# Mapping Milky Way Dust in 3D With Stellar Photometry

# Mapping Milky Way Dust in 3D with Stellar Photometry


A DISSERTATION PRESENTED
BY
GREGORY MAURICE GREEN
TO
THE DEPARTMENT OF ASTRONOMY


IN PARTIAL FULFILLMENT OF THE REQUIREMENTS
FOR THE DEGREE OF
DOCTOR OF PHILOSOPHY
IN THE SUBJECT OF
ASTRONOMY AND ASTROPHYSICS


HARVARD UNIVERSITY
CAMBRIDGE, MASSACHUSETTS
MAY 2016

Thesis advisor: Professor Douglas P. Finkbeiner Gregory Maurice Green

# Mapping Milky Way Dust in 3D with Stellar Photometry

## Abstract

I present a three-dimensional map of interstellar dust reddening, covering three-quarters of the sky out to a distance of several kiloparsecs, based on Pan-STARRS 1 and 2MASS photometry. The map reveals a wealth of detailed structure, from filaments to large cloud complexes. The map has a hybrid angular resolution, with most of the map at an angular resolution of $3.4'$ to $13.7'$, and a maximum distance resolution of $\sim 25\%$. The three-dimensional distribution of dust is determined in a fully probabilistic framework, yielding the uncertainty in the reddening distribution along each line of sight, as well as stellar distances, reddenings and classifications for 800 million stars detected by Pan-STARRS 1. The method developed here compares observed stellar photometry with empirical stellar templates, incorporating prior knowledge about the structure of the Galaxy.

I validate the per-star reddening estimates by comparison with reddening estimates for stars with both SDSS photometry and SEGUE spectral classifications, finding per-star agreement to within $\sim 0.15$ mag out to a stellar $\mathrm{E}(B-V)$ of 1 mag. I demonstrate the consistency of the resulting reddening estimates with those of two-dimensional emission-based maps of dust reddening. In particular, I find agreement with the *Planck* $\tau_{353\,\mathrm{GHz}}$-based reddening map to within 0.05 mag in $\mathrm{E}(B-V)$ to a depth of 0.5 mag, and explore systematics at reddenings less than $\mathrm{E}(B-V) \approx 0.08$ mag. I compare the 3D map developed here to two existing three-dimensional dust maps, by Marshall *et al.* (2006)

and Lallement *et al.* (2014), exploring the strengths and weaknesses of the different 3D mapping methods. The map presented here has better angular resolution than both 3D maps compared, and it has better distance resolution than Marshall *et al.* (2006) within $\sim$3 kpc, but shows radial "finger-of-God" features not contained in Lallement *et al.* (2014).

The map can be queried or downloaded at `http://argonaut.skymaps.info`. I expect the three-dimensional reddening map presented here to find a wide range of uses, among them correcting for reddening and extinction for objects embedded in the plane of the Galaxy, studies of Galactic structure, calibration of future emission-based dust maps and determining distances to objects of known reddening. The method we present is not limited to the passbands of the Pan-STARRS 1 and 2MASS surveys, but may be extended to incorporate photometry from other optical and near-infrared surveys, such as WISE, *Spitzer* GLIMPSE, UKIDSS, SDSS, and in the future, LSST and *Gaia*. The method can also be naturally extended to stellar kinematic data, such as that soon to be released by *Gaia*.

# Contents

# List of figures

To my cousin Alexander Szejman (1927-2014), with whom I had many long discussions on science, history and politics into the early hours of the morning, and who led a truly unusual life.

# Acknowledgments

THANKS MUST GO FIRST OF ALL TO MY PARENTS, Heather and David Green, who raised me in an intellectual household, and who encouraged my interest in science, languages, and many other fields. I would also like to thank my wife, Kitty Yeung, my two brothers, Daniel and Anthony, and the childhood friends who have been like brothers and sisters to me. I am also deeply grateful to my doctoral advisor, Douglas Finkbeiner, for his years of mentorship.

I would also like to acknowledge the colleagues whose work contributed to §§ 1 to 5:

> Edward F. Schlafly, Douglas P. Finkbeiner, Hans-Walter Rix, Nicolas Martin, Mario Jurić, Will Burgett, Kenneth C. Chambers, Peter W. Draper, Heather Flewelling, Nicholas Kaiser, Rolf Peter Kudritzki, Klaus Hodapp, Eugene Magnier, Nigel Metcalfe, Paul Price, John Tonry, Richard Wainscoat and Christopher Waters.

The Pan-STARRS 1 Surveys (PS1) have been made possible through contributions of the Institute for Astronomy, the University of Hawaii, the Pan-STARRS Project Office, the Max-Planck Society and its participating institutes, the Max Planck Institute for Astronomy, Heidelberg and the Max Planck Institute for Extraterrestrial Physics, Garching, Johns Hopkins University, Durham University, the University of Edinburgh, Queen's University Belfast, the Harvard-Smithsonian Cen-

ter for Astrophysics, the Las Cumbres Observatory Global Telescope Network Incorporated, the National Central University of Taiwan, the Space Telescope Science Institute, the National Aeronautics and Space Administration under Grant No. NNX08AR22G issued through the Planetary Science Division of the NASA Science Mission Directorate, the National Science Foundation under Grant No. AST-1238877, the University of Maryland, and Eötvös Loránd University (ELTE). This publication makes use of data products from the Two Micron All Sky Survey (2MASS), which is a joint project of the University of Massachusetts and the Infrared Processing and Analysis Center/California Institute of Technology, funded by the National Aeronautics and Space Administration and the National Science Foundation. The computations in this dissertation were run on the Odyssey cluster supported by the FAS Science Division Research Computing Group at Harvard University. Gregory Green and Douglas Finkbeiner are supported by NSF grant AST-1312891.

# 0

# Introduction

OOKING UP ON A DARK NIGHT, one can make out a faint, nebulous glow that arcs across the sky. If the night is especially clear and dark, one can perceive dark lanes reaching through this band of light. Today, we know that this nebulosity is actually a mass of billions of stars, too faint and close together for our eyes to discern them as individual points of light. Because most of the stars of our Galaxy, the Milky Way, are located in a flattened

disc, in which our Solar system is embedded, these stars appear to trace out an arc across the sky. The dark lanes and spots that appear superimposed on this arc are regions where intervening clouds of small particles absorb or scatter away a substantial portion of the background starlight. These particles are known in astrophysics as "dust."

Because interstellar dust attenuates the light of background objects, knowing how much dust is along the line of sight is of critical importance when determining the true brightness of an object. Further complicating matters, interstellar dust does not absorb equally across the entire electromagnetic spectrum. Dust extinction peaks in the ultraviolet (UV), and declines as wavelength increases through the visible and infrared (IR) regions of the spectrum. Thus, not only is the apparent brightness of an object affected by dust, but also the shape of the spectrum. A precise knowledge of both the total column density of dust and the shape of the wavelength–extinction curve is therefore needed to accurately correct observations in the ultraviolet, visible, and infrared.

Up until recently, most work on mapping interstellar dust extinction has focused on the two-dimensional distribution of dust across the sky. The distribution of dust along the third dimension, distance, is much more difficult to obtain. This thesis presents work that I have carried out on mapping the extinction caused by interstellar dust in the Milky Way in three dimensions. The second critical aspect required for precision astronomy – the problem of mapping variation in the wavelength–extinction curve of dust across the Milky Way – is left for future investigation.

The thesis is organized as follows. § 0 discusses the history of the investigation of interstellar dust, gives a brief overview of relevant dust properties, and introduces several methods which have been used to map dust reddening and extinction in two dimensions across the sky. § 1 presents a proba-

bilistic framework for inferring the three-dimensional structure of dust reddening. In § 2, the empirical models necessary to apply this framework to the Pan-STARRS 1 and 2MASS photometric surveys are developed. In § 3, I validate the methods developed in § 1, using both simulated catalogs and comparisons with real data. § 4 presents the resulting three-dimensional map of dust reddening, and compares it with previous two- and three-dimensional maps. Finally, § 5 points to some directions forward in the field of dust mapping.

## 0.1 The Discovery of Dust

The pre-Socratic Greek philosopher Democritus, an atomist who lived from the late 5$^{th}$ to the early 4$^{th}$ century B.C., held that the light of the Milky Way comes from a large number of stars. In a short overview of the views of various philosophers on the subject, Pseudo Plutarch* writes that Democritus believed the Milky Way to be "the splendor which ariseth from the coalition of many small bodies, which, being firmly united amongst themselves, do mutually enlighten one another" (Ps. Plut. Plac. 3.1; *trans.* W. Goodwin, 1874). In the modern age, it was Galileo who first confirmed this hypothesis, soon after first directing his telescope at the sky. Through the telescope, the faint glow of the Milky Way resolves into individual points of light. In a wonderful passage of *Sidereus Nuncius* (*The Starry Messenger*) that emphasizes the importance of empiricism in science, Galileo relates,

> In third place, I have observed the essence or substance of the MILKY WAY circle. By the aid of a telescope anyone may behold this in a manner which so distinctly appeals

*Placita Philosophorum* was long falsely attributed to the great Greek historian Plutarch. *Pseudo Plutarch* therefore refers to the unknown author of *Placita*. As no works of Democritus have survived to the present day, we rely on second-hand reports, including the works of so-called *doxographers*, such as Pseudo Plutarch, to relate Democritus' views.

> to the senses that all the disputes which have tormented philosophers through so many ages are exploded at once by the unquestionable evidence of our eyes, and we are freed from wordy disputes upon this subject, for the GALAXY is nothing else but a mass of innumerable stars planted together in clusters. Upon whatever part of it you direct the telescope straightway a vast crowd of stars presents itself to view; many of them are tolerably large and extremely bright, but the number of small ones is quite beyond determination. (Galileo, 1610; *trans.* P. Baker, 2004)

In the late 18$^{th}$ century, William Herschel undertook a careful count of the number of visible stars, in an attempt at determining "the construction of the Heavens" (Herschel 1785). Scanning along lines of constant Galactic longitude, Herschel counts the number of stars visible in his telescope at different Galactic latitudes. He notices that while the number of stars increases as one approaches the Milky Way, there are areas where the star count drops suddenly to zero. Herschel terms such apparently starless regions of the Milky Way "opening[s] in the Heavens." Because he notices dense clusters of stars in the vicinity of some of these "openings," he speculates that they are indeed devoid of stars, with all the stars having fallen into the nearby clusters.

The nature of these seemingly empty regions of the Milky Way – whether they indeed lack stars or whether some obscuring matter blocks our view of them – remained open until the early 20$^{th}$ century, when astronomers converged on the problem from a number of different angles. Two astronomers in particular, E.E. Barnard and Max Wolf, approached the problem directly by imaging dark regions on the sky. Barnard (1916) advances a number of arguments as to why so-called "dark markings on the sky" are caused by obscuring masses, rather than stellar voids. Perhaps the most convincing arguments he makes involve comparisons with bright nebulae – that is, nebulae that are bright in visible light (due to reflection of the light of nearby stars, although this mechanism was

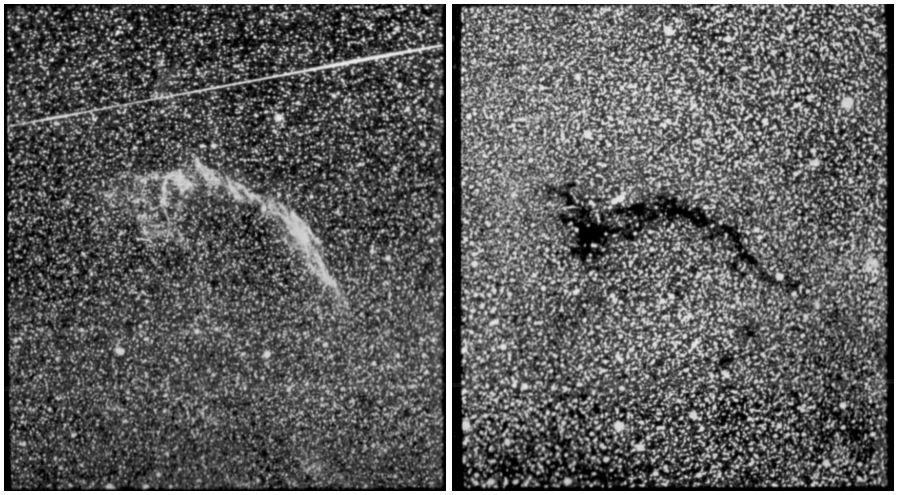

(a) Gaseous Nebula NGC 6995. (b) Dark Object in Cepheus.

Figure 0.1: Adapted from Plate I of Barnard (1916), comparing a reflection nebula (left) with a dark nebula (right). Note the similarity in the shape of the two nebulae. Barnard (1916) argues on the basis of such similarities that "bright" and "dark" nebulae may be of similar nature, and that dark nebulae are therefore not regions of space devoid of stars. © AAS. Reproduced with permission.

not known at the time). Barnard notes the similarity in shape and size between many bright nebulae and "dark markings," suggesting that they may be a related class of objects. A particularly striking example is shown in Fig. 0.1. Barnard also notes that in some regions of the sky, nebula-shaped "dark markings" are superimposed on bright nebulae, again suggesting that these dark regions are indeed nebulae, rather than simply being starless regions of the Galaxy.

Wolf (1923) pursues this comparison further, pointing to regions of the sky where bright and dark nebulae seem to be intertwined in complex forms, and arguing that the two types of nebulae must somehow be connected. Wolf attempts here as well perhaps the first distance determination to a dark nebula, by comparing distribution of stellar apparent magnitudes in the direction of the nebula and in an unobscured field offset from the nebula.

In order to understand Wolf's method, it is first necessary to introduce the concept of "distance modulus," a logarithmic unit of distance which will be used frequently throughout this thesis. When dealing with magnitudes, distance modulus, denoted by $\mu$, is often more useful than "raw" distance. It is related to distance $r$ by:

$$\frac{\mu}{1\,\mathrm{mag}} = 5 \log_{10}\left(\frac{r}{10\,\mathrm{pc}}\right) . \tag{0.1}$$

Note that $\mu$ has units of magnitudes. The primary use of this unit is that increasing the distance modulus of a source by a given number of magnitudes increases the apparent magnitude by an equal amount.

Wolf's method for determining distances to dark nebulae works as follows. Imagine that all stars were to have the same absolute magnitude, $M_\star$. Because stars lie at different distances, we observe them at a range of apparent magnitudes. Denote the number of stars brighter than apparent magnitude $m$ as $N_\star(< m)$. We observe two fields that are identical, except for the fact that the first is completely unobscured, while the second field has a dark nebula at fixed distance, which extinguishes background stars. Let us assume the cloud in the obscured field is at distance modulus $\mu_{\mathrm{cloud}}$, and extinguishes background stars by $A$ magnitudes. In the obscured sightline, stars with apparent magnitudes $m < M_\star + \mu_{\mathrm{cloud}}$ are in front of the dust cloud. $N_\star(< m)$ is therefore exactly the same in the unobscured and obscured sightlines out to this apparent magnitude. Beyond this apparent magnitude, however, stars in the obscured sightline are an additional $A$ magnitudes fainter. In the obscured sightline, there is therefore a break in the curve $N_\star(< m)$, which allows one to determine

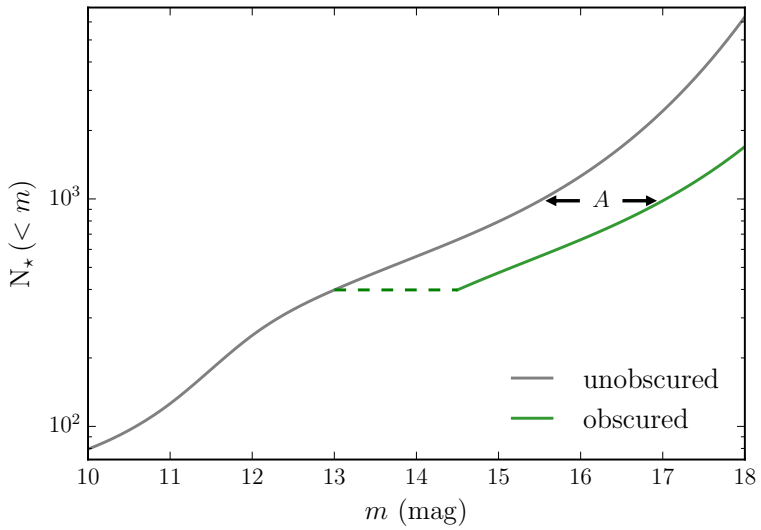


Figure 0.2: A prototypical Wolf diagram, an early method of determining distances to dust clouds, introduced by Wolf (1923). The number of stars brighter than a given apparent magnitude is plotted for two sightlines. The gray line corresponds to an unobscured sightline with no dust cloud, while the green line corresponds to a sightline with a single dust cloud. The two sightlines are identical, except that in the obscured sightline, all the stars that are behind the cloud are $A$ magnitudes fainter.

the distance modulus and extinction of the dust cloud. An illustration of Wolf's method is given in Fig. 0.2.

In reality, things are not so simple as in this toy example. Stars come in a wide range of different absolute magnitudes, and the dust along a given line of sight does not necessarily all reside at one distance. After Wolf's initial paper on the subject, others began using "Wolf diagrams" to study cloud distances, with varying levels of sophistication, and often questionable results (Bok 1960). A correct implementation of Wolf's idea requires a good knowledge of the luminosity function of stars, and their spatial distribution throughout the Milky Way, and requires a level of statistical modeling not common in astronomy at the time.

Wolf (1923) finally studies the colors of stars in the region of a dark nebula, and away from the

nebula. Wolf notes that neutral gas would redden stellar spectra through Rayleigh scattering, but erroneously assumes that dust would have such an effect. In an example of two wrongs making a right, Wolf measures no difference in colors of stars in the direction of the nebula and away from the nebula, and concludes that dark nebulae contain dust.

A separate line of reasoning that led astronomers to consider the existence of interstellar extinction of light had to do with the number of observed stars in different regions of the sky. In 1847, F.G.W. von Struve considered the observed distribution of stars across the sky, as a function of apparent magnitude, finding it to be inconsistent with the hypothesis that the density of stars is the same everywhere in space (Struve 1847). In fact, von Struve found that star counts rose less quickly with magnitude than expected in all directions, implying that the density of stars falls off *in all directions* from the Sun. One has to either accept that the Sun is in the center of the Galaxy, or that observed stellar flux drops off faster than with the square of the distance. Let us again assume that all stars have the same absolute magnitude, $\mathcal{M}_\star$. At a given distance modulus, $\mu$, stars will have apparent magnitude $m = \mathcal{M}_\star + \mu$. As before, denote the number of stars fainter than magnitude $m$ as $N_\star(< m)$. The number of stars per unit distance is given by

$$\frac{\mathrm{d}N}{\mathrm{d}r} = 4\pi n_\circ r^2 \,, \tag{0.2}$$

where $n_\circ$ is the number density of stars (which we are assuming to be uniform throughout the uni-

verse). Using the fact that $\mathrm{d}r = \frac{\ln 10}{5} r \, \mathrm{d}\mu$ (which can be easily derived from Eq. (0.1)), we find that

$$\frac{\mathrm{d}N}{\mathrm{d}\mu} = \frac{4\pi \ln 10}{5} n_0 r^3 \propto 10^{3\mu/5} . \tag{0.3}$$

Since apparent magnitude increases linearly with apparent magnitude, the above implies that

$$\frac{\mathrm{d}N}{\mathrm{d}m} \propto 10^{3m/5} . \tag{0.4}$$

In a universe filled uniformly with stars of the same absolute magnitude, the number of observed stars increases exponentially with apparent magnitude. If we now allow stars to have a range of absolute magnitudes, we can see that we arrive at the same result. Each class of stars contributes a term of the form Eq. (0.4) to the observed distribution of apparent magnitudes, with the result that $\frac{\mathrm{d}N}{\mathrm{d}m}$ is proportional to $10^{3m/5}$, regardless of the distribution of absolute magnitudes. All that we have assumed here is that stellar density is uniform, and that there is no obscuring matter.

Because the observed abundance of stars does not rise as quickly with apparent magnitude as Eq. (0.4) dictates, Struve (1847) considers the possibility of an absorbing medium. Von Struve is also motivated to assume the existence of interstellar extinction by Olbers' paradox, which states that in an infinite universe of infinite age, filled uniformly with stars, the sky will be as bright as the surface of a star. Jacobus Kapteyn, at Groningen University, elaborates a similar argument to von Struve, rejecting the idea that the Sun is in a special position in the Galaxy (i.e., at the center) (Kapteyn 1904). Kapteyn finds that if interstellar extinction increases by $\sim$1.6 magnitudes per kiloparsec, the data

available at the time implies a uniform stellar density throughout space. A smaller rate of increase of extinction implies that stellar number density falls in all directions from the Sun, while a greater extinction implies that the stellar number density rises in all directions.

Kapteyn then set about looking for selective extinction – that is, extinction that depends on wavelength. If either gas or particulate matter causes extinction, one expects greater extinction at short wavelengths than at long wavelengths. This means that stars that suffer greater extinction will also appear redder, since less of their blue light reaches us. Kapteyn (1909a) and Kapteyn (1909b) consider the measured *photographic* and *visual* magnitudes[†] (corresponding roughly to blue and green, respectively) of stars with distance estimates and well-determined spectral classifications. Modeling the dependence of observed *photographic - visual* magnitudes on apparent magnitude, absolute magnitude and distance, Kapteyn finds that selective absorption increases by $\sim 0.66\ ^{\mathrm{mag}}/_{\mathrm{kpc}}$ in these passbands.

Kapteyn had found in 1890 that there were systematic differences in the distribution over the sky of stars observed by surveys at different wavelengths. In particular, the ratio of the number of stars observed in the Galactic plane to the number observed at the Galactic poles varied between surveys (de Sitter 1900). Motivated by this finding, Kapteyn's student, Willem de Sitter, undertook a number of efforts to systematically compare the *photographic - visual* colors of stars in the Galac-

[†]The terms "*photographic*" and "*visual*" derive originally from the fact that there were two methods, in the late 19$^{\mathrm{th}}$ century, of determining the apparent brightness of stars. To the age-old method of assigning magnitudes based on the visual appearance of stars had been added the new method of assigning magnitudes based on the appearance of stars on photographic plates. As photographic plates at the time were more sensitive to blue light than the human eye, *photographic* magnitudes could differ from *visual* magnitudes, depending on the color of the object being observed. Thus, *photographic* magnitudes are more a measure of the apparent brightness of a star in blue light, while *visual* magnitudes are more a measure of apparent brightness in green light.

tic plane with those of stars at the Galactic poles (de Sitter 1900, 1904). As this was long before the era of CCDs and electronic computers, accurate calibration of stellar magnitudes was a much more painstaking and fraught task than it is today. Magnitudes at the time were determined from the isophotal size of sources on photographic plates, and there was a worry that in crowded stellar fields in the Milky Way, isophotal size might vary differently with magnitude than in sparse fields. De Sitter (1904) tested for this effect by taking two exposures on the same plate – one off the plane of the Galaxy one in the plane. By switching the order in which these two exposures were taken (whether the Galactic plane was imaged first or second), de Sitter could test the effect of crowding on the magnitudes of stars at the Galactic poles. After convincing himself that his photometry war sufficiently accurate, de Sitter concluded that the colors of stars at the Galactic poles are largely homogeneous, while the colors of stars in the Galactic plane are redder, with large differences in the colors of stars in different regions of the Galactic plane. De Sitter raised the possibility that this is due to the presence of a selectively absorbing medium, and references photographs of "extended faint nebulosities" taken by Max Wolf and E.E. Barnard.

However, the existence of interstellar extinction was not completely uncontroversial. As late as 1916, Harlow Shapley argued that selective absorption was negligible (Shapley 1916). Noting that Kapteyn and others had measured selective absorption with nearby stars, Shapley pointed out that if the effect increases linearly with distance, a greater baseline would give a more accurate measurement. Shapley took photometric and spectroscopic measurements in the globular cluster Messier 13, known then to be at a distance of more than a kiloparsec. To his surprise, Shapley found that the colors of stars in M13 are similar to those of nearby stars. Given the great distance of the globular

cluster, a uniform selective absorption of the magnitude claimed by Kapteyn (1909b) would be easily observable. Shapley therefore concluded that selective absorption in interstellar space is negligible, and that by extension, non-selective absorption is also most likely negligible. Interestingly, Shapley's findings convinced Kapteyn of the absence of interstellar absorption, which led him to conclude further that the Sun must reside near the center of the Milky Way (Gingerich 2000). The source of the discrepancy between Shapley and Kapteyn's results on selective absorption, of course, lies in the fact that dust is not evenly distributed throughout the Galaxy. Interstellar dust is concentrated in a thin (and extremely inhomogeneous) layer in the midplane of the Milky Way. M13 lies significantly out of the plane of the Galaxy, and therefore suffers little extinction from our point of view. As Gilmore (2000) points out, it is difficult, from a modern perspective, to undestand how early-20$^{th}$ century astronomers, looking up at the rifts of the Milky Way (visible even to the naked eye) did not ascertain that interstellar absorption is the norm, or indeed highly variable throughout space.

The photographs which Max Wolf and E.E. Barnard published of "dark markings" on the sky did much to persuade astronomers that such markings were indeed obscuring clouds. In 1922, Henry Norris Russell, Harlow Shapley's doctoral advisor, wrote that Bernard's photographs had been particularly persuasive (Russell 1922). Russell was also of the opinion that such obscuring clouds in the plane of the Milky Way were the cause of the "region of avoidance," the equatorial band of the Galaxy where Globular Clusters were not observed (Seeley & Berendzen 1972a). Russell speculated that the cause of obscuration in such clouds is fine dust. As larger grains are more efficient at absorbing and scattering than very small grains or gas molecules, if they make up even a small portion of total mass of such clouds, they should dominate the extinction (Russell 1922). Russell additionally

discussed how light with wavelength much larger than the grain size is selectively extinguished (Russell assumed that Rayleigh scattering is the primary means of extinction), and concluded that grains several microns in diameter will dominate interstellar extinction (Russell 1922).

A simple mathematical explanation of the dependence of extinction on grain size goes as follows. Imagine that a cloud with total mass $M$ is composed of spherical particles of radius $a$. The mass of each particle goes as $m \propto a^3$, while the geometric cross-section of each particle goes as $\sigma_{\rm geom} \propto a^2$. However, the efficiency with which a particle extinguishes light of wavelength $\lambda$ depends on the ratio $a/\lambda$. The effective cross-section is then given by

$$\sigma = \sigma_{\rm geom}\, q\left(\frac{a}{\lambda}\right) \propto a^2 q\left(\frac{a}{\lambda}\right) \ , \tag{0.5}$$

where the efficiency $q(a/\lambda)$ depends on the detailed scattering and absorption properties of the particles. The total number of particles in the cloud is given by $N = M/m$, and the total cross section of all the particles is given by $N\sigma$. Thus,

$$N\sigma = \frac{M\sigma}{m} \propto \frac{1}{a}\, q\left(\frac{a}{\lambda}\right) \ . \tag{0.6}$$

We can therefore see that the effect of grain size on the extinction of the cloud depends on how efficiency $q$ scales with $a/\lambda$. When the grains are large compared to the wavelength of the impinging light (i.e., $a/\lambda \gg 1$), we are in the geometric optics limit, where diffraction of light around the particle is negligible, and $q \approx 1$. Extinction therefore scales with $1/a$. In the limit of large grains, increas-

ing grain size decreases the total extinction of the cloud. In the opposite limit, where the grains are much smaller than the wavelength (i.e., $a/\lambda \ll 1$), scattering and absorption efficiency fall off more quickly than $a/\lambda$, so total extinction scales with a positive power of $a$. In the limit of small grains, therefore, decreasing grain size reduces the total extinction of the cloud. Thus, the maximum extinction is produced when the cloud is made up of particles for which $a \sim \lambda$. As extinction is greatest in the ultraviolet and optical regions of the spectrum, we can deduce that the grains causing the extinction are hundreds of nanometers to microns in scale.

In his 1909 paper, "On the Absorption of Light in Space," Jacobus Kapteyn discusses an additional effect that interstellar matter might have: discrete spectral lines, which he terms "space lines." He remarks, however, that "[as] I have no evidence as to the real occurrence of such lines or bands, no more need be said about them at present." (Kapteyn 1909a) In the same year, the Lowell Observatory astronomer Vesto Slipher reported the discovery of Calcium absorption lines in stellar spectra (Slipher 1909). If these lines were to arise from Calcium in the stellar atmsopheres, one would expect them to be red- or blueshifted in accordance with the proper motion of the stars. Slipher finds, however, that these Calcium absorption lines do not shift in wavelength according to stellar proper motions, and that, moreover, stars near to one another on the sky often share similar Calcium absorption features. Slipher references Kapteyn's prediction, concluding that the observed Calcium absorption lines arise from interstellar clouds (Slipher 1909; Seeley & Berendzen 1972a).

Thus, in the early 1900s, astronomers pursuing different avenues of research suggested that there is extinction in interstellar space, that this extinction might be selective (i.e., that it might depend on wavelength), that it might be associated with interstellar emission lines, and that it might be related

to the problem of Herschel's "opening[s] in the Heavens."

In 1930, Robert J. Trumpler published a number of groundbreaking papers which firmly established the existence of interstellar dust, established that it causes both general and selective extinction, gave an estimate of the grain size, traced how extinction varied with wavelength, and showed that dust is concentrated in the plane of the Galaxy. Trumpler's investigation of dust grew out of his work on open clusters, groups of young stars that formed out of a single primordial cloud of gas and dust. Trumpler measured the distance to open clusters using two different methods (Trumpler 1930b):

1. Comparison of the apparent diameters of open clusters with the expected physical diameter of clusters having similar characteristics, and
2. Comparison of the apparent magnitudes of cluster stars with those of nearby stars having the same spectral type.

For the first method, Trumpler divided open clusters into twelve categories, based on the level of concentration of stars in the center of the cluster and the total richness (or number of stars) of the cluster. Within each class of open clusters, Trumpler was able to derive a relation between the apparent diameter of the cluster and its distance (Trumpler 1930b; Seeley & Berendzen 1972b). This distance measure rests on the assumption that within each class of clusters, the physical diameter of the cluster is predictable, so that distance can be inferred from apparent diameter. For the second method, Trumpler derived absolute magnitudes for cluster stars by matching them with nearby stars of the same spectral classification. If the absolute magnitude, $M$, of a star is known, then the

distance modulus, $\mu$, can be determined according to the equation

$$m = M + \mu \,, \tag{0.7}$$

where $m$ is the apparent magnitude. This equation assumes that there is no obscuration of the star's light. Trumpler found that the magnitude-based measure systematically gives a larger distance estimate than the diameter-based measure (Trumpler 1930b,a). Additionally, Trumpler found that the colors of cluster stars are systematically redder than their nearby counterparts of the same spectral type. The presence of dust would both reconcile the two types of distance measurements and explain the reddishness of stars in open clusters. The presence of extinction modifies Eq. (0.7) to read

$$m = M + \mu + A \,, \tag{0.8}$$

where $A$ is extinction, in magnitudes. Holding $m$ and $M$ constant, larger extinction $A$ implies smaller distance modulus $\mu$. Assume that $A$ varies with distance, and rearrange the above, to obtain:

$$\mu + A(\mu) = m - M \,. \tag{0.9}$$

Varying how extinction depends on distance will alter the solution for $\mu$, and thus distance. Trumpler found that 0.7 $^{\text{mag}}/_{\text{kpc}}$ would remove the discrepancy between his two types of distance measures (Trumpler 1930b,a). Trumpler's results are visualized in Fig. 0.3. Consistency with Shapley's

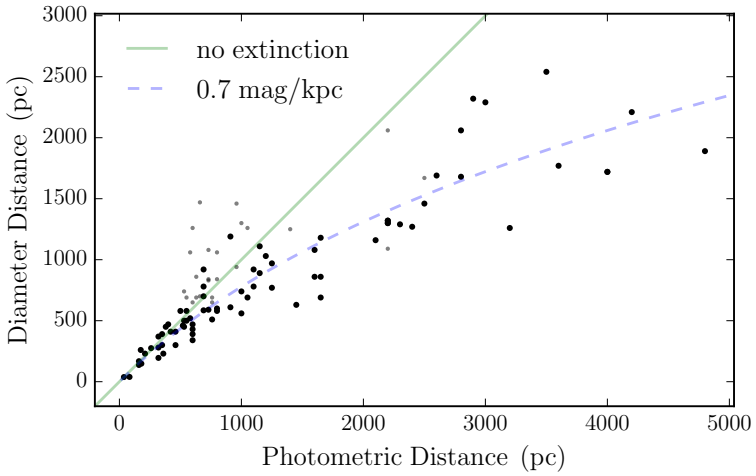


Figure 0.3: Open cluster distances derived from photometry and from diameters, adapted from Trumpler (1930a), using distances from Table 3 of Trumpler (1930b). Open clusters with less certain photometric distance estimates are denoted by lighter dots. The solid line shows the one-to-one relationship one would expect in the absence of extinction, while the dotted line shows the relation one would expect if there were unaccounted-for extinction. Even if the diameter distances are off by a linear scale factor, the non-linear relationship between the two distance measures indicates the presence of extinction.

finding of little selective extinction for globular clusters at high Galactic latitudes required that the dust be concentrated in the plane of the Milky Way (Trumpler 1930b,a). Trumpler's work therefore reconciled Kapteyn's finding of significant general and selective absorption with Shapley's finding that distant globular clusters, significantly above the plane of the Galaxy, have little reddening.

Trumpler (1930a) contains a thorough discussion of the possible effects that an interposing medium could have on our observations of astronomical sources, which is still well worth reading in this day. The five effects he lists are

1. General absorption: extinction that does not depend on wavelength, which we would now term the "gray component" of extinction.
2. Selective absorption: which we would also term "reddening" today.
3. Monochromatic absorption: extinction at discrete wavelengths, due to specific absorption

lines in the interstellar medium.

4. Obscuration effects: complete absorption or scattering of the light of background objects, which might be subsumed into the first category.

5. Dispersion of light: variation in the wave speed of light in the interstellar medium, which would cause light of different wavelengths from transient events to reach us at different times.

Tentatively assuming extinction to come from Rayleigh scattering by small particles, Trumpler calculates the density of obscuring matter that would be required to produce the observed extinction of 0.7 $^{\text{mag}}/_{\text{kpc}}$. Rayleigh scattering occurs in the limit that the scattering particles are much smaller than the wavelength of the impinging light. In the language of Eq. (0.5), $q(a/\lambda) \propto (a/\lambda)^4$. Scattering efficiency thus drops dramatically as one decreases the size of the scattering particles. Motivated by the existence of calcium lines in the interstellar medium (as discovered by Vesto Slipher), Trumpler (1930a) calculates the mass density that would be required if the scatterers were individual calcium atoms. Because of the very small size of an individual calcium atom, its scattering efficiency for optical light is extremely small, and an enormous density of atoms – equivalent to 1700 Solar masses per cubic parsec – would be required to produce the observed growth of extinction with distance. By comparison, the total mass of *stars* in the solar neighborhood is on the order of one Solar mass per cubic parsec. In order to reduce the necessary mass density of scatters to a reasonable level, which Trumpler sets at half a Solar mass per cubic parsec, Trumpler calculates that each grain should contain 3400 calcium atoms.[‡] Thus, Trumpler (1930a) for the first time firmly established that the matter responsible for interstellar extinction is dust-like in nature. Trumpler notes that this dust

[‡]As we now now, calcium is not the primary constituent of the interstellar medium. See § 0.2 for an overview of the graphite/silicate model of dust. Trumpler's reasoning, however, still stands, as it does not depend on the atoms involved in the scattering being calcium.

may be distributed highly unevenly throughout the Milky Way, and that the "dark nebulae" may be particularly dense condensations.

In a third paper from 1930, Trumpler investigates the wavelength–dependence of extinction, by use of what we would now term the "pair method": by comparing the spectrum of a distant star with a nearby, and therefore presumably unreddened star, one can trace how extinction changes with wavelength (Trumpler 1930c). Trumpler finds that the wavelength–dependence of interstellar extinction does not follow Rayleigh's law, and proposes that there may be a range of grain sizes in the interstellar medium. From a modern perspective, we now know that this is half of the explanation, but that absorption due to dust does not fall off as $\lambda^{-4}$ at large wavelengths (see, e.g., Fig. 0.4).

Thus, by the end of 1930, one can say that the existence of dust in the interstellar medium was firmly established. Since then, the study of interstellar dust has branched out in many directions, including the effort to map its distribution throughout space in detail – an effort which this thesis extends.

## 0.2 An Overview of Dust Properties

In the present era, while there has been much progress in the study of dust properties, our knowledge of the composition of dust is still highly uncertain. It is beyond the scope of this introduction to catalog the different models of dust composition. In what follows, I briefly review the present state of knowledge about the basic properties of interstellar dust, focusing on the graphite/silicate model, although it is by no means the only existing model.

The interstellar medium is 1% dust by mass, yet dust plays an outsize role in the physics of the

ISM. Dust absorbs and scatters light in the UV, optical and NIR regions of the spectrum, re-radiating away the energy it gains in the MIR and FIR. By one estimate, dust reprocesses an estimated 30% of all stellar light in the Universe in this manner (Draine 2003). In optical UV, optical and NIR astronomy, one must often make corrections for the effect of dust extinction on one's observations. In FIR astronomy – particularly in studies of the cosmic microwave background – dust emission is often a foreground contaminant. Thus, in many areas of astronomy, a good understanding of the dust properties is important for precision measurements.

Given this fact, it is perhaps surprising that our current knowledge of the basic composition of dust is highly uncertain. Models of dust composition must be designed to produce the observed extinction and emission spectrum of interstellar dust, and are constrained in the range of dust compositions they can propose by the known abundance of different elements. Additional information about grain properties come from measurements of the polarization of extinction. In what follows, I will give a brief overview of dust extinction features, leaning heavily on one particular model of dust composition, the graphite/silicate model of Weingartner & Draine (2001).

The modeled dust extinction spectrum of Weingartner & Draine (2001) is plotted in Fig. 0.4. The particular extinction spectrum plotted in Fig. 0.4 is for "average" Milky Way dust, while Weingartner & Draine (2001) also allows for variation in the dust properties. This is because the composition and radiative environment of dust varies throughout the Milky Way, and, of course, from galaxy to galaxy, leading to different extinction and emission spectra. However, some general features of the dust extinction spectrum are:

- Extinction peaks in the UV, and then declines with increasing wavelength through the optical

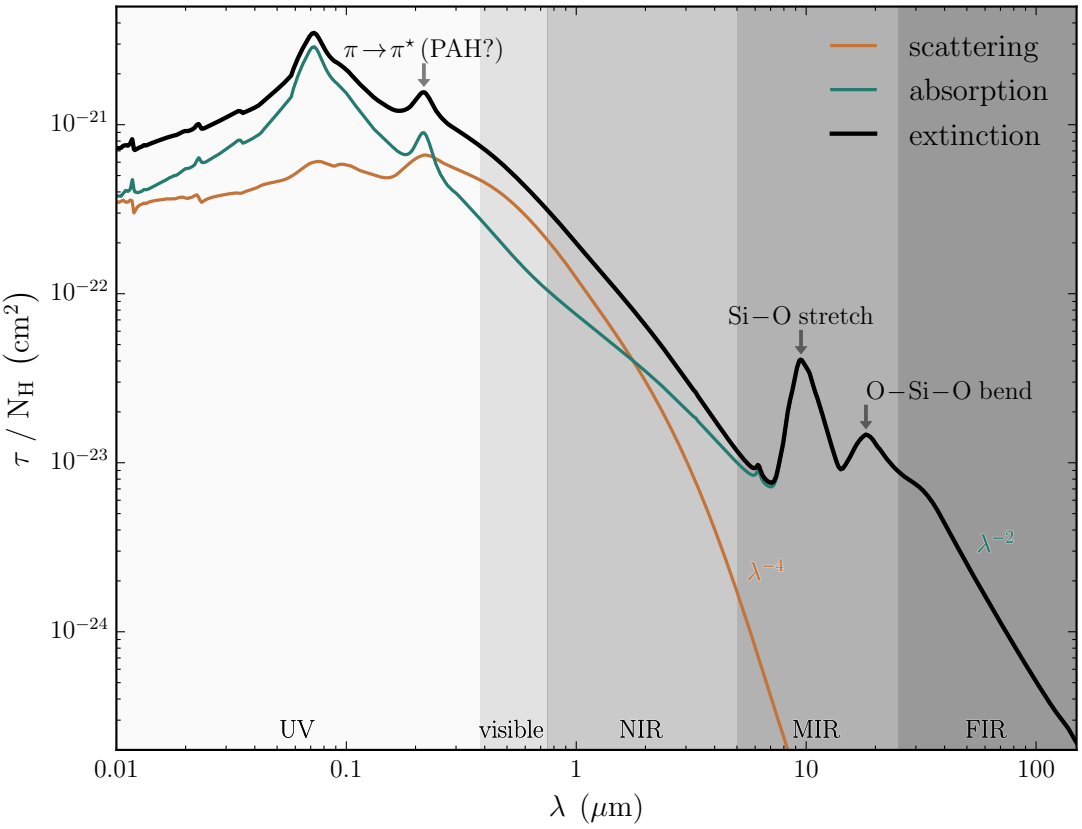


Figure 0.4: The dust extinction spectrum for "average" Milky Way dust, according to the graphite/silicate model of Weingartner & Draine (2001). Extinction is given in units of optical depth per hydrogen nucleon, as a function of wavelength. The different regions of the spectrum are marked for ease of interpretation. Both scattering and absorption of light by dust grains cause extinction. Of particular note are the 2175 Å (0.2175 $\mu$m) feature, likely caused by electronic $\pi \rightarrow \pi^*$ transitions in PAH molecules; and the broad absorption features in the MIR, likely caused by Si–O stretching and O–Si–O bending modes in amorphous silicates. At long wavelengths, scattering obeys the Rayleigh's law, with a $\lambda^{-4}$ dependence, while absorption drops off with $\lambda^{-2}$.

and IR.

- A "bump" in extinction at 2175 Å.
- Broad extinction features at $\lambda \approx 10$ $\mu$m and 18 $\mu$m.

Polycyclic aromatic hydrocarbon (PAH) molecules or small graphite spheres are the most likely cause of the peak in extinction at 2175 Å (Draine 2003). Both PAHs and graphite contain aromatic rings – particularly stable hexagonal rings of carbon – with a delocalized electron in a $\pi$ bonding orbital. This electron has an excited anti-bonding state, $\pi^*$, with a gap approximately equivalent to the energy of a photon with wavelength 2175 Å. Graphite and PAH molecules therefore generally have a $\pi \rightarrow \pi^*$ absorption feature in the 2175 Å region. The abundance of carbon in the interstellar medium and the oscillator strength of this transition are sufficient to account for the observed 2175 Å feature. This, together with the presence of what are likely PAH emission features in the MIR, make PAHs and graphite an attractive explanation for the extinction peak at $\lambda \approx 2175$ Å (Draine 2003). In the Weingartner & Draine (2001) graphite–silicate model, PAH molecules smaller than 0.01 $\mu$m lock up about 15% of the carbon in the interstellar medium (Draine 2003).

Broad extinction features in the MIR indicate the presence of silicates in the interstellar medium. Si–O bonds in silicates have a stretching mode with energy spacing corresponding to $\lambda = 9.7$ $\mu$m. Because of the lack of detailed features in this absorption peak, most interstellar silicates are thought to be amorphous, rather than crystalline (Draine 2003). A broad absorption feature at 18 $\mu$m is likely due to an O–Si–O bending mode in silicates. These two silicate absorption features are labeled in Fig. 0.4.

The overall shape of the absorption and scattering spectrum over a wide range of wavelengths

is produced largely by the distribution of grain sizes and the dielectric function of the grain material. In the Weingartner & Draine (2001) model, the distribution of carbonaceous grain size, $a$, has peaks at radii $a \approx 0.0005\ \mu$m, $0.005\ \mu$m and $0.3\ \mu$m, while the silicate size distribution peaks at $a \approx 0.2\ \mu$m (Draine 2003). At wavelengths longer than the largest grain sizes, extinction drops off rapidly, due to suppression by the factor $q(a/\lambda)$ in Eq. (0.5). At short wavelengths, below $a \sim 0.07\ \mu$m, absorption is suppressed due to the high-frequency cut-off in the dielectric response function of the grains. Incident electric fields induce a polarization field within the grain materials by adjustment of the electron orbitals. This polarization cannot be driven at frequencies significantly higher than the classical electron orbital frequency, which for a bonding energy on the order of 13.6 eV is approximately $3 \times 10^{15}$ Hz. This corresponds to a photon wavelength of $\sim$90 nm, not far from the true dust absorption peak. Far above this frequency, the polarization field is increasingly unable to react to the incident electric field, and the grain material becomes transparent.

In this thesis, we deal with photometric data from stars, taken in broad passbands. For this reason, we are not sensitive to the precise behavior of extinction with wavelength, but rather to its effect on the apparent magnitudes of stars in each passband. The extinction in a passband is dependent on the dust transmission curve (which is unitless), $T(\nu)$, the stellar spectral flux density (which has units of energy flux per unit frequency), $f_\nu(\nu)$, and the filter response curve (which is unitless),

$W(\nu)$. The definition of the AB magnitude[§] is

$$m_{\mathrm{AB}} = -2.5 \log_{10} \left[ \frac{\int f_\nu(\nu)\, W(\nu)\, \mathrm{d}\nu}{\int f_\nu^\circ\, W(\nu)\, \mathrm{d}\nu} \right] , \tag{0.10}$$

where $f_\nu^\circ = 3631\,\mathrm{Jy}$ is a constant. Extinction $A$ is the increase in magnitude if we apply the dust transmission $T(\nu)$ to the flux density $f_\nu(\nu)$:

$$A = -2.5 \left[ \log_{10} \int f_\nu(\nu)\, T(\nu)\, W(\nu)\, \mathrm{d}\nu - \log_{10} \int f_\nu(\nu)\, W(\nu)\, \mathrm{d}\nu \right] . \tag{0.11}$$

If the dust transmission $T(\nu)$ is independent of frequency across the passband, then $A$ is independent of $f_\nu$ and $W$:

$$\begin{aligned} A &= -2.5 \left[ \log_{10} \int f_\nu(\nu)\, T_\circ W(\nu)\, \mathrm{d}\nu - \log_{10} \int f_\nu(\nu)\, W(\nu)\, \mathrm{d}\nu \right] \\ &= -2.5 \log_{10} T_\circ . \end{aligned} \tag{0.12}$$

Alternatively, if the filter response function $W(\nu)$ is a Dirac delta centered on $\nu_\circ$,

$$\begin{aligned} A &= -2.5 \left[ \log_{10} \int f_\nu(\nu)\, T(\nu)\, \delta(\nu - \nu_\circ)\, \mathrm{d}\nu - \log_{10} \int f_\nu(\nu)\, \delta(\nu - \nu_\circ)\, \mathrm{d}\nu \right] \\ &= -2.5 \log_{10} T(\nu_\circ) , \end{aligned} \tag{0.13}$$

[§]There are two common definitions of magnitudes in astronomy: the older "Vega magnitude" and the newer "AB magnitude." While the former uses the flux density of Vega as its zeroeth-magnitude reference, the latter uses an idealized reference of constant flux density. For Vega magnitudes, the term $f_\nu^\circ$ should be replaced with $f_\nu^{\mathrm{Vega}}(\nu)$.

and extinction is again independent of the stellar spectrum. Because to some level, $T(\nu)$ is always dependent on frequency, and because the filter response function is never infinitely narrow, the same dust screen does not produce precisely the same extinction for two stars with different spectra. This is typically a small effect, which we will ignore in the remainder of this thesis. For our purposes, dust extinction is described by a vector, $\vec{A}$, the extinction in each band, which increases in magnitude equally for all stars with increasing column density of dust, and whose direction and magnitude can change if the dust properties are altered.

In this work, we rely on empirical prescriptions for dust extinction, rather than the models calculated from first principles, such as that of Weingartner & Draine (2001). Cardelli *et al.* (1989) found that the variation in observed dust wavelength–extinction relation can be approximately described by a one-parameter family of curves. Given a single parameter, $R_V$, the shape of the 2175 Å bump and the slope of the UV extinction curve is predictable for most lines of sight. This single parameter is defined as the ratio of $B-V$ color excess, $\mathrm{E}(B-V)$, to total $V$-band extinction, $A_V$:

$$R_V = \frac{\mathrm{E}(B-V)}{A_V} \,, \tag{0.14}$$

and can be understood as the ratio of selective to total extinction. Based on the findings of Cardelli *et al.* (1989), we can write the extinction in any set of UV, optical or NIR bands as

$$\vec{A} = \vec{R}(R_V)\,\mathrm{E}(B-V) \,, \tag{0.15}$$

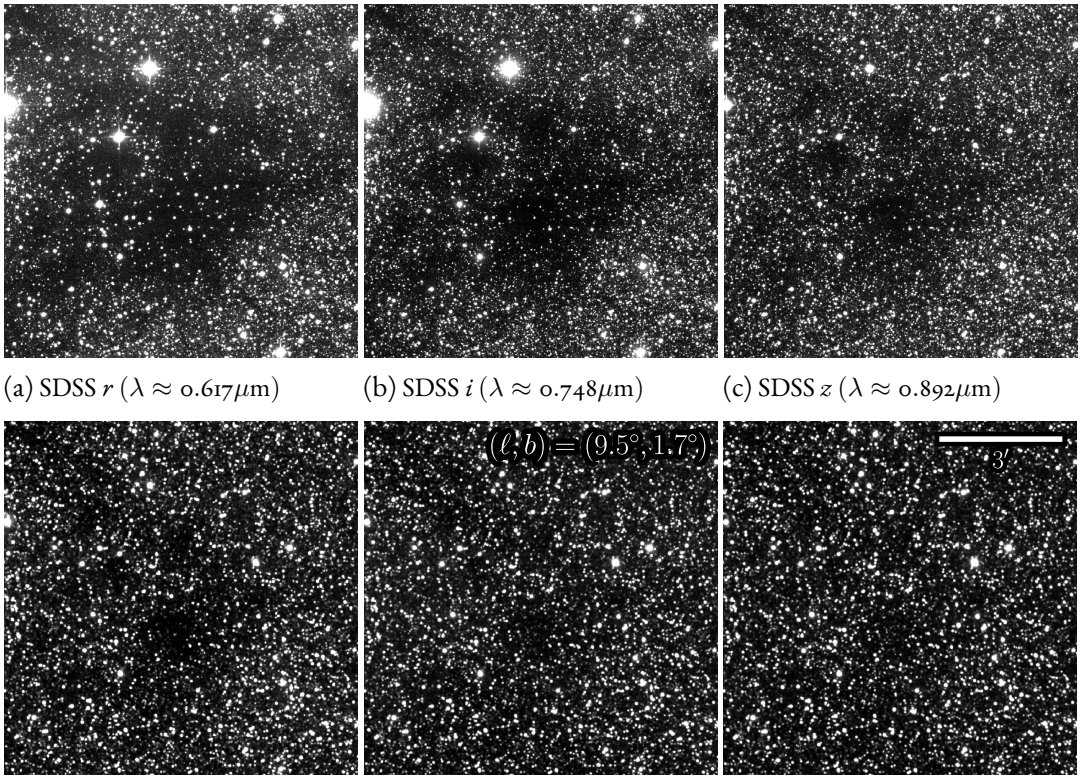


(a) SDSS $r$ ($\lambda \approx 0.617\mu$m) (b) SDSS $i$ ($\lambda \approx 0.748\mu$m) (c) SDSS $z$ ($\lambda \approx 0.892\mu$m)

(d) 2MASS $J$ ($\lambda \approx 1.24\mu$m) (e) 2MASS $H$ ($\lambda \approx 1.66\mu$m) (f) 2MASS $K_s$ ($\lambda \approx 2.16\mu$m)

Figure 0.5: An interstellar cloud at six wavelengths in the optical and NIR. The cloud extinguishes a greater fraction of the background starlight at shorter wavelengths. The imprint of the cloud is therefore strongest in the SDSS $r$ photograph, and weakest in the 2MASS $K_s$ photograph.

where $\vec{R}$ encodes the response of all the bands to a given color excess $E(B-V)$, and is, to first approximation, dependent only on the quantity $R_V$. In the bulk of this thesis, we make the simplifying assumption that all dust follows the same, "average" Milky Way extinction law, with $R_V = 3.1$. As will be seen, there is evidence that this approximation is very rough indeed, but since fitting dust properties throughout space adds an additional layer of complexity, it is left for future work.

The observable effect of dust in the optical and NIR can be seen in Fig. 0.5, which shows the same stellar field, deep in the plane of the Galaxy, imaged in six different passbands, spanning the

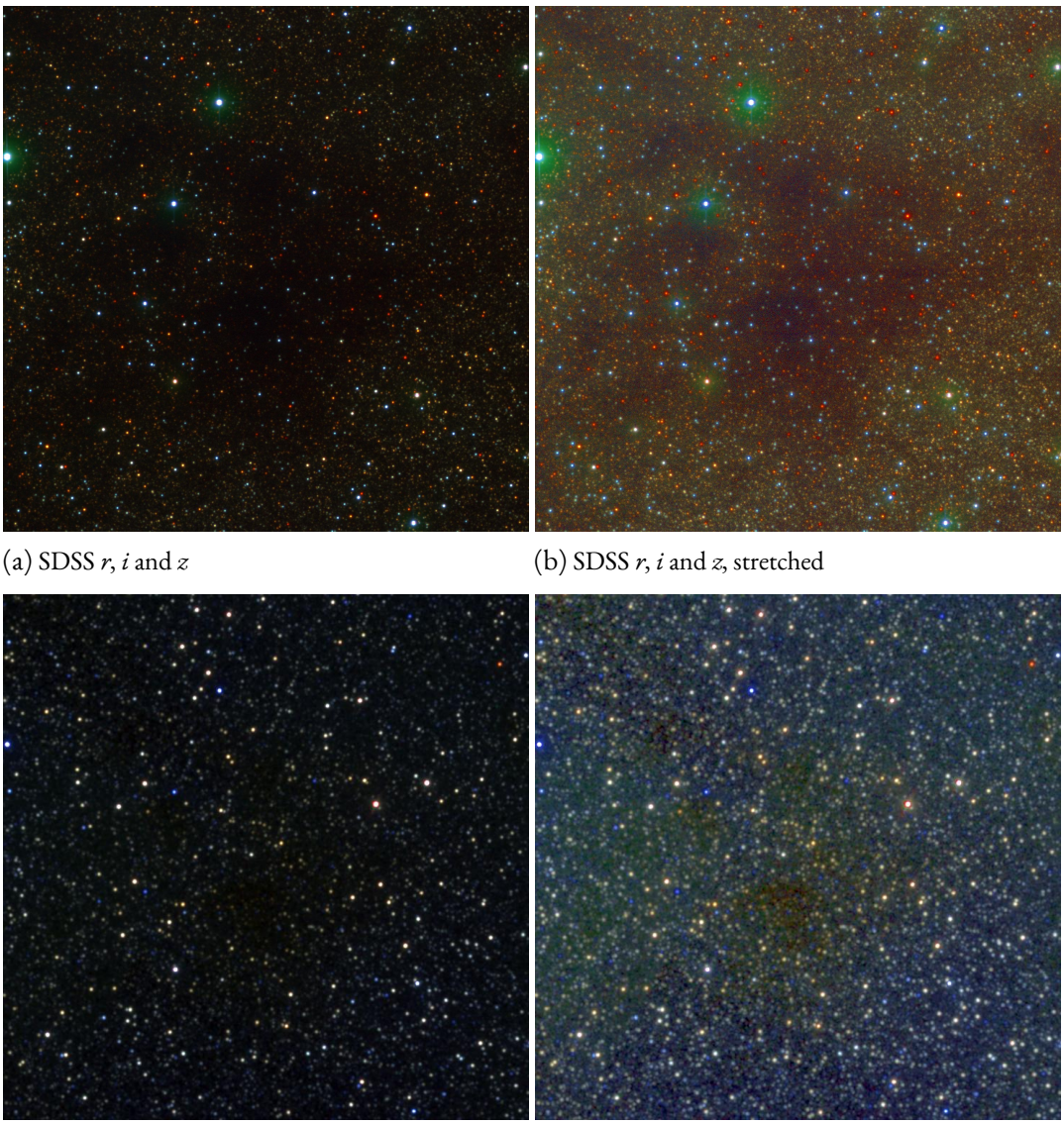

(a) SDSS $r$, $i$ and $z$

(b) SDSS $r$, $i$ and $z$, stretched

(c) 2MASS $J$, $H$ and $K_s$

(d) 2MASS $J$, $H$ and $K_s$. stretched

Figure 0.6: The same cloud as in Fig. 0.5, but in color. In the top panels, each image shows the SDSS $r$, $i$ and $z$ passbands as blue, green and red, respectively. In the bottom panels, the same is done for the 2MASS $J$, $H$ and $K_s$ passbands. In both cases, the longest-wavelength passband is mapped to the red channel, and the shortest-wavelength passband is mapped to the blue channel. In the right panels, the image intensity is stretched in order to boost faint stars. As can be seen, stars lying behind the core of the cloud look redder, on average, than stars elsewhere in the frame.

optical and the NIR. A cloud with $E(B-V) \sim 2.5$ mag blocks out a large fraction of foreground stars in the "bluest" passband (i.e., the shortest-wavelength passband), but far fewer stars in the "reddest" passband (i.e., the longest-wavelength passband). This is due to the decrease in dust optical depth with increasing wavelength through the optical and NIR (see Fig. 0.4). Thus, while in the bluest pictured passband, SDSS *r*, the dust in the interstellar cloud extinguishes stellar light from an extended area, in the reddest pictured passband, 2MASS $K_s$, only the dense core of the cloud blocks out a significant fraction of stars.

A different way of visualizing this effect is to look at the change in color of stars behind a dust cloud. As the dust has greater optical depth for blue light than red light, stars behind the cloud appear not only fainter, but redder, an effect termed "reddening." This effect can be seen in Fig. 0.6, which shows the exact same field as Fig. 0.5, but with the different passbands mapped to the blue, green and red channels of the images. In each panel of Fig. 0.6, the shortest-wavelength passband is mapped to the blue channel, and the longest-wavelength passband to the red channel. The intrinsic colors of stars vary, but on average, the stars in regions of space obscured by dust appear redder than their counterparts away from the dust cloud.

## 0.3 Two-Dimensional Dust Maps

While this thesis focuses on the three-dimensional distribution of dust throughout the Galaxy, it is helpful to review some of the methods that have been used in the past to map dust in two dimensions. Here, I will focus on just a few works which span a range of dust-mapping techniques, rather than attempting to give a comprehensive listing of all dust mapping efforts.

One of the earliest prescriptions for accounting for dust was to treat it as a thin, flat slab in the midplane of the Milky Way, extending out to infinite distance in the all but the vertical direction. Given a slab height $h$, and extinction per unit distance of $\kappa$, the total extinction (out to infinite distance) at Galactic latitude $b$ would be given by

$$A = \frac{h\kappa}{2} \csc(b) \ . \tag{0.16}$$

This was often formulated as

$$A = A_0 \csc(b) \ , \tag{0.17}$$

which obviates the need to know the slab height or rate of extinction, combining these two terms into a single quantity, equal to the extinction at the Galactic poles (Burstein & Heiles 1978a). Given the highly non-uniform nature of the interstellar medium, the slab model is a brutal approximation.

### 0.3.1 Burstein & Heiles

Recognizing the inadequacy of the slab model of dust, Burstein & Heiles (1978a,b) developed a new method for mapping reddening across the sky, based on a combination of neutral atomic hydrogen (HI) column density and galaxy counts. If gas and dust in the Galaxy are well mixed, and HI makes up a constant fraction of the gas, then HI column density will be a good proxy of dust column density, and by extension, extinction. If galaxies are uniformly distributed and have similar properties (e.g., a similar distribution of luminosities) across the sky, then an under-abundance of galaxies in

one region of the sky is indicative of interstellar extinction.

Both of these proxies for extinction suffer from difficult systematics. The gas-to-dust ratio varies throughout the galaxy, making HI column density a very imperfect proxy for dust column density. Dust properties (e.g., the grain-size distribution and the PAH abundance) vary as well, meaning that the same column density of dust does not necessarily translate into the same magnitude of extinction in two regions of the sky. Galaxy counts suffer from two effects: large noise due to small-number Poisson statistics, and galaxy clustering, deriving from the large-scale structure of the universe, which violates the assumption that galaxy positions are uncorrelated and increases the occurrence of regions with anomalously high or low counts. Thus, a map that traces dust extinction with HI column density may, in reality, trace the gas-to-dust ratio, while a map that uses galaxy counts may instead trace cosmological large-scale structure.

Burstein & Heiles (1978a,b) take several steps to mitigate these systematics. First, galaxy counts from the Shane–Wirtanen galaxy survey (Shane & Wirtanen 1967) are smoothed on 13° scales, reducing the impact of galaxy clustering. In order to find a good proxy for reddening, Burstein & Heiles (1978a,b) then look for a combination of galaxy counts and HI column density which correlates best with the reddening of a set of calibrators. Two sets of calibrators are used: RR Lyrae stars, for which a period-luminosity-color relation is available, and globular clusters, for which several good methods of determining reddening exist. Each of these calibrators trace reddening, rather than extinction, making the resulting map a reddening map. While there is large scatter in the relationship between reddening and HI column density alone, or between reddening and galaxy counts alone, Burstein & Heiles (1978a,b) find a function of both proxies with smaller scatter. Burstein & Heiles (1982)

presents the resulting map, and evaluates its accuracy as 10% outside of the plane of the Galaxy. The map is not homogeneous across the entire sky: the Shane & Wirtanen (1967) galaxy survey does not cover equatorial declinations $\delta \leq -23°$, and the gas-to-dust ratio is assumed to be relatively constant at Galactic latitudes $b \geq 65°$, obviating the need to use galaxy-count correction (Burstein & Heiles 1982).

The resulting map was a great advance over the simple slab models in common use at the time, and could be rightly viewed as representing the dawn of serious dust mapping. As can be seen in the top panels of Figs. 0.7 and 0.8, the Burstein & Heiles (BH) map shows Galactic structure that varies in a non-trivial way across the sky, and which is not well captured by any simple mathematical prescription.

### 0.3.2 Schlegel, Finkbeiner & Davis

Dust in the diffuse interstellar medium has a typical temperature of $\sim$20 K. The larger dust grains therefore radiate thermally in the FIR, with emission peaking in the range 100 $\mu$m to 200 $\mu$m (Li & Draine 2001). From the ground, this FIR emission is unobservable, because of the enormous ambient thermal background produced by the telescope itself, the telescope dome and the atmosphere. In 1983, NASA, in collaboration with the Netherlands and UK, launched the Infrared Astronomical Satellite (IRAS), which conducted the first-ever all-sky infrared survey from space (Neugebauer *et al.* 1984; Lemke 2009; Low *et al.* 2007). IRAS had a 0.57 m aperture, and was cryogenically cooled by an onboard liquid helium reservoir, with the mirrors at $<$ 10 K and the focal plane at $<$ 3 K. This enabled IRAS to survey more than 95% of the sky in four passbands, centered on 12, 25, 60 and 100 $\mu$m

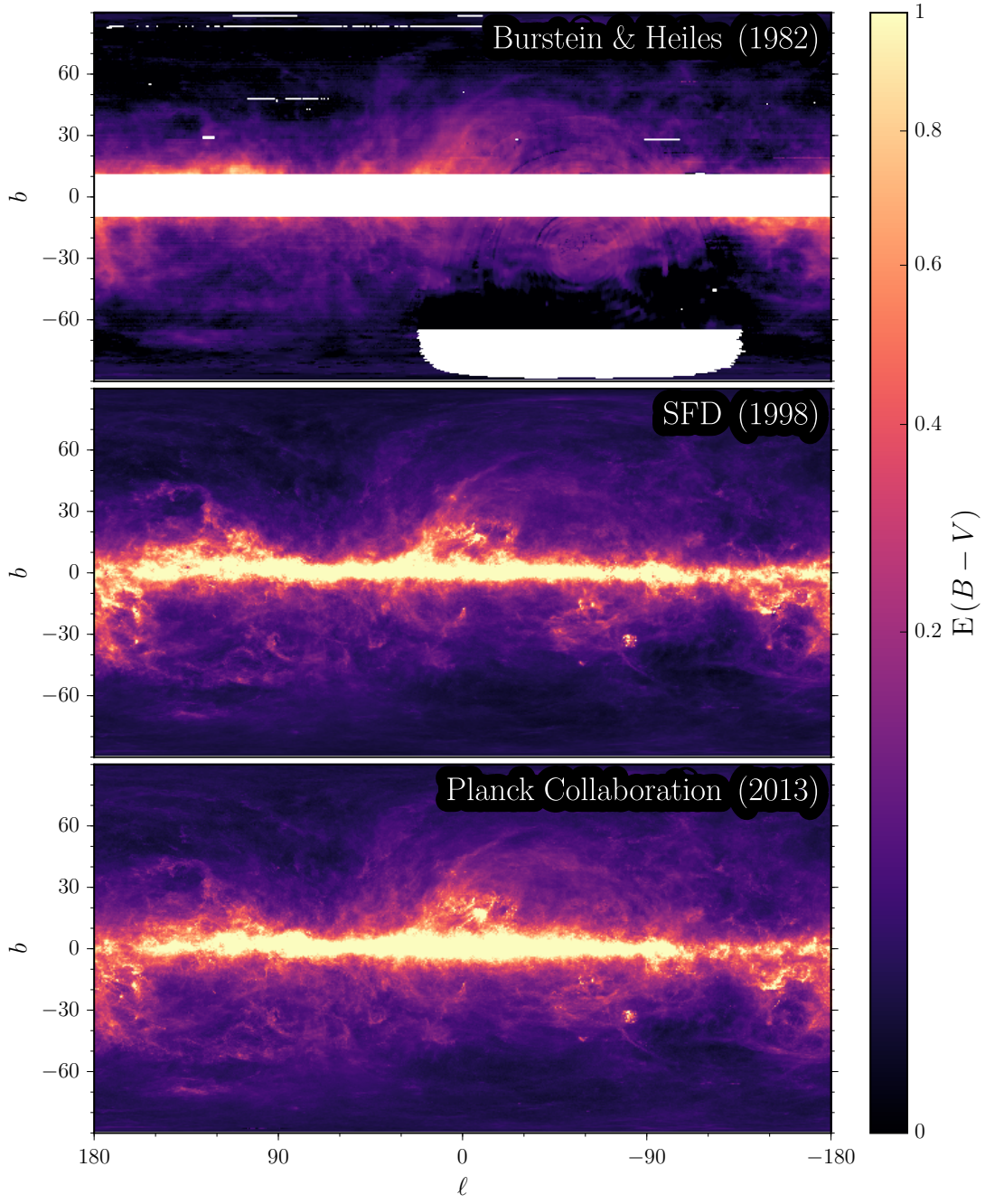


Figure 0.7: Three generations of two-dimensional emission-based maps of dust reddening. These three maps, discussed in the text, show the progression of dust mapping over time.

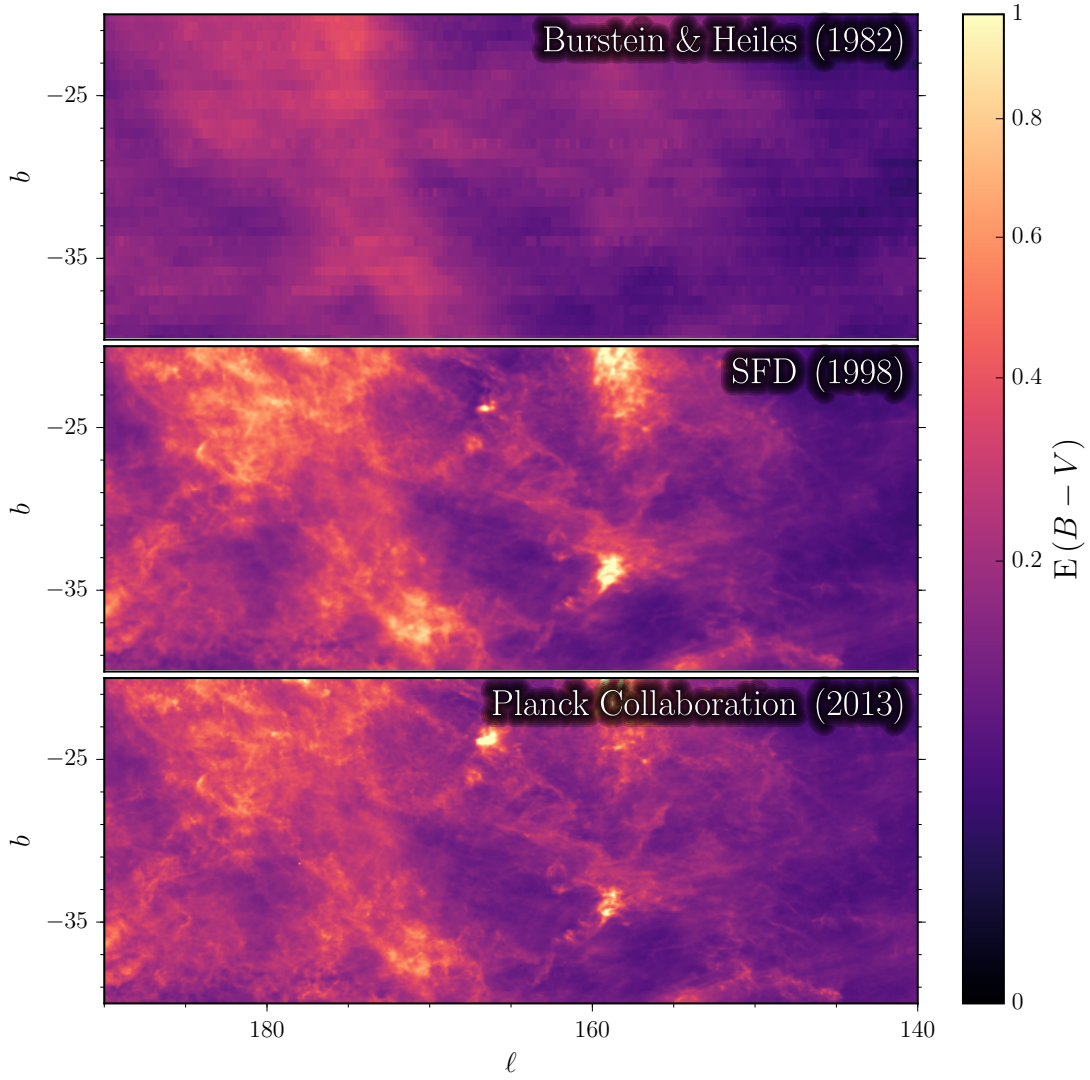


Figure 0.8: A detailed view of three generations of two-dimensional emission-based maps of dust reddening. The difference in resolution between the earliest dust map, Burstein & Heiles (1982), and more recent maps is stark. The differences between the latter two maps, Schlegel *et al.* (1998, SFD) and Planck Collaboration (2015) are more subtle. As discussed in the text, the low-resolution temperature correction in SFD leads to smearing of cold filamentary structures, which are captured in greater detail by the Planck dust maps.

(Neugebauer *et al.* 1984). The availability of maps of the FIR sky allowed a more direct approach to mapping dust, which did not rely on estimation of uncertain gas-to-dust ratios.

Schlegel *et al.* (1998, hereafter "SFD") maps dust by carefully modeling FIR dust emission at 100 and 240 $\mu$m. SFD relies on 100 $\mu$m IRAS data, as well as 100 and 240 $\mu$m data from the Dust Infrared Background Experiment (DIRBE), an instrument aboard the Cosmic Background Explorer (COBE) satellite (Boggess *et al.* 1992). This work is complicated by the uncertain emission properties of dust and several foregrounds and backgrounds, including zodiacal light emitted by dust grains in our Solar system, extragalactic background radiation and foreground point sources. The zodiacal light, in particular, is extremely difficult to model. "Interplanetary dust" (IPD) within the Solar system is arranged non-trivially in three dimensions and heated differentially by the Sun, and our view through the IPD changes as we orbit the Sun. Due to its proximity to the Sun, the IPD is significantly hotter ($\sim 280$ K) than interstellar dust, but has a much smaller total column density. This combination means that the IPD radiates significantly in the FIR, but contributes only negligible extinction, on the level of $\sim 10^{-6}$ mag at optical wavelengths (Schlegel *et al.* 1998).

SFD takes an empirical approach to removing the zodiacal light, cleaning DIRBE images at each observation epoch by finding the function of 25 $\mu$m DIRBE emission which, when subtracted from the 100 or 240 $\mu$m DIRBE maps, maximizes the correlation of the latter with high-Galactic-latitude 21 cm HI emission maps. This process rests on the fact that 25 $\mu$m emission is the best tracer of zodiacal light, and that HI column density is expected to correlate well with diffuse dust column density at high Galactic latitudes (recall that this was the basis for the Burstein & Heiles maps). Interestingly, this process leads to a measurement of the Cosmic Infrared Background zero-point, perhaps the first

measurement of this quantity. SFD additionally cleans the IRAS maps, and creates a hybrid IRAS–DIRBE 100 $\mu$m map, which combines large-scale information from the zodiacal-light-corrected DIRBE maps and small-scale information from the IRAS 100 $\mu$m map, which has much better angular resolution.

In order to determine dust column density, which can be translated into dust reddening, SFD models the 100 and 240 $\mu$m FIR emission as a modified blackbody. Dust is assumed to radiate with intensity

$$I_\nu(\nu,\ T) = \sigma_{\rm dust}\, \kappa_\nu(\nu)\, B_\nu(\nu,\ T)\ , \tag{0.18}$$

where $B_\nu(\nu,\ T)$ is the Planck blackbody spectrum, $\kappa_\nu(\nu)$ is a wavelength-dependent opacity, and $\sigma_{\rm dust}$ is the line-of-sight dust column density. As dust emits inefficiently at wavelengths larger than the grain size, the dust opacity should decrease at high frequencies – SFD assumes $\kappa_\nu \propto \nu^2$. SFD applies this model to the DIRBE 100 and 240 $\mu$m maps in order compute a map of dust temperature, with an angular resolution of 0.7°. SFD then uses this temperature map, in conjunction with the hybrid IRAS–DIRBE 100 $\mu$m map to determine dust column density on 6.1′ angular scales.

SFD translates dust column densities into reddening by calibrating against a set of 389 elliptical galaxies with E($B-V$) determinations (derived from a $Mg_2$ abundance – color relation). The resulting map is plotted in the second panel of Figs. 0.7 and 0.8. SFD has several advantages over BH, including its much finer angular resolution and the fact that it is more directly tied to dust, rather than inferring dust through the intermediary of HI column density. SFD, and the recalibrated version of

Schlafly & Finkbeiner (2011), are now standard tools in astronomy for making dust corrections, and therefore widely cited.

### 0.3.3 Planck Collaboration

The basic method employed by SFD has been applied to newer datasets as well. The *Planck* satellite, which launched in 2009 and operated until 2013, surveyed the sky in a large number of bands, spanning the wavelength regime $\sim$300 $\mu$m to $\sim$1 cm. The primary goal of *Planck* was to measure the anisotropy of the Cosmic Microwave Background (CMB), in order to constrain cosmological models (Planck Collaboration 2011). In order to complete this goal, however, the Planck Collaboration had to separate out the CMB from various foregrounds, including thermal dust emission. The Planck Collaboration has therefore published a series of dust models. Planck Collaboration (2014) fits dust as a modified blackbody, in a similar manner to SFD, to *Planck* and IRAS data. Planck Collaboration (2015) fits a set of foreground components, including dust thermal emission, to a combination of *Planck*, WISE[¶] and 408 MHz data in a self-consistent manner. Planck Collaboration (2016) fits the free parameters of a more physically motivated model of dust by Draine & Li (2007), using a combination of *Planck*, WISE, DIRBE and IRAS data.

The Planck Collaboration (2014) dust map is plotted in the bottom panels of Figs. 0.7 and 0.8. Although similar in nominal resolution to SFD, the Planck dust maps trace cold cloud cores and filaments in the interstellar medium somewhat better. This is because while SFD derived dust col-

[¶] The Wide-field Infrared Survey Explorer (Wright *et al.* 2010, WISE) is a space telescope that completed an all-sky MIR survey between 2010 and 2011, but which was reactivated in 2013 in order to conduct a search for near-Earth asteroids and comets (Mainzer *et al.* 2011, 2014).

umn densities from a 100 $\mu$m map with 6.1′ resolution, the temperature correction in SFD is derived from DIRBE maps with 0.7° resolution. Cold cloud cores and filaments are therefore surrounded by a halo of low temperature in the SFD temperature maps. In order to achieve the same intensity at lower temperature, SFD therefore has to infer the presence of a larger column density in the surroundings of these filaments. This has the effect, in SFD, of creating a halo of increased reddening around cold, dense features in the interstellar medium.

### 0.3.4 NICE, NICER, NICEST

The preceding dust maps relied on either FIR emission (in the case of SFD and *Planck*) or HI emission (in the case of BH) to trace dust column, and then used extragalactic sources with predictable intrinsic color to derive a calibration from dust column to reddening. The implicit assumption in such techniques is that there is some standard relation between the FIR thermal emission properties of dust and its UV, optical and NIR absorption and scattering properties. Additionally, we would expect dust column density to be more correlated with dust extinction than with reddening, yet the preceding maps use reddening calibrators, rather than extinction calibrators. This is for good reason – reddenings are easier to obtain, because they do not require precise *absolute* photometry, but rather only precise *relative* photometry between different passbands. Nevertheless, because of these deficiencies in emission-based maps, the idea of mapping dust reddening using some dense population of reddening tracers is appealing. Even a glance at Fig. 0.6 should convince one that stellar colors provide a promising means of tracing dust.

Lada *et al.* (1994) does just this, mapping dust reddening by way of NIR color measurements of stars, a technique termed the "Near-Infrared Color Excess" (NICE) method. The central idea of NICE is that most stars have fairly similar NIR $H-K$ colors. Denote the true $H-K$ color of a given star by $(H-K)^{\rm tr}$. The observed color of the star is then

$$(H-K)^{\rm obs} = (H-K)^{\rm tr} + k_{HK} A_V \,, \tag{0.19}$$

where $k_{HK}$ is the scaling between total $V$-band extinction and $H-K$ color excess. For any given point on the sky, NICE estimates the extinction as

$$\hat{A}_V = \frac{1}{k_{HK} N} \sum_{n=1}^{N} \left[ (H-K)_n^{\rm obs} - \left\langle (H-K)^{\rm tr} \right\rangle \right] \,, \tag{0.20}$$

where the sum is taken over all stars within some chosen angular distance. Increasing the angular distance reduces noise by averaging over more stars, but also reduces the angular resolution of the map. While NICE technically reports an extinction, it is, in essence a reddening map, as extinction has simply been obtained by scaling an estimated $H-K$ color excess.

Lombardi & Alves (2001) notes two major problems with NICE – the intrinsic scatter in $(H-K)^{\rm tr}$ is unaccounted for, and stars cannot all be assumed to lie behind all the dust – and develops a more robust technique, termed the "Near-Infrared Color Excess method Revisited" (NICER). This method makes use of an arbitrary number of passbands, making the assumption that in each pair

$i$ of passbands, the observed color, $c_i^{\rm obs}$, is related to the true color, $c_i^{\rm tr}$, by

$$c_i^{\rm obs} = c_i^{\rm tr} + k_i A_V + \epsilon_i \,. \tag{0.21}$$

As before, $k_i$ is the ratio of color excess in color $i$ to $A_V$. The term $\epsilon_i$ is the photometric error in color $i$, and will be different for each observation of each star. Taking care to consider both the covariance of photometric errors, $\mathrm{Cov}_{ij}(\epsilon)$, and the covariance in true stellar colors, $\mathrm{Cov}_{ij}(c^{\rm tr})$, NICER determines the minimum-variance unbiased estimator of the form

$$\hat{A}_V = \sum_{i=1}^{N_{\rm colors}} b_i \, c_i^{\rm obs} \,. \tag{0.22}$$

The coefficients $b_i$ turn out to be a function of the covariances mentioned above, as well as the vector $\vec{k}$ (encoding $k_i$ in each color). NICER similarly returns an estimate of the variance in $\hat{A}_V$ for each star.

NICER transforms individual stellar extinction estimates into a smooth extinction map in a similar manner to NICE. At any given point in space, NICER estimates extinction from a weighted average of stellar extinctions. The weight contains an angular smoothing kernel, which determines the effective resolution of the map, and the inverse variance of each star, down-weighting stars with more uncertain extinction estimates.

As dust and stars fill a three-dimensional volume, one cannot, in general, assume that all stars in a given direction on the sky suffer the same extinction. However, above or below the plane of the

Galaxy, there is often only one dense cloud along a given line of sight, making it a decent approximation to assume that all stars are either in front of or behind a single screen of dust. Because the scale height of stars in the plane of the Galaxy is larger than the scale height of the dust, more stars are generally behind the dust than in front of it (this assumption can break down, however, if the dust is optically thick enough to block out most background stars). NICER therefore attempts to deal with the 3D nature of dust by assuming that some fraction of stars are in the foreground, and attempting to remove those stars from the extinction estimate. This is achieved by iterating the NICER procedure, clipping stars with anomalous $\hat{A}_V$ estimates after each step.

While this procedure quickly converges and will in many cases effectively remove foreground stars, it breaks the fundamental assumption that the calculated map of $\hat{A}_V$ is a smoothed version of the true, full-resolution extinction map. In regions with complicated dust structure that varies on small angular scales, NICER's $\sigma$-clipping procedure may systematically cull stars from certain small regions of the sky, on scales smaller than the smoothing kernel. An additional problem which confronts NICER is the fact that stars themselves are not observed equally in high- and low-extinction regions of the sky. If a narrow filament of dust runs through a given region of the sky, fewer stars will be observed behind the filament than away from the filament, due to differential extinction. This will have the effect of biasing maps produced by NICER towards lower extinctions, especially in more complicated regions of the sky. In order to deal with the twin problems of foreground stars and biases deriving from small-scale extinction variations, Lombardi (2009) develops a more principled method, which gives more weight to stars behind a greater column of dust. This method is termed, appropriately, NICEST. A detailed description of this method, which is considerably more

sophisticated than that of NICE and NICER, is beyond the scope of this introduction. Foster *et al.* (2008) develops an additional extension to NICER, which uses not just the colors of stars, but also of galaxies to trace reddening. This method is called "GNICER," with the "G" standing for "galaxies."

## 0.4 Three-Dimensional Dust Maps

As we have seen, a variety of methods have been developed to map extinction and reddening across the sky. However, it is the last family of methods, NICE/NICER/NICEST, which point towards the method used in this thesis for determining the three-dimensional distribution of dust throughout the Galaxy.

The principle upon which NICE, NICER and NICEST work is that stars, due to the effect that dust has on their appearance, can trace the distribution of dust throughout the Galaxy. As stars are distributed in three dimensions throughout the volume of the Milky Way, however, it is possible to use them as tracers not just of the total integrated column of dust across the sky, but rather as tracers of the density of dust throughout space. Whereas NICE, NICER and NICEST treat the dust as a screen that the stars lie behind, we will treat the dust as a field in which the stars are embedded. This requires us to model the distance to each star, as well as the column of dust that lies in front of it. The dust column is measured on the basis of the extinction and reddening it applies to stellar photometry, but as we do not know the intrinsic luminosity and color of any given star in a photometric survey, we are required to infer the star's spectral type at the same time that we infer the distance and dust column. In order to produce a three-dimensional dust map, we therefore have to model the

distance and spectral type of stars, as well as the distribution of dust in one self-consistent model.

I am not the first work to pursue this type of work. Marshall *et al.* (2006) developed a method that iteratively improves distance and reddening estimates to post-main sequence stars, updating the dust column in each distance bin with each iteration so that the intrinsic stellar colors match those predicted by the Besançon model of the Galactic stellar population (Robin *et al.* 2003). Marshall *et al.* (2006) applied this method to 2MASS photometry of the Galactic plane, producing a three-dimensional reddening map out to a distance of several kiloparsecs in the region $|b| < 10°$, $-100° \leq \ell \leq 100°$. A number of groups have pursued methods that determine maximum-likelihood parameters for the stars along each sightline, combining the estimates in each sightline into a distance-reddening relation. Berry *et al.* (2012) applied such a method to SDSS photometry, producing a 3D reddening map and measuring variation in the dust extinction spectrum across the SDSS footprint. Chen *et al.* (2014) used optical XSTPS-GAC, NIR 2MASS and MIR WISE photometry to produce a 3D reddening map of the Galactic anticenter. Sale (2012) developed a probabilistic framework to simultaneously infer stellar parameters and the dust extinction distribution along each line of sight, and Sale *et al.* (2014) applied this method to IPHAS photometry of the northern Galactic plane. Hanson & Bailer-Jones (2014) developed a similar probabilistic framework for inferring stellar types, distances and dust foreground properties, and applied this method to SDSS and UKIRT Infrared Deep Sky Survey (UKIDSS) photometry in regions of the high-Galactic-latitude sky. Lallement *et al.* (2014) took a somewhat different approach, using $\sim 23,000$ stellar parallaxes and reddening estimates from a number of sources to infer the 3D distribution of dust opacity out to a distance of 800 - 1000 pc in the plane of the Galaxy, and $\sim$300 pc out of the plane.

The work of Lallement *et al.* (2014) is particularly interesting, in that it explicitly takes into the account that dust is spatially smooth, placing a prior on correlations in the dust density field. Vergely *et al.* (2001) and Lallement *et al.* (2003) pursue a conceptually similar method of mapping out the distribution of dust, mapping out the "Local Bubble" (i.e., the local interstellar medium, believed to be under-dense) by measuring absorption lines imprinted by the interstellar medium on the spectra of stars with parallaxes from the *Hipparcos* satellite (ESA 1997).

This thesis ties together work laid out in Green *et al.* (2014, 2015), which developed the methodology used here, and then released the 3D map featured in this thesis, respectively. Within the Finkbeiner research group at Harvard, we have conducted additional work on three-dimensional dust mapping. Schlafly *et al.* (2014a) presented a map of dust reddening integrated to 4.5 kpc, covering three quarters of the sky, based on applying this method to optical Pan-STARRS 1 stellar photometry. Using this same 3D mapping technique, Schlafly *et al.* (2015) found that the Orion molecular complex appears to form part of a larger bubble structure. Finally, Schlafly *et al.* (2014b) determined the distance to a large number of molecular clouds by applying a related method to Pan-STARRS 1 stellar photometry.

*Now since there is illimitable space empty in every direction, and since seeds innumerable in number in the unfathomable universe are flying about in many ways driven in everlasting movement, it cannot by any means be thought likely that this is the only round earth and sky that has been made, that all those bodies of matter without do nothing: especially since this world was made by nature, and the seeds of things themselves of their own accord, knocking together by chance, clashed in all sorts of ways, heedless, without aim, without intention, until at length those combined which, suddenly thrown together, could become in each case the beginnings of mighty things, of earth and sea and sky and the generations of living creatures.*

Lucretius, *de rerum natura*, 2.1052–1063

# 1

# Method

The goal of this thesis is to develop a method for inferring the three-dimensional distribution of dust throughout the Galaxy, and then to apply it to photometric data in order to produce a map. This chapter lays out just such a method, beginning with § 1.1, which details the mathematical formalism underpinning this mapping technique. Going into more detail, § 1.2 describes the model used to describe individual stars, while § 1.3 explains

the model used to describe the distribution of dust throughout space. Extensions to the model that render it more realistic and robust are described in § 1.4. In § 1.5, I explain how to sample from the resulting model of stars and dust. Finally, § 1.6 gives a concise summary of the model, while § 1.7 describes how additional information about individual stars can be extracted from the 3D dust map that will be produced.

## 1.1 Line-of-Sight Reddening Profile

Here, I lay out the basic method used in this thesis for inferring the three-dimensional distribution of dust in the Milky Way. A number of basic assumptions of our model should be stated at the outset. The most basic assumption is that stars which are close to one another in 3D space lie behind the same column of dust from our perspective in the Solar system. A consequence of this principle is that by grouping together stars which are angularly close to one another on the sky, we obtain a sample of stars that trace the same column of dust. Along one sightline, therefore, stars that are at greater distance are behind a greater column of dust, and are thus extinguished and reddened to a greater extent. This allows us to group stars into small angular pixels, and then use stars within each pixel as tracers of the dust column to different distances along the given sightline. So long as the dust column does not vary significantly over small angular scales, then this is procedure is approximately correct.

A second assumption is that the extinction properties of dust are uniform throughout the Galaxy. As discussed in § 0.2, the extinction spectrum of dust is determined by a number of factors, including the grain-size distribution, the dielectric response function of the grain material and the

abundance of chemical species with certain absorption lines (e.g., the $\pi \rightarrow \pi^{\star}$ transition in PAH molecules). The wavelength–extinction relation has been determined for individual stars using the "pair method" (discussed in § 0.1 in the context of Robert Trumpler's pioneering work on interstellar dust), revealing significant deviation from the average Milky Way extinction law (See Draine 2003 for a brief introduction to variation in dust extinction). However, the assumption of uniform dust properties, while being a rough approximation, significantly simplifies the problem of creating a 3D dust map. Future work will certainly relax this assumption, but as will be shown in the remainder of this thesis, significant progress can be made with relatively simplified models of the more complex reality.

The strategy pursued in this thesis for inferring the 3D structure of dust in the Milky Way is therefore as follows. A three-dimensional dust map is constructed pixel-by-pixel from independently determined line-of-sight reddening profiles. Stars are grouped into sightlines with typical angular scales of $\sim 6.8'$. The reddening, distance and type of each star is then determined independently. Assuming that the distances and reddenings of the stars in a given line of sight lie along a single profile, with reddening increasing monotonically with distance, I then sample from the posterior density of distance–reddening profiles, returning the uncertainty in the line-of-sight reddening in the pixel. By repeating this process in each angular pixel, I obtain the 3D distribution of dust throughout the Milky Way, out to a distance of several kiloparsecs.

Let us denote the reddening profile along a particular sightline by

$$E(\mu\,;\,\vec{\alpha})\ , \tag{1.1}$$

where $E$, the color excess in some pair of passbands (e.g., E$(B-V)$ for $B$ and $V$ bands), is a function of distance modulus $\mu$, and $\vec{\alpha}$ denotes any fitting parameters defining the distance–reddening profile. For example, $\vec{\alpha}$ could encode the dust density in each distance bin, and could in principle include the value of $R_V$, which parameterizes the wavelength dependence of the extinction law (Cardelli *et al.* 1989; Fitzpatrick 1999). The extinction $\vec{A}$ in any set of passbands is then assumed to be a function of the reddening, which we denote by $E$, and $R_V$, which will be held fixed in this work:

$$\vec{A} = \vec{A}(E, R_V)\ . \tag{1.2}$$

Along one line of sight, denote the photometry of star $i$ by $\vec{m}_i$, and the set of all observed stellar magnitudes by $\{\vec{m}\}$. We wish to determine how the model parameters $\vec{\alpha}$ for the line-of-sight reddening profile depend on the stellar photometry $\{\vec{m}\}$. That is, we wish to determine

$$p(\vec{\alpha}\,|\,\{\vec{m}\})\ . \tag{1.3}$$

Using Bayes' rule,

$$p(\vec{\alpha} \mid \{\vec{m}\}) = \frac{p(\{\vec{m}\} \mid \vec{\alpha})\, p(\vec{\alpha})}{p(\{\vec{m}\})}\,. \tag{1.4}$$

The likelihood, $p(\{\vec{m}\} \mid \vec{\alpha})$, is the probability density of obtaining the set of observed magnitudes $\{\vec{m}\}$, given the reddening profile defined by $\vec{\alpha}$.

The *evidence*, $p(\{\vec{m}\})$, remains constant as we vary $\vec{\alpha}$, since it depends only on the observed stellar apparent magnitudes, $\{\vec{m}\}$. Conceptually, the idea of assigning a probability density to our *observations* might seem strange. One should think of this term, however, as the probability density of the observed stellar apparent magnitudes being generated by our model of the structure of the Milky Way. If we were to simulate stellar observations for an infinite number of Milky-Way-like galaxies, with statistically equivalent three-dimensional distributions of stars and dust, the simulated datasets would populate a space of possible datasets. Some regions of this dataset-space would be more densely populated than others. The evidence, $p(\{\vec{m}\})$, is the density of simulated datasets in the region of our actual observed dataset. In other words, it tells us whether the data we observe is "typical" of what we would observe, were our statistical model of the Galaxy correct. The evidence is therefore a conceptually interesting term, but since it only enters into our problem as a normalizing constant, we can disregard it in the following.

The likelihood of the entire set of stellar observations is just the product of the individual likeli-

hoods, i.e.

$$p(\{\vec{m}\} \,|\, \vec{\alpha}) = \prod_i p(\vec{m}_i \,|\, \vec{\alpha}) \ . \tag{1.5}$$

This is just a statement that the photometry of one star does not influence the photometry of any other star – a good assumption if the stars are not strongly blended in our imaging, and if stars are not clustered in three-dimensional space. Plugging Eq. (1.5) into Eq. (1.4), and dropping the normalizing factor $p(\{\vec{m}\})$,

$$p(\vec{\alpha} \,|\, \{\vec{m}\}) \propto p(\vec{\alpha}) \prod_i p(\vec{m}_i \,|\, \vec{\alpha}) \ . \tag{1.6}$$

We now introduce nuisance parameters describing the distance to and intrinsic type of each star, and then marginalize over these parameters to obtain the likelihood. Denote the distance modulus to star $i$ by $\mu_i$, and the parameters describing the stellar type by $\vec{\Theta}_i$. For an individual star,

$$\begin{aligned} p(\vec{m} \,|\, \vec{\alpha}) &= \int \mathrm{d}\mu \, \mathrm{d}\vec{\Theta} \, p\Big(\vec{m}, \mu, \vec{\Theta} \,|\, \vec{\alpha}\Big) & (1.7) \\ &= \int \mathrm{d}\mu \, \mathrm{d}\vec{\Theta} \, p\Big(\vec{m} \,|\, \mu, \vec{\Theta}, \vec{\alpha}\Big) \, p\Big(\mu, \vec{\Theta} \,|\, \vec{\alpha}\Big) & (1.8) \\ &= \int \mathrm{d}\mu \, \mathrm{d}\vec{\Theta} \, p\Big(\vec{m} \,|\, \mu, \vec{\Theta}, E(\mu; \vec{\alpha})\Big) \, p\Big(\mu, \vec{\Theta}\Big) \ . & (1.9) \end{aligned}$$

In the last step, we have assumed that the joint prior on the distance and intrinsic stellar type are independent of the reddening profile. Up to a normalizing constant, the above integrand is equivalent

to the posterior density

$$p\left(\mu, E, \vec{\Theta} \mid \vec{m}\right) \tag{1.10}$$

for an individual star, where the prior on $E$ is flat. Intuitively, this is because the prior on reddening is on the fitting parameters $\vec{\alpha}$, rather than the reddening of an individual star. After marginalizing over the stellar type $\Theta$,

$$p(\vec{m} \mid \vec{\alpha}) \propto \int \mathrm{d}\mu \; p(\mu, E(\mu; \vec{\alpha}) \mid \vec{m}) \; . \tag{1.11}$$

Plugging the above into Eq. (1.6), we find that the full posterior density for $\vec{\alpha}$ is given by

$$p(\vec{\alpha} \mid \{\vec{m}\}) \propto p(\vec{\alpha}) \prod_i \int \mathrm{d}\mu_i \; p(\mu_i, E(\mu_i; \vec{\alpha}) \mid \vec{m}_i) \; , \tag{1.12}$$

where we have defined the function

$$p(\mu_i, E_i | \, \vec{m}_i) \equiv \frac{1}{Z_i} \int \mathrm{d}\vec{\Theta}_i \, p\left(\vec{m}_i \mid \mu_i, \vec{\Theta}_i, E_i\right) p\left(\mu_i, \vec{\Theta}_i\right) \; , \tag{1.13}$$

which is equivalent to the posterior probability density of finding a single star at distance $\mu_i$ and reddening $E_i$, where the prior on reddening is flat. Here, $Z_i$ is a normalizing constant. Effectively, it is the Bayesian evidence for star $i$, a measure of how likely the star is to be generated by the model. A higher evidence indicates that the data is more consistent with the model, while a low value for

$Z_i$ indicates that the model does not well describe the object $i$. Our strategy for sampling from a posterior of the form given by Eq. (1.12) is to pre-compute Eq. (1.13) for each star by Markov-Chain Monte Carlo (MCMC) sampling, and then to sample from $p(\vec{\alpha} \mid \{\vec{m}\})$. This approach has two advantages. First, it factorizes the full problem into a series of smaller problems of lower dimension, potentially speeding up the computation. The second advantage of this two-step approach is that it allows outlier rejection on the basis of the Bayesian evidence for each star before proceeding to the second step. Point sources which do not fit the chosen stellar model (e.g., blue stragglers, white dwarfs and galaxies mistakenly classified as stars) can be filtered out by imposing a cut on the evidence $Z_i$ (See § 1.5.2). More principled approaches to reducing the influence of outliers exist (e.g., Hogg *et al.* 2010), though in the context of our problem they are significantly more computationally expensive to implement.

A more general limitation to the approach taken here is that it does not allow the simultaneous fitting of parameters describing the stars and the spatial variation in dust properties. One could imagine simultaneously constraining stellar types and distances, as well as the dust density and $R_V$ parameter throughout space. By fitting the dust properties in many voxels simultaneously, one would be able to place priors on the density power spectrum of the dust, and to infer $R_V$ as a function of position in the Galaxy. By fitting dust properties throughout the entire volume of the Galaxy simultaneously, one could even attempt to constrain global parameters, such as the dust scale height and scale length. This would represent a hierarchical approach to the problem of creating a 3D dust map (See, for example, Kruschke 2010, for an introduction to hierarchical Bayesian models). At the highest level in the hierarchy, one has global parameters, which describe the overall

dust distribution and density power spectrum. One level below in the hierarchy, one would have parameters describing the dust properties in each voxel in the Galaxy. At the lowest level, one could have the type and distance for each star. Such a hierarchical approach is appealing because it takes into account spatial correlations in dust properties, and because it directly fits the global structure of the Galaxy's dust component. However, this hierarchical approach potentially requires much greater computational power than the approach I take in this thesis, as it does not allow one to process each star individually and treat each line of sight separately, greatly increasing the dimensionality of parameter space. This thesis therefore confines itself to fitting each star independently, and then combining the information from each star along any given line of sight to determine the reddening profile as a function of distance.

## 1.2 Individual Stars

Now that we have factorized the problem of determining the line-of-sight reddening profile into one of determining $p\left(\mu_i, E_i, \vec{\Theta}_i \mid \vec{m}_i\right)$ for each star, we need to determine the individual stellar likelihoods and priors. In the following, we will drop the subscript $i$, as it is assumed that we are dealing with one star.

Using Bayes' Rule,

$$p\left(\mu, E, \vec{\Theta} \mid \vec{m}\right) \propto p\left(\vec{m} \mid \mu, E, \vec{\Theta}\right) p\left(\mu, E, \vec{\Theta}\right) \ . \tag{1.14}$$

The likelihood, $p\left(\vec{m} \mid \mu, E, \vec{\Theta}\right)$, is the probability density of a star having apparent magnitudes $\vec{m}$,

given a distance, reddening and stellar type. The likelihood is discussed directly below, in § 1.2.1. The priors, $p\left(\mu, E, \vec{\Theta}\right)$, which are dependent on the distribution of stars of different types throughout the Galaxy, are discussed in § 1.2.2.

### 1.2.1 Stellar Likelihood

We adopt a simple stellar model, in which each star is described by two intrinsic parameters – its absolute magnitude, $M_r$, in the PS1 $r_{\rm P1}$ band and its metallicity, [Fe/H]. In terms of our previous notation, $\vec{\Theta} = (M_r, [\mathrm{Fe/H}])$. Given a set of stellar templates, $\vec{M}(M_r, [\mathrm{Fe/H}])$, which map intrinsic stellar type to a set of absolute magnitudes, one obtains theoretical apparent magnitudes

$$\vec{m}_{\rm mod} = \vec{M}(M_r, [\mathrm{Fe/H}]) + \vec{A}(E, R_V) + \mu\,. \tag{1.15}$$

The likelihood is thus dependent on our model of intrinsic stellar colors, $\vec{M}(M_r, [\mathrm{Fe/H}])$, which must be tailored to the specific photometric survey data that one uses. I discuss stellar models tailored to Pan-STARRS 1 and 2MASS photometry in § 2.3.

For the PS1 passbands, we adopt an extinction vector, $\vec{A}(E, R_V)$, that follows the Fitzpatrick (1999) reddening law with $R_V = 3.1$, adapted to the $grizy_{\rm P1}$ filter set by Schlafly & Finkbeiner (2011, see Table 6). In the 2MASS passbands, we adopt the reddening coefficients $R_J = 0.786$, $R_H = 0.508$ and $R_{Ks} = 0.320$, calculated by Yuan *et al.* (2013) for a 7000 K source spectrum at $\mathrm{E}(B-V) = 0.4$ mag, using the Cardelli *et al.* (1989) reddening law and assuming $R_V = 3.1$.

The likelihood of observing apparent magnitudes $\vec{m}$ with Gaussian uncertainties $\vec{\sigma}$ is then given

by

$$p(\vec{m} \,|\, \mu, \mathcal{M}_r, [\text{Fe/H}], E) = \mathcal{N}(\vec{m} \,|\, \vec{m}_{\text{mod}}, \vec{\sigma}) \ , \tag{1.16}$$

with $\vec{m}_{\text{mod}}$ given by Eq. (1.15). In this work, I use the notation $\mathcal{N}(\vec{x} \,|\, \vec{\mu}, \Sigma)$ to denote the probability density of a multivariate normal with mean $\vec{\mu}$ and covariance $\Sigma$, evaluated at $\vec{x}$. If the covariance matrix is diagonal, I instead write $\mathcal{N}(\vec{x} \,|\, \vec{\mu}, \vec{\sigma})$, where the covariance is taken to be $\Sigma = \text{diag}(\vec{\sigma})$.

### 1.2.2 Stellar Priors

I now present the priors that we place on the intrinsic (i.e., luminosity and metallicity) and extrinsic (i.e., distance and reddening) parameters describing each star. I factorize the priors as follows:

$$p(\mu, \mathcal{M}_r, [\text{Fe/H}]) = p(\mu)\, p([\text{Fe/H}] \,|\, \mu)\, p(\mathcal{M}_r) \ . \tag{1.17}$$

The luminosity fuction, $p(\mathcal{M}_r)$, is therefore taken to be universal throughout the Galaxy, while the distribution of stellar metallicities depends on position in the Galaxy, which for one sightline reduces to distance modulus, $\mu$. I describe the distance prior in § 1.2.2.a, the metallicity prior in § 1.2.2.b and the luminosity prior in § 1.2.2.c.

#### 1.2.2.a Stellar Distance Prior

For a given line of sight, the prior probability of finding a star in a small range d$\mu$ in distance modulus is proportional to the number of stars per unit distance modulus per unit solid angle in the

direction of the pixel:

$$p(\mu) \propto \frac{\mathrm{d}N}{\mathrm{d}\mu \mathrm{d}\Omega} = \frac{\mathrm{d}N}{\mathrm{d}r \mathrm{d}\Omega} \frac{\mathrm{d}r}{\mathrm{d}\mu} = n(\mu)\, r^2 \frac{\mathrm{d}r}{\mathrm{d}\mu} \propto 10^{3\mu/5}\, n(\mu) \ . \tag{1.18}$$

Here, $r$ denotes physical distance from the Sun, and $n(\mu)$ is the stellar number density at distance modulus $\mu$ along the chosen line of sight. The distance prior is thus controlled by the line-of-sight number density of stars, as well as a volume factor, $10^{3\mu/5}$, which grows with distance. This latter term takes into account that the volume represented by a beam of constant, small width in distance modulus grows with distance, and should be familiar from the earlier discussion, in § 0.1, of von Struve and Kapteyn's argument about the distribution of stellar apparent magnitudes. For a typical line of sight, the stellar distance prior is driven upwards by the volume factor at small distances, while farther out it is suppressed by the decline in density in the outer reaches of the Galaxy. For constant density, $n(\mu)$, Eq. (1.18) simply reduces to the Euclidean counts equation.

The distance prior thus requires us to calculate the stellar number density at arbitrary locations in the Galaxy. We employ the three-component Galactic model developed in Jurić *et al.* (2008), which comprises a thin disk, a thick disk and an oblate halo. In cylindrical coordinates centered on the Galactic center, and with the Galactic plane defining $Z = 0$, each disk component has number density of the form

$$n_i(R, Z) = n_{0,i}\, e^{-\left(R/R_{0,i} + |Z|/Z_{0,i}\right)} \ , \tag{1.19}$$

where $R_{o,\,i}$ and $Z_{o,\,i}$ are the scale radius and height respectively, of each disk component, and $n_{o,i}$ is the stellar number density of each component at the Galactic center. In the Solar neighborhood,

$$n_i(R_\odot,\, Z_\odot) = n_{o,i}\, e^{-\left(R_\odot/R_{o,i} + |Z_\odot|/Z_{o,i}\right)}\,, \tag{1.20}$$

where $R_\odot$ and $Z_\odot$ are the Galactocentric Solar radius and height in cylindrical coordinates, respectively. We can thus write the number density of each disk component in terms of locally defined quantities, which are more readily measurable than quantities defined at the Galactic center:

$$n_i(R, Z) = n_i(R_\odot,\, Z_\odot)\; e^{-\left[(R-R_\odot)/R_{o,i} + (|Z| - |Z_\odot|)/Z_{o,i}\right]}\,. \tag{1.21}$$

From this point onwards, we will denote $n_{\rm thin}(R_\odot,\, Z_\odot)$ as $n_\odot$, and write

$$n_{\rm thick}(R_\odot,\, Z_\odot) \equiv f_{\rm thick}\, n_\odot\,. \tag{1.22}$$

The halo is assumed to have stellar number density

$$n_{\rm halo}(R, Z) = n_\odot f_h \left(\frac{R_{\rm eff}}{R_\odot}\right)^{-\eta}\,, \tag{1.23}$$

with

$$R_{\rm eff} \equiv \sqrt{R^2 + (Z/q_h)^2 + R_\epsilon^2}\,. \tag{1.24}$$

Table 1.1: Stellar Number Density Parameters

| Thin Disk | | Thick Disk | | Halo | |
|---|---|---|---|---|---|
| $R_{\rm thin}$ | 2600 pc | $R_{\rm thick}$ | 3600 pc | $R_{\rm br}$ | 27.8 kpc$^{\dagger}$ |
| $Z_{\rm thin}$ | 300 pc | $Z_{\rm thick}$ | 900 pc | $q_h$ | 0.70$^{\dagger}$ |
| | | $f_{\rm thick}$ | 0.12 | $f_h$ | 0.0006$^{\star}$ |
| | | | | $\eta_{\rm inner}$ | 2.62$^{\dagger}$ |
| | | | | $\eta_{\rm outer}$ | 3.80$^{\dagger}$ |

$^{\dagger}$ Values from Sesar *et al.* (2011).
$^{\star}$ Chosen to match Robin *et al.* (2003).
All other values adopted from Jurić *et al.* (2008).

Here, $q_h$ controls the oblateness of the halo and $\eta$ controls the steepness of the power law. Following Sesar *et al.* (2011), the power law breaks at $R_{\rm eff} = R_{\rm br}$, becoming steeper. We therefore define $\eta_{\rm inner}$ and $\eta_{\rm outer}$, corresponding to the halo steepness inside and outside of the break. We also introduce a distance scale, $R_\epsilon$, over which the inner region of the halo is smoothed, in order to remove the singularity at the Galactic Center. We choose $R_\epsilon$ to be 500 pc; at this scale, it has a negligible effect on the halo density in the regions which Jurić *et al.* (2008) studied, but it prevents the halo from dominating over the disk at the Galactic Center and is the same scale adopted by Robin *et al.* (2003).

I employ the parameters given in Table 10 of Jurić *et al.* (2008) and Sesar *et al.* (2011). These are listed in Table 1.1. I adopt, however, a less dense halo prior than Jurić *et al.* (2008), reducing the local halo density (relative to the local thin-disk stellar density) from $f_h = 0.0051$ to $f_h = 0.0006$, a similar value to that used by the Besançon model (Robin *et al.* 2003). Throughout, I use $R_\odot = 8$ kpc and $Z_\odot = 25$ pc.

The shape of the distance prior for a line of sight centered on $\ell = 90^\circ$ and $b = 10^\circ$ is shown in Fig. 1.1. Of course, the shape of the distance prior depends on the angle on the sky. At high Galactic

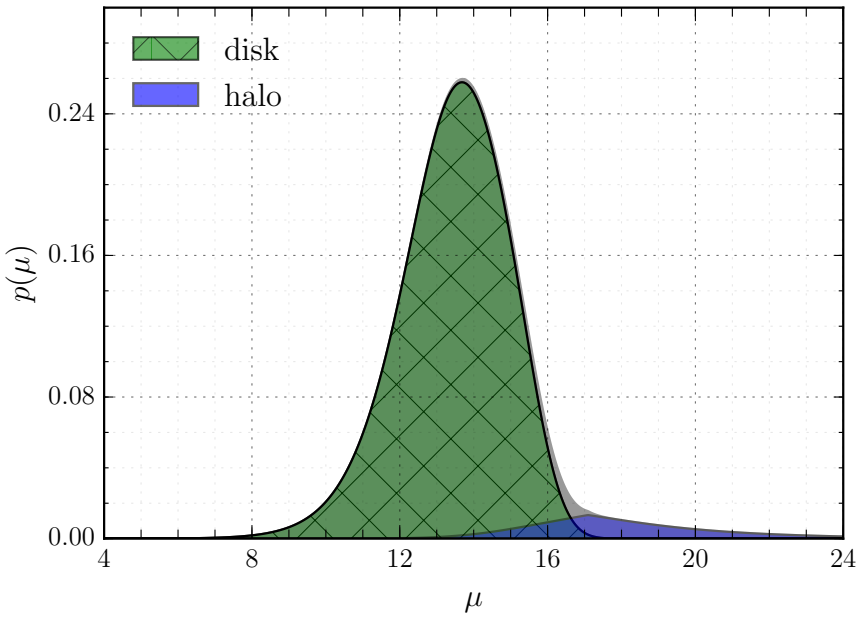


Figure 1.1: The distance prior for $(\ell,\ b) = (90°,\ 10°)$. The contributions of the disk and halo are shown individually in green and purple, respectively, while the total prior is given by the gray contour. The break in the contribution from the halo is due to the use of a broken power law for the number density of stars in this component. The shape of the distance prior varies across the sky.

latitudes, the halo is relatively stronger, while at low Galactic latitudes, in the plane of the Milky Way, the stellar disk terms dominate.

#### 1.2.2.b Stellar Metallicity Prior

I adopt the model of Galactic metallicity developed in Ivezić *et al.* (2008a) and Bond *et al.* (2010), assigning separate metallicity distributions to the disk and halo. The metallicity distribution of the disk varies with height above the Galactic plane, and is thus dependent on line-of-sight distance.

The metallicity prior takes the form

$$p([\mathrm{Fe/H}] \mid \mu) = p([\mathrm{Fe/H}] \mid \mu,\ \mathrm{disk})\, p(\mathrm{disk} \mid \mu) + p([\mathrm{Fe/H}] \mid \mathrm{halo})\, p(\mathrm{halo} \mid \mu)\ . \tag{1.25}$$

The membership probabilities are simply

$$p(\mathrm{disk} \mid \mu) = \frac{n_{\mathrm{thin}}(\mu) + n_{\mathrm{thick}}(\mu)}{n_{\mathrm{thin}}(\mu) + n_{\mathrm{thick}}(\mu) + n_{\mathrm{halo}}(\mu)}\ , \tag{1.26}$$

$$p(\mathrm{halo} \mid \mu) = 1 - p(\mathrm{disk} \mid \mu)\ , \tag{1.27}$$

which can be calculated on the basis of the preceding discussion (§ 1.2.2.a).

For the disk, stellar metallicity is distributed as a sum of Gaussians. The mean of each Gaussian varies with height above the Galactic plane, so that the prior is best written in terms of cylindrical coordinates:

$$p([\mathrm{Fe/H}] \mid Z,\ \mathrm{disk}) = c\,\mathcal{N}([\mathrm{Fe/H}] \mid a(Z), \sigma_D) + (1-c)\,\mathcal{N}([\mathrm{Fe/H}] \mid a(Z)+\Delta a, \sigma_D)\ , \tag{1.28}$$

where

$$a(Z) = a_D + \Delta_\mu e^{-|Z|/H_\mu}\ . \tag{1.29}$$

The parameters $a_D$, controlling the central disk metallicity, and $\Delta_\mu$ and $H_\mu$, describing the vertical metallicity gradient in the disk, are defined in Table 1.2. We assume the halo metallicity to be spa-

Table 1.2: Metallicity Parameters

| Disk | | Halo | |
|---|---|---|---|
| $a_D$ | $-0.89$ | $a_H$ | $-1.46$ |
| $\sigma_D$ | 0.20 | $\sigma_H$ | 0.30 |
| $c$ | 0.63 | | |
| $\Delta a$ | 0.14 | | |
| $\Delta_\mu$ | 0.55 | | |
| $H_\mu$ | 0.5 kpc | | |

tially invariant, and distributed as

$$p([\mathrm{Fe}/\mathrm{H}] \mid \mathrm{halo}) = \mathcal{N}([\mathrm{Fe}/\mathrm{H}] \mid a_H, \sigma_H) \ . \tag{1.30}$$

The parameters, $a_H$ and $\sigma_H$, describing the halo metallicity, are given in Table 1.2. The metallicity prior is plotted in Fig. 1.2 as a function of height above the Galactic midplane in the Solar neighborhood.

### 1.2.2.c Stellar Luminosity Prior

I use the $r_{\mathrm{P1}}$-band absolute magnitude to parameterize the luminosity of each star. The joint prior on luminosity and distance is

$$p(\mu, \mathcal{M}_r) \propto \frac{\mathrm{d}N(\mu, \mathcal{M}_r)}{\mathrm{d}\mu \, \mathrm{d}\mathcal{M}_r} \ . \tag{1.31}$$

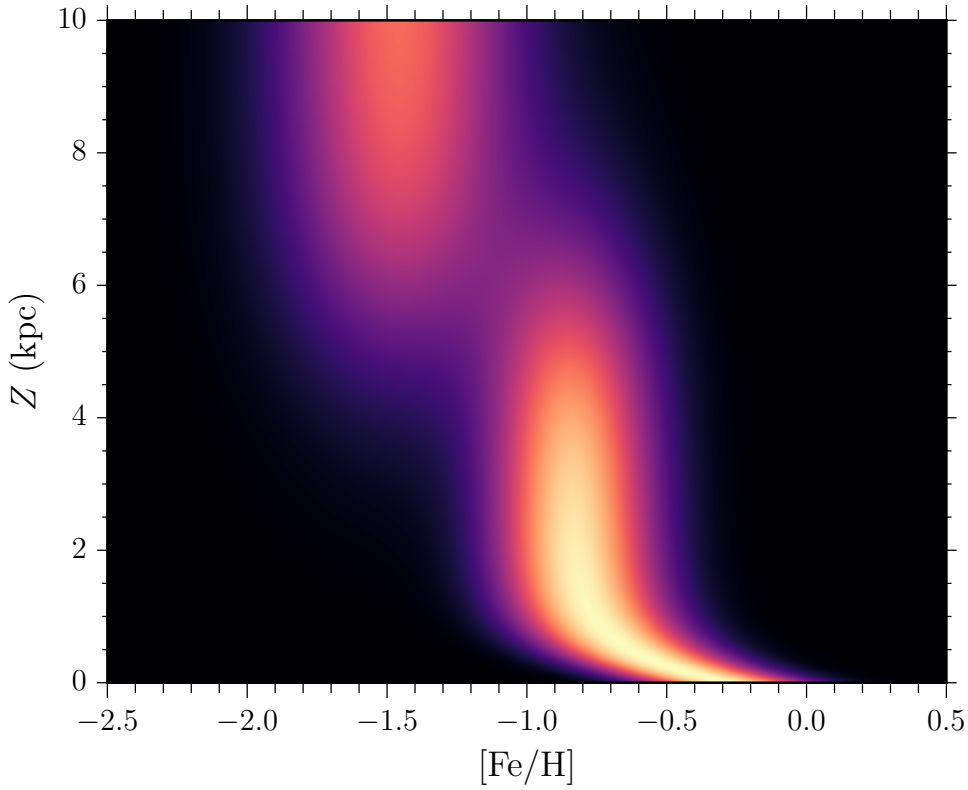


Figure 1.2: The metallicity prior, $p([\mathrm{Fe/H}] \mid Z)$, in the Solar neighborhood ($R = 8$ kpc). High above the plane of the Galaxy, where the halo dominates, the metallicity distribution has a constant mean and variance. In the plane, where the disk dominates, the mean decreases with scale height. Adapted from Fig. 9 of Ivezić *et al.* (2008a).

The luminosity function is assumed to be same in the halo and both disk components, and furthermore independent of position. The priors on distance and luminosity are then separable, so that

$$p(\mu,\, \mathcal{M}_r) = p(\mu)\, p(\mathcal{M}_r) \ , \tag{1.32}$$

with $p(\mathcal{M}_r) = \mathrm{LF}(\mathcal{M}_r) \propto \frac{\mathrm{d}N}{\mathrm{d}\mathcal{M}_r}$.

I adapt the PS1 luminosity functions provided by the Padova & Triese Stellar Evolution Code (Bressan *et al.* 2012, PARSEC), assuming a Chabrier (2001) log-normal initial mass function. I average over luminosity functions for populations with ages of $\tau = 7 \pm 2$ Gyr and metallicities $[\mathrm{Fe/H}] = -0.5 \pm 0.5$ dex. Denote the luminosity function for a population of age $\tau$ and metallicity $[\mathrm{Fe/H}]$ as $\mathrm{LF}(\mathcal{M}_r \,|\, \tau,\, [\mathrm{Fe/H}])$. The luminosity function I adopt is then

$$\mathrm{LF}(\mathcal{M}_r) \propto \int \mathrm{d}\tau \int \mathrm{d}[\mathrm{Fe/H}] \;\; \mathrm{LF}(\mathcal{M}_r \,|\, \tau,\, [\mathrm{Fe/H}]) \, \exp\left[ -\frac{(\tau - \tau_0)^2}{2\sigma_\tau^2} - \frac{([\mathrm{Fe/H}] - [\mathrm{Fe/H}]_0)^2}{2\sigma^2_{[\mathrm{Fe/H}]}} \right] \ , \tag{1.33}$$

with $\tau_0 = 7$ Gyr, $\sigma_\tau = 2$ Gyr, $[\mathrm{Fe/H}]_0 = -0.5$ dex and $\sigma_{[\mathrm{Fe/H}]} = 0.5$ dex. In principle, it is possible to make the luminosity function depend on metallicity, by not averaging over $[\mathrm{Fe/H}]$ in Eq. (1.33). For simplicity, I assume here that the luminosity function is universal.

#### 1.2.2.d Stellar Reddening

As explained in § 1.1, the manner in which we have factorized the line-of-sight reddening problem requires us to place a flat prior on the color excess, $E$, for each star. The priors on the reddening profile are imposed on the parameters which control the line-of-sight reddening, rather than on

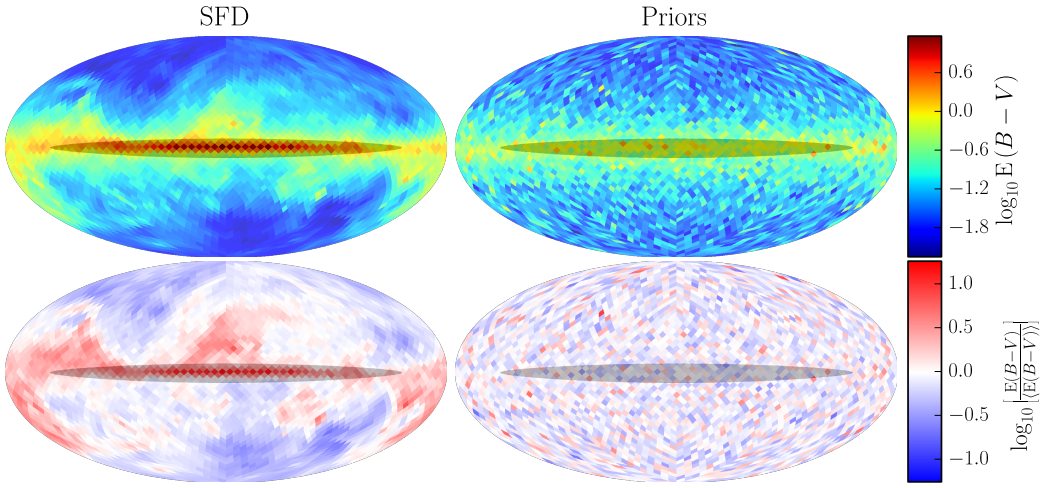


Figure 1.3: The SFD dust map, compared to a random draw from the priors on the 3D dust reddening distribution, used in the construction of our map. The top two panels, from left to right, show the SFD reddening and the 2D reddening map that results from a draw from the priors, both on a log scale. The bottom two panels show the same maps, after dividing out the mean projected reddening in the priors. The priors are limited so that the mean expected reddening in any given distance bin does not exceed a pre-defined amount. This is done in order to avoid inferring large amounts of reddening in the absence of data. Regions that are affected by this clipping are shaded in gray. The priors do not include spatial correlations, as can be seen by comparing the bottom two panels.

individual stellar reddenings. The line-of-sight reddening priors are discussed below, in § 1.3. For example, if one divides each sightline into $N$ distance bins and assigns a different dust density $\rho_i$ to each bin, then the reddening prior would take the form $p(\rho_1,\ \rho_2,\ \ldots,\ \rho_N)$.

## 1.3 3D Dust Priors

As laid out in § 1.1, the parameters describing the distribution of dust along a chosen sightline are denoted by $\vec{\alpha}$. As we saw in Eq. (1.6), it is necessary to choose a prior on $\vec{\alpha}$ – I describe this prior in what follows.

In this work, reddening is parameterized in each sigtline as a monotonically increasing, piecewise-

linear function in distance modulus. Dividing up the line of sight into bins of equal width in distance modulus, we infer the increase in reddening in each bin, so that

$$\vec{\alpha} = \{\Delta E_k \,|\, k = 1, 2, \ldots, N_{\text{bins}}\} \ , \tag{1.34}$$

where $k$ denotes the bin index, and $N_{\text{bins}}$ is the number of distance bins. We place a log-normal prior on the reddening in each bin:

$$\Delta E_k = e^{\epsilon_k} \ , \ \text{ where } \epsilon_k \sim \mathcal{N}(\bar{\epsilon}_k \, , \sigma_\epsilon) \ . \tag{1.35}$$

In each bin, we set $\bar{\epsilon}_k$ so that the mean reddening in each voxel matches what would be expected from the smooth disk component of Drimmel & Spergel (2001), up to a constant normalization that is the same for the entire map. In order to fully define the priors, there are therefore two global parameters that must be set:

1. $\mathrm{d}E(B\!-\!V)/\mathrm{d}s\big|_{s=0}$, the local normalization of the dust reddening per unit distance, and
2. $\sigma_\epsilon$, the width of the log-normal prior on dust column density in each voxel.

We fit these two numbers so that our priors, in projection, produce two-dimensional dust maps with the same overall normalization and standard deviation as the SFD dust map. We find that $\sigma_\epsilon = 1.4$ and a local reddening per unit distance of $\mathrm{d}E(B\!-\!V)/\mathrm{d}s = 0.2$ mag kpc$^{-1}$ roughly matches the mean and variance of the SFD dust map over large angular scales.

Fig. 1.3 shows a random realization of these 3D dust priors, next to the SFD dust map. In each bin, we limit $\bar{\epsilon}$ to the range $-12 \leq \bar{\epsilon} \leq -4$. On the lower end, the limit helps our fit to converge

by preventing the prior from becoming too stringent. On the upper end, the limit prevents the fit from inferring large amounts of dust in the absence of data. Regions where $\bar{\epsilon}$ has been limited to $-4$ are shaded in Fig. 1.3. These priors do not impose spatial correlations across lines of sight, and thus in the absence of data, produce cloud-free maps. The detailed cloud structures that emerge from this 3D dust modeling therefore derive entirely from the data, rather than from the priors.

It is worth noting that the above 3D dust priors diverge from what one should expect for the real distribution of dust in a number of ways. In order to render the problem of fitting the 3D distribution of dust tractable, we fit the dust column along each sightline separately. We know, however, that in real life, dust density has spatial correlations. Moreover, there is nothing special about the Sun's place in the Galaxy, but our dust map voxelizes the sky into pencil beams centered on the Solar System. This of course makes practical sense, since angles are much easier to measure than distances in astronomy, but it is again an unreal feature of the chosen voxelization. A more realistic model would treat the dust density as a continuous field, or voxelize the Galaxy in a way that treats the angular and radial directions equally, and would impose correlations between dust density in nearby points in space (See, e.g., Lallement *et al.* 2014; Sale & Magorrian 2014). This entails significantly more algorithmic and computational complexity than the method used here, and I defer such work to the future. Within the constraints of the present setup – independent sightlines with pencil-beam-like voxels – the priors attempt to reasonably trace the properties of the Galaxy, including the mean dust density in each voxel and the overall variance in dust column across the sky.

## 1.4 Additions to the Basic Model

### 1.4.1 Survey Selection Function

The stellar distance prior developed in § 1.2.2.a only asks how many stars are in a thin shell at each distance. However, for a magnitude-limited survey, we would like instead to know the number of observable stars at a given distance. We should assign zero prior probability to the possibility of a star being observed which our instrument cannot detect. The fact that a star has been observed by a given instrument therefore tells us something about its stellar type, distance and extinction. Using the notation from Sale (2012), define the vector $\vec{S}$ for each star, where $S_i$ is true if a star has been observed in passband $i$, and false if the star is not detected in that passband. The PS1 dataset used in this thesis is not based on forced photometry, so there is a separate probability of a source being detected in each passband. If forced photometry were conducted, there would be one single probability $p(S)$, equal to the probability of detecting the source in at least one of the passbands. Including this information in the single-star posterior, Eq. (1.13), we get

$$p\left(\mu, E, \vec{\Theta} \,|\, m_{\text{obs}}, \vec{S}\right) \propto p\left(m_{\text{obs}} |\, \mu, E, \vec{\Theta}, \vec{S}\right) p\left(\mu, E, \vec{\Theta} \,|\, \vec{S}\right) \ . \tag{1.36}$$

But the prior is now just

$$p\left(\mu, E, \vec{\Theta} \,|\, \vec{S}\right) \propto p\left(\vec{S} \,|\, \mu, E, \vec{\Theta}\right) p\left(\mu, E, \vec{\Theta}\right) \ , \tag{1.37}$$

so in full,

$$p\left(\mu, E, \vec{\Theta} \,|\, m_{\rm obs}, \vec{S}\right) \propto p\left(m_{\rm obs}|\, \mu, E, \vec{\Theta}, \vec{S}\right) p\left(\mu, E, \vec{\Theta}\right) p\left(\vec{S} \,|\, \mu, E, \vec{\Theta}\right) \,. \tag{1.38}$$

The first term is simply the likelihood we found earlier, since the knowledge that the star has been detected has no effect on the apparent magnitudes the model predicts, assuming the stellar type, distance and reddening are known. That is to say,

$$\vec{m}_{\rm mod} = \vec{M}_{\rm mod}\left(\vec{\Theta}\right) + \vec{A}(E) + \mu \,, \tag{1.39}$$

and

$$p\left(m_{\rm obs}|\, \mu, E, \vec{\Theta}, \vec{S}\right) = \mathcal{N}(m_{\rm obs}|\, \vec{m}_{\rm mod}, \vec{\sigma}) \,. \tag{1.40}$$

The only element of the calculation which changes when we take into account Malmquist bias is therefore the prior, which picks up an extra factor of

$$p\left(\vec{S} \,|\, \mu, E, \vec{\Theta}\right) = p\left(\vec{S} \,|\, \vec{m}_{\rm mod}\right) = \prod_i p\left(S_i \,|\, m_{{\rm mod},\, i}\right) \,. \tag{1.41}$$

This is the survey selection function used in this work. The precise form of this function for each passband is derived in § 2.4.

If forced photometry were used instead, then we would have a single detection parameter $S$,

denoting that the source was detected in at least one passband, and the survey selection function would be

$$p\left(S = \text{true} \mid \mu, E, \vec{\Theta}\right) = p(S \mid \vec{m}_{\text{mod}}) = 1 - \prod_i p\left(S_i = \text{false} \mid m_{\text{mod},\,i}\right) \tag{1.42}$$

in place of the expression in Eq. (1.41).

### 1.4.2 Scatter in Line-of-Sight Reddening Profile

A basic assumption of our model, as described in § 1.1, is that within a given angular pixel, the dust density varies only with distance, and not with angle. If the pixels are sufficiently small, this is a good assumption. We are limited, however, in how small we can make each pixel by the need to include enough stars in each pixel to probe the dust density at a range of distances. Increasing the angular resolution of the map decreases the number of stars in each pixel, effectively decreasing the distance resolution of the map. We have found that we obtain best results for pixels containing a few hundred stars, and we vary the resolution of our pixels across the sky to obtain approximately the same number of stars in each pixel (See Fig. 2.1).

Note that varying the pixel size across the sky in this way technically violates the principles of Bayesian inference. From a forward-modeling point of view, the distribution of dust influences the number of stars that are observed in any given region of the sky. Sale (2015), for example, provides an excellent discussion of how a catalog of stars observed in a survey can be described as a Poisson point process whose rate is determined by the distribution of stars in the Galaxy, the three-dimensional

distribution of dust, and the survey selection function. Yet we are using the number of stars observed in each part of the sky to determine how to pixelize the sky. Our pixelization is therefore set, in part, by an observable (the density of stars across the sky) that is a consequence of the model. Nevertheless, as we are treating each pixel independently, and we would like to keep pixels as small as possible without reducing the number of stars per pixel below a few hundred, this rules violation is difficult to avoid. We expect the impact of this violation to be small in most regions of the sky. In regions with large sub-pixel variation in dust reddening, however, our map may be biased towards lower reddenings, as we preferentially detect stars in regions of the pixel with lower reddening.

The typical resolution of the map is $6.8' \times 6.8'$, corresponding to an `nside` $= 512$ HEALPix pixelization (Gorski *et al.* 2005). At this resolution, there can still be significant power in the dust density spectrum below the pixel scale. This can pose problems for our method, especially in the vicinity of dense clouds and filamentary structures, where the sub-pixel angular variation is largest. In order to deal with sub-pixel angular variation in the dust density, we relax our assumption that all stars lie along the same dust column by allowing each star to deviate from the local "average" dust column by a small amount. The reddening of star $i$ is parameterized as

$$E_i = (1 + \delta_i)\, E(\mu_i; \vec{\alpha}) \ , \tag{1.43}$$

where $\delta_i$ is the fractional offset of the star from the local dust column, $E(\mu_i; \vec{\alpha})$.

In effect, our model is therefore that within each HEALPix pixel, the reddening is a white noise process, with a mean that increases piecewise linearly with distance. Each star samples this white

noise process at a particular distance and angular position within the pixel. The parameter $\delta_i$ is then understood as the fractional residual (from the mean reddening in the pixel at the given distance) of the reddening column at the angular location and distance of star $i$.

We put a Gaussian prior on $\delta_i$, with zero mean and standard deviation dependent to the scale of the pixel (allowing more variation in larger pixels) and the local dust column (allowing greater fractional variation in regions of greater reddening). In detail,

$$p(\delta_i \,|\, \mu_i,\, \vec{\alpha}) = \mathcal{N}(\delta_i \,|\, 0,\, \sigma_\delta) \ , \tag{1.44}$$

with

$$\sigma_\delta = a\, E(\mu_i; \vec{\alpha}) + b \, . \tag{1.45}$$

Here, $a$ and $b$ are parameters that we set in order to match the variation we see at the given pixel angular scale in the Planck radiance-based two-dimensional dust map. We compute the RMS scatter within HEALPix pixels of difference scales, finding that the scatter is well described by setting the coefficients $a$ and $b$ to

$$\log_{10} a = 0.88\, \log_{10}\left(\frac{\varphi}{1'}\right) - 2.96 \, , \tag{1.46}$$

$$\log_{10} b = 0.58\, \log_{10}\left(\frac{\varphi}{1'}\right) - 1.88 \, , \tag{1.47}$$

where $\varphi$ is the angular pixel scale, defined as the square-root of the pixel solid angle.

We have found through trial and error that it is preferable to impose a minimum scatter of $\sim$ 10% on the in-pixel dust column. Additionally, if we allow $\delta_i$ to approach unity, we clearly risk the possibility of scattering a star to negative dust column. We therefore never allow $\sigma_\delta > 0.25$.

Although the complication introduced in this section adds an additional parameter, $\delta_i$, for each star, it can be achieved with minimal additional computational resources. We are introducing a Gaussian scatter in the reddening of each star from the "average" reddening in the pixel, and an appropriate Gaussian smoothing of the individual stellar probability density surfaces, $p(\mu_i,\ E_i \mid \vec{m}_i)$, achieves this effect.

To see exactly how this works out mathematically, let us begin with the full posterior density on line-of-sight reddening given our stellar photometry (See Eq. (1.6)), and include a deviation, $\delta_i$, for each star $i$,

$$p(\vec{\alpha} \mid \{\vec{m}\}) \propto p(\vec{\alpha}) \prod_i \int \mathrm{d}\mu_i \, \mathrm{d}\vec{\Theta}_i \, \mathrm{d}\delta_i \; p\Big(\vec{m}_i \mid \mu_i, \vec{\Theta}_i, \vec{\alpha}, \delta_i\Big)\, p\Big(\mu_i, \vec{\Theta}_i, \delta_i \mid \vec{\alpha}\Big) \ . \tag{1.48}$$

Here, $\vec{\Theta}_i$ is the type of star $i$. Taking just the integrand, and ignoring the subscript $i$ for the moment,

$$I \equiv p\Big(\vec{m} \mid \mu, \vec{\Theta}, \vec{\alpha}, \delta\Big)\, p\Big(\mu, \vec{\Theta}, \delta \mid \vec{\alpha}\Big) \tag{1.49}$$

$$= p\Big(\vec{m} \mid \mu, \vec{\Theta}, \vec{\alpha}, \delta\Big)\, p\Big(\mu, \vec{\Theta} \mid \vec{\alpha}\Big)\, p\Big(\delta \mid \mu, \vec{\Theta}, \vec{\alpha}\Big) \ . \tag{1.50}$$

As before, we assume that

$$p\left(\mu, \vec{\Theta} \,|\, \vec{\alpha}\right) = p\left(\mu, \vec{\Theta}\right) \ , \tag{1.51}$$

with the only complication being the survey completeness limit, which has no impact on the modification being discussed here. We also assume that

$$p\left(\delta \,|\, \mu, \vec{\Theta}, \vec{\alpha}\right) = p(\delta \,|\, \mu, \vec{\alpha}) \ , \tag{1.52}$$

since $\delta$ is a property of the sub-pixel variation in dust density, and should be unrelated to stellar type. Then,

$$I = p\left(\vec{m} \,|\, \mu, \vec{\Theta}, \vec{\alpha}, \delta\right) p\left(\mu, \vec{\Theta}\right) p(\delta \,|\, \mu, \vec{\alpha}) \ . \tag{1.53}$$

The likelihood term (the first term on the right-hand side), can be rewritten as

$$p\left(\vec{m} \,|\, \mu, \vec{\Theta}, E(\mu; \vec{\alpha}, \delta)\right) \ , \tag{1.54}$$

since the modeled apparent magnitude is simply determined by the stellar distance, type and reddening, and the individual stellar reddening is determined by the line-of-sight reddening profile, the stellar distance, and the fractional deviation of the stellar reddening from the local reddening.

By Bayes' Rule, the product

$$p\Big(\vec{m} \,|\, \mu, \vec{\Theta}, E(\mu; \vec{\alpha}, \delta)\Big)\, p\Big(\mu, \vec{\Theta}\Big) \tag{1.55}$$

is proportional to the posterior density on distance, reddening and stellar type for an individual star, in the presence of a flat prior on reddening. Thus,

$$I \propto p\Big(\mu, \vec{\Theta}, E \,|\, \vec{m}\Big)\, p(\delta \,|\, \mu, \vec{\alpha}) \ , \tag{1.56}$$

evaluated at $E = (1 + \delta)\, E(\mu; \vec{\alpha})$. After marginalizing over stellar type, $\Theta$, we are left with

$$\int \mathrm{d}\Theta\, I \propto p(\mu, E) = (1 + \delta)\, E(\mu; \vec{\alpha} \,|\, \vec{m})\, p(\delta \,|\, \mu, \vec{\alpha}) \ , \tag{1.57}$$

Recall that the prior on $\delta$ is a Gaussian centered on zero, with width determined by $E(\mu; \vec{\alpha})$. Then,

$$\int \mathrm{d}\Theta\, I \propto p(\mu, E = (1 + \delta)\, E(\mu; \vec{\alpha}) \ | \, \vec{m})\, p(\delta \,|\, E(\mu; \vec{\alpha})) \ , \tag{1.58}$$

Marginalizing over $\delta$ now leaves us with a smoothed version of the individual stellar posterior density in distance and reddening:

$$\int \mathrm{d}\Theta\, \mathrm{d}\delta\, I = \tilde{p}(\mu, E(\mu; \vec{\alpha}) \,|\, \vec{m}) \ , \tag{1.59}$$

where we have defined the "smoothed" individual stellar posterior probability density

$$\tilde{p}(\mu, E) = \int \mathrm{d}\delta \, p(\mu, (1+\delta)\, E \,|\, \vec{m})\, p(\delta \,|\, E) \ . \tag{1.60}$$

In Eq. (1.12), we therefore replace the individual stellar posterior densities with "smoothed" posterior densities:

$$p(\vec{\alpha} \,|\, \{\vec{m}\}) \propto p(\vec{\alpha}) \prod_i \int \mathrm{d}\mu_i \, \tilde{p}(\mu_i, E(\mu_i; \vec{\alpha}) \,|\, \vec{m}_i) \ . \tag{1.61}$$

Our method relies on calculating the individual stellar posterior probability densities for all stars along a line of sight first, before sampling from the line-of-sight reddening distribution, as described in detail in § 1.5. The above derivation shows that the addition of scatter in individual lines of sight, allowing stars to deviate from the line-of-sight reddening profile, can be accomplished by an intermediate step, in which the individual stellar posterior densities are smoothed in reddening, according to Eq. (1.60).

## 1.5 Sampling Strategy

### 1.5.1 Individual Stars

We use Markov Chain Monte Carlo (MCMC) sampling to explore the parameter space for individual stars. The sampling must be performed with great care, owing to two features of the distributions $p(\mu, E)$. First, the distributions are invariably highly elongated, and second they are often

multimodal. The elongation stems from the close alignment between the reddening vector and the stellar locus in the PS1 bands, as shown in Fig. 1.4. The multimodality has two causes. First, the reddening vector in general intersects the *gri* stellar locus in two locations, creating a degeneracy between blue and red main-sequence stars. Second, the PS1 bands do not distinguish dwarfs from giants, leading to the possibility that a star can be either a faraway red giant or a nearby red dwarf.

These degeneracies are easier to visualize if we consider only three passbands, as shown in Fig. 1.4. In this reduced space, stellar photometry is fully described by a single overall observed magnitude and two colors. If we observe a star at a given location in color-color space, we can then move backwards along the reddening vector until we intersect the stellar locus. One can then compare the observed apparent magnitude with the absolute magnitude of the stellar locus at the point of intersection. One thus obtains both a reddening and distance for the star. If there are multiple intersections, then the observed star could be of different intrinsic types, and thus have different reddening and distance combinations. The relative probability of each mode is in practice given by the space of stellar types lying close to the gray line, as well as the priors applied to the problem.

We perform an MCMC sampling of these surfaces using a custom `C++` implementation of the affine-invariant sampler introduced in Goodman & Weare (2010) and recently given in a python implementation by Foreman-Mackey *et al.* (2012). We employ both short-range "stretch" and long-range "replacement" moves (Goodman & Weare 2010). The long-range moves allow mixing between widely separated modes in parameter space, but are more computationally expensive than the short-range "stretch" steps. The replacement moves are closely related to the Normal Kernel Coupler of Warnes (2001). We have found that with the addition of long-range "replacement" steps, the

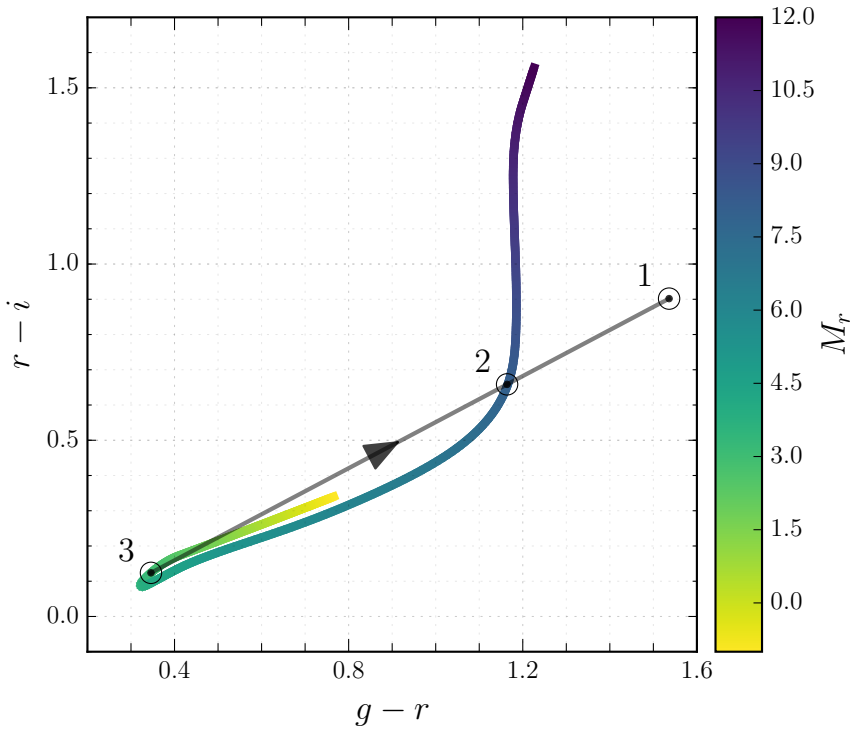


Figure 1.4: Sketch of how photometric parallax works, for illustrative purposes, adapted from Berry *et al.* (2012). A star is observed at location 1 in color-color space. Its de-reddened colors may lie along any point on the gray line, parallel to the reddening vector. The intersections of this line with the model stellar locus, labeled 2 and 3, represent the most likely intrinsic stellar types. The posterior density for the star will thus have two modes – one at larger distance and lesser reddening (2), and one at smaller distance and greater reddening (3). For simplicity, we assume Solar metallicity in this example. This is how one would make a distance and reddening determination by eye. The more rigorous probabilistic method laid out in § 1.1 takes into account photometric uncertainties, as well as priors on stellar type and Galactic structure.

affine-invariant sampler is capable of handling the multimodality of the problem, and that it is well suited to the strong degeneracies in parameter space. For each star, we sample from each stellar posterior density in four independent runs and screen for non-convergence by way of the Gelman-Rubin diagnostic (Gelman & Rubin 1992). The Gelman-Rubin diagnostic essentially verifies that the variance between the means of separate chains is small compared with the variance within the chains. If independent MCMC runs produce significantly different estimates of the parameter means, one or more of the runs must not have converged. Each run employs 20 samplers, with a mix of 80% stretch steps and 20% replacement steps, and 2000 steps per sampler. The first 1000 steps from each sampler are discarded as burn-in. Thus, excluding the burn-in phase, a total of 80000 samples are drawn for each star across the four chains, with the number of independent samples being lower due to correlations between successive samples. On four cores of a 2.67 GHz Intel Xeon X5650 with 12 MB of L3 cache, our run time per star is typically 0.15 seconds per run per core, or 0.8 CPU seconds for four independent runs.

### 1.5.2 Bayesian Evidence & Outlier Rejection

When an observed object does not match our stellar model, the inferences we draw on its distance, reddening and stellar type are unreliable. One means of quantifying the reliability of our inferences for an individual star is to compute the evidence

$$Z \equiv \int \mathrm{d}\mu \, \mathrm{d}E \, \mathrm{d}\vec{\Theta} \; p\left(\vec{m}, \vec{S} \,|\, \mu, E, \vec{\Theta}\right) \; p\left(\mu, E, \vec{\Theta}\right) \;, \tag{1.62}$$

which is the probability density of drawing the observed magnitudes $\vec{m}$ from the stellar model and observing the star in a photometric survey. A low evidence indicates that the observed point source is a member of a stellar population not included in our model (e.g., a young blue giant or an unresolved binary system with colors that do not match any stellar template), is not a star (e.g., a white dwarf or galaxy), that the errors in the photometry have been underestimated, or that the reddening vector is inaccurate. Here, our approach is similar to Berry *et al.* (2012), which identifies objects which do not fit the stellar model by a threshold $\chi^2$ statistic.

Note that as we do not include priors on the extinction to individual stars, but rather on the line-of-sight reddening profile, we do not strictly calculate the evidence. Instead, we calculate the evidence of a model with a prior on $E$ with wide support (i.e. a prior which allows $E$ to take on a wide range of values), such that the prior is nearly constant across all relevant reddennings:

$$p(E) \approx \begin{cases} a & 0 \leq E \lesssim E_0 \\ af(E) & E \gtrsim E_0 \end{cases}, \tag{1.63}$$

where $f(E)$ is some integrable function whose precise behavior is unimportant, $a$ is a normalizing constant, and $E_0$ is some large extinction. We thus effectively calculate the evidence $Z$ for a model of this form, up to a constant factor $a$, which is the same for every star. This allows for outlier rejection, based on comparisons between the evidence for different stars.

We employ a bounded harmonic mean estimate, which is obtained directly from the Markov chain produced in sampling the posterior density, and thus requires little additional computation

(Gelfand & Dey 1994; Robert & Wraith 2009). This method is presented in more detail in § A.1.

### 1.5.3 Line-of-Sight Sampling

We choose the HEALPix pixelization scheme (Gorski *et al.* 2005) as our method of dividing the sky into individual lines of sight. Once we have determined $p(\mu,\ E \mid \vec{m})$ for each star in a given HEALPix pixel and rejected stars which fall below the evidence cut, we can apply Eq. (1.12) to determine the posterior probability of the parameters $\vec{\alpha}$ describing the reddening profile. We parameterize the reddening profile as a piecewise-linear function in distance modulus, with $\alpha_i = \Delta E^{(i)}$ describing the rise in $r_{\mathrm{P1}}$-band reddening in distance segment $i$. We split up each line of sight into 30 distance segments of equal width in $\mu$, with the closest distance being at $\mu = 4$, corresponding to 63pc, and the furthest distance being at $\mu = 19$, corresponding to 63kpc. It must be cautioned that, in general, our method does not tightly constrain reddening at this latter distance, where PS1 observes very few stars.

We use a number of different types of step proposals to draw a representative sample of possible reddening profiles: We use the affine-invariant "stretch" and "replacement" proposals, Gaussian Metropolis-Hastings proposals, as well as an additional proposal type, which we term "swap proposals," tailored to the degeneracies inherent in our line-of-sight reddening parameterization. This last step proposal is laid out in § A.2. We sample from the posterior density given by Eq. (1.6), with the modifications described above, in § 1.4. We can thus produce a three-dimensional reddening map which includes the uncertainty in reddening as a function of distance.

## 1.6 Summary of Model

In summary, the model of each sightline contains the following elements:

- The increase in the "average" reddening in each distance bin: $\vec{\alpha} = \{\Delta E_k \mid k = 1, \ldots, n_{\text{bins}}\}$.
- The distance modulus, $\mu_i$, stellar type, $\Theta_i$ and fractional offset, $\delta_i$ from the "average" reddening of each star $i$.

The reddening of star $i$ is therefore determined both by $\vec{\alpha}$ and $\delta_i$. Together with the distance and type of the star, one can obtain model apparent magnitudes for the star, and thus a likelihood:

$$p\left(\vec{m}_i \mid \mu_i, \vec{\Theta}_i, \delta_i, \vec{\alpha}\right) . \tag{1.64}$$

We also have per-star priors on distance and stellar type, given by a smooth model of the distribution of stars throughout the Galaxy, and a prior on the offset of each star from the local reddening column:

$$p\left(\mu_i, \vec{\Theta}_i, \delta_i \mid \vec{\alpha}\right) = p\left(\mu_i, \vec{\Theta}_i\right) p(\delta_i \mid \mu_i, \vec{\alpha}) . \tag{1.65}$$

We finally have a log-normal prior on the increase in reddening in each distance bin along each sightline, $p(\vec{\alpha})$, whose mean is chosen to match a smooth model of the distribution of dust throughout the Galaxy.

The posterior on the line-of-sight reddening along one sightline is then given by

$$p(\vec{\alpha} \,|\, \{\vec{m}\}) \propto p(\vec{\alpha}) \prod_{i=1}^{n_{\mathrm{stars}}} \int \mathrm{d}\mu_i \, \mathrm{d}\vec{\Theta}_i \, \mathrm{d}\delta_i \; p\left(\vec{m}_i \,|\, \mu_i, \vec{\Theta}_i, \delta_i, \vec{\alpha}\right) p\left(\mu_i, \vec{\Theta}_i\right) p(\delta_i \,|\, \mu_i, \vec{\alpha}) \; . \tag{1.66}$$

In order to sample from this model, we first pre-compute the likelihood and prior terms for the individual stars, marginalizing over $\vec{\Theta}_i$ and $\delta_i$. We then sample in $\vec{\alpha}$, taking the required integral over $\mu_i$ in each step.

## 1.7 Extracting Additional Stellar Information from the 3D Map

In order to create the 3D dust map, we first probabilistically infer the distance and reddening to each star individually, with no information about the 3D structure of the dust. After creating the 3D dust map, however, we have a very strong constraint on how reddening should increase with distance, and this should impact our inferences about individual stellar distances and reddenings. In order to improve our stellar parameter inferences, we should replace our initial assumption about stellar reddening (a flat prior) with a new one that favors stellar reddenings close to the measured distance-reddening relation along the sightline. This can be done, in practice, by reweighting the probability density functions we initially calculated for each star. In this section, we therefore define a reweighting of the Markov Chain samples for the individual stars which takes into account the line-of-sight reddening.

Let us first consider the case in which we fix the line-of-sight reddening profile. In the formalism used here, that means that we fix the parameters $\vec{\alpha}$, expressing the line-of-sight reddening profile

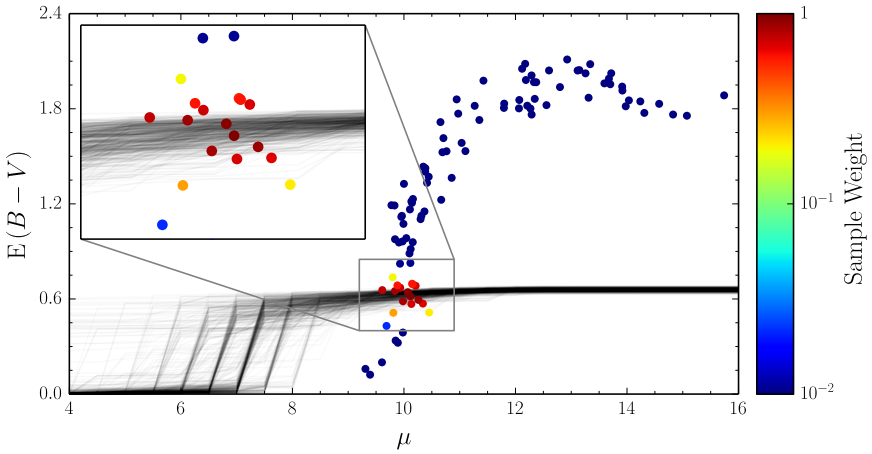


Figure 1.5: Reweighting Markov Chain samples for an individual star, based on the line-of-sight reddening profile. Each black line is a reddening profile drawn from the posterior on line-of-sight reddening. The dots are posterior samples of parameters (including distance and reddening) for one star viewed in isolation, i.e., not conditioned on the line-of-sight reddening. The samples are reweighted in order to condition them on the line-of-sight reddening, assigning greater weight to samples that are consistent with the reddening profile. Including information about the line-of-sight reddening can significantly reduce the uncertainties in stellar distance, reddening and type.

as $E(\mu; \vec{\alpha})$. The reddening of an individual star is then determined by the distance modulus of the star, $\mu$, as well as the fractional deviation, $\delta$, of the stellar reddening from the local dust column. As before, there are also parameters representing the stellar type, $\vec{\Theta}$. In this formulation, the posterior density of the stellar parameters, given its photometry $\vec{m}$ and the line-of-sight reddening profile, is determined by

$$p\left(\mu, \vec{\Theta}, \delta \,|\, \vec{m},\, \vec{\alpha}\right) \propto p\left(\vec{m} \,|\, \mu, \vec{\Theta}, \delta, \vec{\alpha}\right) p\left(\mu, \vec{\Theta}\right) p(\delta \,|\, \mu, \vec{\alpha}) \ . \tag{1.67}$$

We already have Markov chain samples in distance, reddening and stellar type for each star, for a model which does not take the line-of-sight reddening into account. We would like to apply weights

to these samples, so that they correspond to the model sketched out directly above. As shown in detail in § A.3, the correct reweighting of the stellar Markov chain samples, assuming a particular line-of-sight reddening profile $\vec{\alpha}$, is

$$w_k \propto \frac{\mathcal{N}(\delta_k \mid 0, \sigma_\delta)}{E(\mu_k; \vec{\alpha})}\,, \tag{1.68}$$

where $k$ indexes the sample, and $\delta_k$ is the fractional offset of the sample reddening, $E_k$, from the line-of-sight reddening, $E(\mu_k; \vec{\alpha})$, at distance $\mu_k$. The numerator in the above weight corresponds to a prior on the offset of the stellar reddening from the local dust column, while the denominator comes from the Jacobian transformation from reddening to fractional offset from the local reddening.

Reweighting each of the stellar parameter samples by the above factor, and normalizing the sum of the weights to unity, we obtain an inference for the stellar parameters, conditioned on a particular line-of-sight reddening profile, $E(\mu; \vec{\alpha})$. We marginalize over the line-of-sight reddening profile by repeating this procedure for each sampled value of $\vec{\alpha}$, summing the weight applied to each stellar sample.

It might be objected that since we infer $\vec{\alpha}$ using the photometry of all the stars in the given pixel, the samples we drew for $\vec{\alpha}$ in our initial processing are already dependent on the photometry for the star whose samples we are reweighting. Put more formally, the prior we use here when marginalizing over line-of-sight reddenings is the inference we obtained earlier, $p(\vec{\alpha} \mid \{\vec{m}\})$, which is conditional on all the photometry in the pixel, $\{\vec{m}\}$. We are using the photometry of a given star to infer the line-of-sight reddening, and then again to infer the stellar parameters, conditional on that line-of-sight

reddening.

This would be a problem if the photometry of any single star significantly affected the line-of-sight reddening inference. However, if photometry from a large number of stars informs the line-of-sight reddening, then no one star should have a significant impact on the inferred line-of-sight reddening profile. In a more formally correct formulation of the problem, we would first infer the line-of-sight reddening using all the stars in the pixel except the star whose parameters we wish to infer, and we would then infer the parameters for that star, conditional on the inferred line-of-sight reddening profile. As each pixel contains hundreds of stars, however, we expect our procedure to approximate this formally correct procedure closely.

Fig. 1.5 shows the result of reweighting the samples for one star. Depending on the line-of-sight reddening profile and the distribution of the unweighted stellar parameter samples, individual stellar inferences can be tightened dramatically by taking the line-of-sight reddening into account. Our knowledge of the parameters describing one star is therefore dependent not only on its photometry, but also on the photometry of its neighbors on the sky. Because neighboring stars lie along the same dust column, inferences for nearby stars are coupled through the requirement that the dust column increase with distance.

*For as soon as your reasoning begins to proclaim the nature of things revealed by your divine mind, away flee the mind's terrors, the walls of the world open out, I see actions going on throughout the whole void: before me appear the gods in their majesty, and their peaceful abodes, which no winds ever shake nor clouds besprinkle with rain, which no snow congealed by the bitter frost mars with its white fall, but the air ever cloudless encompasses them and laughs with its light spread wide abroad.*

Lucretius, *de rerum natura*, 3.14–22, to Epicurus

# 2

# Data

Now that we have developed a mathematical model for the distribution of stars and dust throughout the Milky Way, I describe how this model can be tailored to two specific datasets, produced by Pan-STARRS 1 (PS1) and the Two Micron All-Sky Survey (2MASS). PS1 has surveyed three-quarters of the sky in the optical and NIR, while 2MASS has surveyed the entire sky in the NIR. In § 2.1, I introduce these two projects, while

in § 2.2, I describe how the survey data is partitioned across the sky. In § 2.3, I describe empirical templates of stellar spectral energy distributions developed for PS1 and 2MASS, and in § 2.4 study the completeness of each photometric survey.

## 2.1 Photometric Surveys

### 2.1.1 Pan-STARRS 1

Pan-STARRS 1 (PS1) is a 1.8-meter optical and NIR telescope located on Mount Haleakala, Hawaii (Kaiser *et al.* 2010; Hodapp *et al.* 2004). The telescope is equipped with the GigaPixel Camera 1 (GPC1), consisting of an array of 60 CCD detectors, each 4800 pixels on a side (Tonry & Onaka 2009; Onaka *et al.* 2008). From May 2010 to April 2014, the majority of the observing time was dedicated to a multi-epoch $3\pi$ steradian survey of the sky north of $\delta = -30^\circ$ (Chambers in prep.). The $3\pi$ survey observes in five passbands $g_{\rm P1}$, $r_{\rm P1}$, $i_{\rm P1}$, $z_{\rm P1}$, and $y_{\rm P1}$, similar to the Sloan Digital Sky Survey (SDSS; York *et al.* 2000), with the most significant difference being the replacement of the Sloan $u$ band with a near-infrared band, $y_{\rm P1}$. The PS1 filter set spans 400–1000 nm (Stubbs *et al.* 2010). The images are processed by the Pan-STARRS 1 Image Processing Pipeline (IPP) (Magnier 2006), which performs automatic astrometry (Magnier *et al.* 2008) and photometry (Magnier 2007). The data is photometrically calibrated to better than 1% accuracy (Schlafly *et al.* 2012; Tonry *et al.* 2012). The $3\pi$ survey reaches typical single-exposure depths of 22 mags (AB) in $g_{\rm P1}$, 21.5 mags in $r_{\rm P1}$ and $i_{\rm P1}$, 20.8 mags in $z_{\rm P1}$, and 20 mags in $y_{\rm P1}$. The resulting homogeneous optical and near-infrared coverage of three quarters of the sky makes the Pan-STARRS1 data ideal for studies of the distribution of the

Galaxy's dust.

### 2.1.2 Two Micron All Sky Survey

The Two Micron All Sky Survey (2MASS) is a uniform all-sky survey in three near-infrared bandpasses, $J$, $H$ and $K_s$ (Skrutskie *et al.* 2006). The survey derives its name from the wavelength range covered by the longest-wavelength band, $K_s$, which lies in the longest-wavelength atmospheric window not severely affected by background thermal emission (Skrutskie *et al.* 2006). The survey was conducted from two 1.3-meter telescopes, located at Mount Hopkins, Arizona and Cerro Tololo, Chile, in order to provide coverage for both the northern and southern skies, respectively. The focal plane of each telescope was equipped with three $256 \times 256$ pixel arrays, with a pixel scale of $2'' \times 2''$. Each field on the sky was covered six times, with dual 51-millisecond and 1.3-second exposures, achieving a $10\sigma$ point-source depth of approximately 15.8, 15.1 and 14.3 mag (Vega) in $J$, $H$ and $K_s$, respectively. Calibration of the survey is considered accurate at the 0.02 mag level, with photometric uncertainties for bright sources below 0.03 mag (Skrutskie *et al.* 2006).

### 2.1.3 Source Selection

We match each PS1 source to the nearest source in the 2MASS point-source catalog, rejecting stars at greater than $2''$ separation. We require detection in at least four passbands, two of which must be PS1 passbands. In order to reject extended sources, we require that $m_{\mathrm{psf}} - m_{\mathrm{aperture}} < 0.1$ mag in at least two PS1 passbands. We additionally reject sources flagged as extended sources in 2MASS.

Individual PS1 passbands are rejected if they have photometric uncertainty greater than 0.2 mag,

Table 2.1: Pixelization

| `nside` | Max. Stars / Pixel | Solid Angle at Resolution (deg$^2$) | # of Pixels |
|---|---|---|---|
| 64 | 200 | 77 | 91 |
| 128 | 250 | 90 | 430 |
| 256 | 300 | 11980 | 228373 |
| 512 | 800 | 16071 | 1225471 |
| 1024 | 1200 | 2957 | 901971 |
| 2048 | — | 66 | 80956 |
| total | — | 31240 | 2437292 |

or if the sources are beyond or close to the saturation limit for PS1 (here considered 14.5, 14.5, 14.5, 14 and 13 mag in $grizy_{\rm P1}$, respectively). In 2MASS passbands, we make the recommended "high-reliability catalog" selection cuts,* in addition to the following requirements:

- `contamination/confusion flag` $= 0$,
- `galaxy contamination flag` $= 0$.

Our final catalog contains 798,611,689 sources, of which 32% are detected in four passbands, 49% in five passbands, and 19% in six or more passbands.

## 2.2 Pixelization

We divide the sky into HEALPix pixels (Gorski *et al.* 2005), adjusting the pixel scale in order to keep the number of stars per pixel roughly constant (see Fig. 2.1). Our procedure is to begin with `nside` $= 64$ pixels, and then subdivide each pixel recursively, as long as the number of stars exceeds some threshold, dependent on the pixel scale. We use thresholds given in Table 2.1, chosen to allow

*For a full description of the 2MASS "high-reliability catalog" requirements, see the 2MASS All-Sky Data Release Explanatory Supplement: `http://www.ipac.caltech.edu/2mass/releases/allsky/doc/sec1_6b.html#composite`.

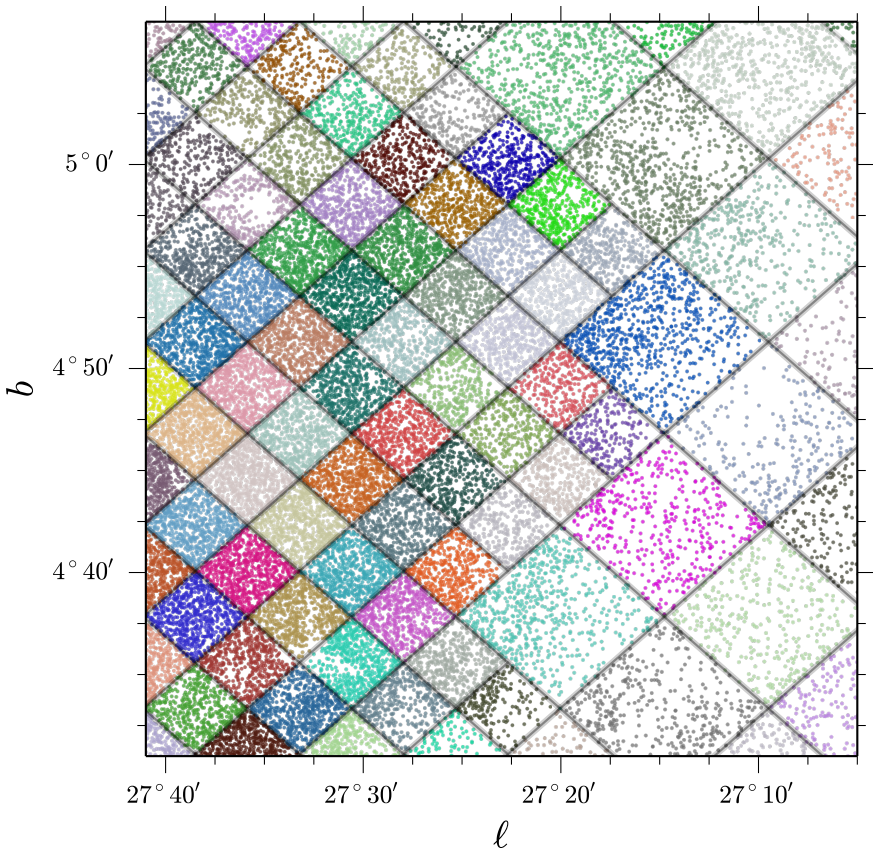


Figure 2.1: Assigning stars to different pixels, in which the line-of-sight dust profile will be fit independently. Here, each dot represents a point-source detection, and the dots are colored by the HEALPix pixel they are assigned to. The pixel scale varies in order to keep the number of stars per pixel roughly constant. Note that some pixels show significant extinction-induced variations in stellar density.

us to reach a resolution of `nside` $= 512$ with a relatively small number of stars, but to avoid going to higher resolutions unless the stellar density is much higher. We reject pixels with fewer than ten stars. Such pixels comprise a negligible fraction of the sky. In all, we assign just under 800 million stars, covering just over three quarters of the sky, to 2.4 million pixels, with an average of 327 stars per pixel.

## 2.3 Stellar Templates

In order to infer stellar types, distances and reddenings, we require a set of templates that give the absolute magnitude of stars of different types. As described earlier, we parametrize stellar type by $r_{\rm P1}$-band absolute magnitude and metallicity: $\vec{\Theta} = \{\mathcal{M}_r,\ [\rm Fe/H]\}$.

We adopt a set of empirical stellar templates based on stellar observations in PS1, with photometric parallaxes and metallicities derived from the work of Ivezić *et al.* (2008b). That work determines the absolute magnitude of a star as a function of its intrinsic color and metallicity, using observations of globular clusters in SDSS. These globular clusters are uniformly old, and as a result our stellar templates are appropriate only for old populations and do not include age as a parameter. This means that young blue stars are not included, and that the morphology of the subgiant and giant branches is only approximate. Accordingly, our giant branch distances are less reliable than our main sequence distances. Nevertheless, we include the giant branches in our models because any given star may indeed be a distant giant rather than a nearby dwarf.

The colors of our stellar templates are derived from stellar colors near the North Galactic Pole. We select $\sim$1 million stars with $\mathrm{E}(B-V)_{\rm SFD} < 0.1$ mag, detections in all PS1 and 2MASS passbands, and photometric errors less than 0.5 mag in every passband. The resulting sample has a median reddening of 0.016 mag in $\mathrm{E}(B-V)$. After dereddening the photometry, we fit a stellar locus in 7-dimensional color space, using the algorithm laid out in Newberg & Yanny (1997). The resulting stellar locus is plotted in Fig. 2.2. All main-sequence stars are required to have intrinsic colors lying along this one-dimensional curve.

We then associate each position along the main sequence with an absolute magnitude and a metallicity using the relations of Ivezić *et al.* (2008b), which give absolute magnitude as a function of color and metallicity. Models for the giants are obtained from linear fits of absolute magnitude to color and metallicity by Ivezić (private communication), based on observations of globular clusters. These giant branch fits are joined to the main sequence via a cubic interpolating polynomial for $4 > M_r > 2.35$. We are able to use relations derived from SDSS because of the close similarity between the PS1 and SDSS filter sets; we transform from the PS1 to SDSS colors using the color transformations of Finkbeiner et al. (in prep.), which have residuals of less than about 1% across the full range of stellar types considered in this work.

Our empirical approach produces a close match to the observed colors of stars, and comparison with Globular and Open Clusters indicates that the absolute magnitudes are accurate along the main sequence (See § 3.2.2). An alternative approach would have been to adopt template colors from a library of synthetic spectra, such as the Padova & Trieste Stellar Evolution Code (PARSEC; Bressan *et al.* 2012), giving us access to age as an additional stellar parameter. However, the synthetic libraries have difficulty reproducing the colors of M-dwarfs in detail. We choose therefore to adopt a set of empirical models that match the colors of most stars well, though in future work a hybrid approach may be best suited to the problem.

Briefly, metallicity-independent main-sequence stellar colors were obtained by fitting a stellar locus in color-color space, and metallicity-dependent absolute magnitudes were obtained from the metallicity-dependent photometric parallax relation given in Ivezić *et al.* (2008b). For the giant branch, linear fits to globular cluster color-magnitude diagrams from Ivezić *et al.* (2008b) were used.

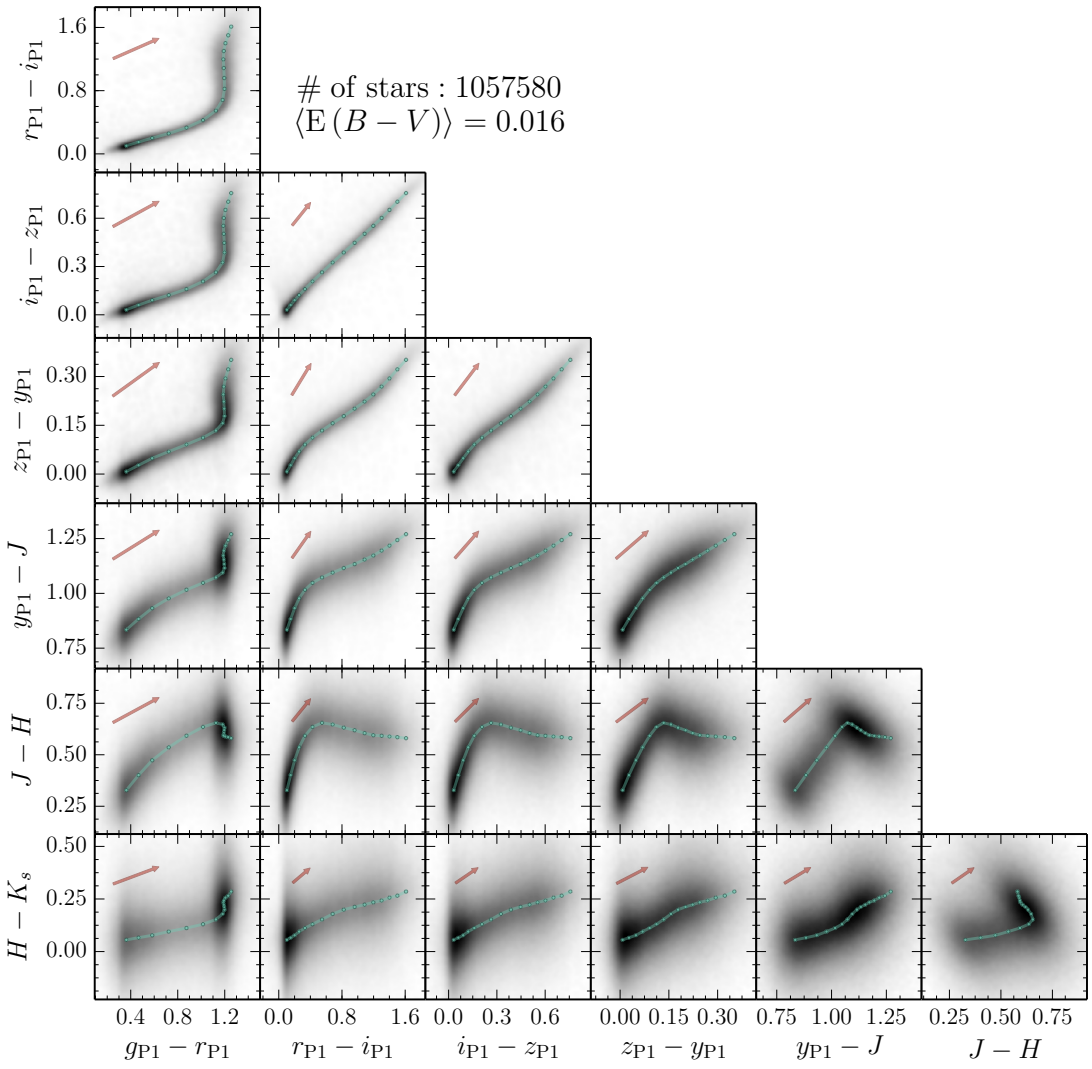


Figure 2.2: Stellar locus fit in join PS1-2MASS color space. For this fit, $\sim$1 million stars in the vicinity of the North Galactic Pole, with SFD reddening less than 0.1 mag in E($B-V$), were used. The fitted stellar locus anchor points are plotted over the density of stars in each color-color projection. A reddening vector with magnitude 0.5 mag in E($B-V$) is overplotted for each combination of colors.

## 2.4 Survey Completeness

As discussed in § 1.4.1, in order to avoid Malmquist bias in photometric inferences, it is necessary to characterize the survey selection function, which we characterize this as the detection probability in each passband as a function of apparent magnitude and position on the sky. Denote the detection or non-detection of a point source on a particular location on the sky in passband $i$ as a binary variable, $S_i$. Denote the intrinsic (or modeled) apparent magnitude of the star in passband $i$ as $m_{\mathrm{mod},\,i}$. The detection probability is written as

$$p(S_i \mid m_{\mathrm{mod},\,i}) \ . \tag{2.1}$$

For point-source detections in PS1, we model the detection probability based on the sky background, read noise and point-spread function. We do this by way of comparison with the 275 deg$^2$ SDSS Stripe 82 survey (York *et al.* 2000; Annis *et al.* 2014). The co-added Stripe 82 images go more than a magnitude deeper than the individual PS1 $3\pi$ images, allowing us to use Stripe 82 detections as a complete catalog of point sources past the detection limits of the PS1 $3\pi$ survey. For each Stripe 82 source, we deteremine whether there is a Pan-STARRS 1 detection within $1''$. The completeness fraction of the PS1 $3\pi$ survey is the percentage of Stripe-82 detections with a PS1 match.

We determine the completeness fraction of the PS1 $3\pi$ survey as a function of

$$\Delta m \equiv m - m_{\mathrm{lim}} \ , \tag{2.2}$$

where $m$ is the PS1 magnitude, and $m_{\rm lim}$ is an estimate of the local PS1 $5\sigma$ magnitude limit, based on the point-spread function of nearby PS1 detections and local sky and read noise. We divide the SDSS Stripe 82 footprint into HEALPix `nside` $= 128$ pixels (with $\sim 27'$ scale). In each pixel, we select all Stripe-82 detections classified as stars, and transform their *ugriz* magnitudes to $grizy_{\rm P1}$, using color transformations derived by Finkbeiner (in prep.), based on standard-star catalogs. In each pixel, we determine the PS1 limiting $grizy_{\rm P1}$ magnitudes from the median limiting magnitudes estimated for individual PS1 detections. For each Stripe 82 detection in the pixel, we obtain $\Delta m$ in each band by subtracting the local limiting magnitude from the transformed detection magnitude. In each passband, we bin Stripe 82 detections by $\Delta m$, obtaining an empirical estimate of the completeness in each bin from the number of PS1 matches.

We find that the completeness fraction is reasonably well fit by

$$p(S_i = \text{true} \,|\, m_{\text{mod},\,i}) = \left[1 + \exp\left(\frac{m_{\text{mod},\,i} - m_{\text{lim},\,i} - \Delta m_1}{\Delta m_2}\right)\right]^{-1}, \tag{2.3}$$

where $m_{\text{lim},\,i}$ is a limiting magnitude calculated for each point-source detection in the PS1 $3\pi$ survey, equal to the magnitude of a source that would be detected at $5\sigma$ in one exposure, given the sky and read noise. $\Delta m_1 = 0.16$ mag and $\Delta m_2 = 0.2$ mag are fitting parameters. The positive value of $\Delta m_1$ indicates that the PS1 pipeline goes somewhat deeper than our naive estimate $m_{\rm lim}$. The same fitting parameter values reproduce the completeness curve in all five PS1 passbands reasonably well, reflecting the consistency of the PS1 optics and pipeline across the entire filter set. The empirically measured completness fraction and our fit are plotted for each passband in Fig. 2.3.

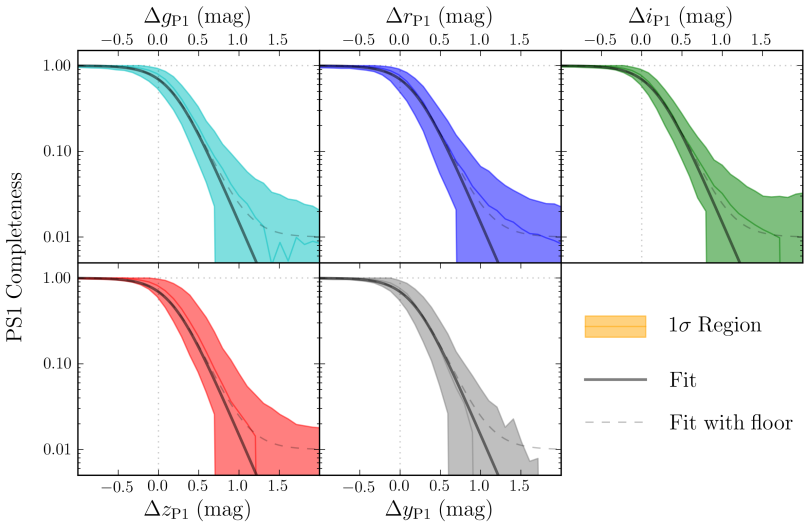


Figure 2.3: Completeness of the PS1 $3\pi$ survey, as a function of magnitudes past a locally estimated $5\sigma$ magnitude limit. The completeness is estimated by comparison with SDSS Stripe 82 (York *et al.* 2000; Annis *et al.* 2014). The shaded curve shows the median completeness, with $1\sigma$-range of completeness in each bin, based on estimates in 27' pixels. The solid black line shows our fit to the completeness curve. The dashed black line shows the effect of adding a small floor to our fit, which takes into account an assumed small rate of false coincidences between PS1 and Stripe 82 detections.

As the 2MASS point-source catalogs do not contain detailed completeness information, we model the 2MASS selection function empirically, from the histogram of detections as a function of apparent magnitude across the sky.

There are two ways to approach this problem. The first approach is to construct a full forward model, drawing stellar types, locations and reddenings from our Galactic and stellar priors, generating model photometry for the simulated stars, and applying a trial selection function and photometric errors to obtain a sample of simulated "observed" apparent magnitudes. One would then vary the selection function until the histogram of detections versus observed apparent magnitude matched observed histogram in a given region of the sky. This method suffers from its reliance on our relatively crude priors on Galactic reddening, and its sensitivity to any errors in our Galactic and stellar priors.

We therefore opt for a simpler approach. We make the assumption that near the limiting magnitude, the true sky density of objects is a smooth function of apparent magnitude. In small patches of the sky, we locate the turnoff in the histogram of detections, $m_{\mathrm{to},\,i}$, as a function of apparent magnitude. In the range $-3.5 < m_i - m_{\mathrm{to},\,i} < -0.1$, we model the logarithm of the number of detections in each apparent magnitude bin as a third-order polynomial in magnitude. This is our smooth estimate of the intrinsic sky density of sources as a function of apparent magnitude. For each 2MASS passband, we define the limiting magnitude as the bin in which the observed sky density per unit magnitude falls below 50% of the estimated true sky density per unit magnitude.

We use this procedure to construct maps of the 2MASS $J$, $H$ and $K_s$ limiting magnitudes at two HEALPix resolutions, `nside` $=$ 32 and 64. In each region of the sky, we adopt the `nside` $=$ 64

map, unless the given pixel contains fewer than 1000 detections in the given passband, in which case we switch to the lower resolution, `nside` $=$ 32 map of limiting magnitude. Fig. 2.4 shows the resulting, multi-resolution map of limiting magnitude in each passband.

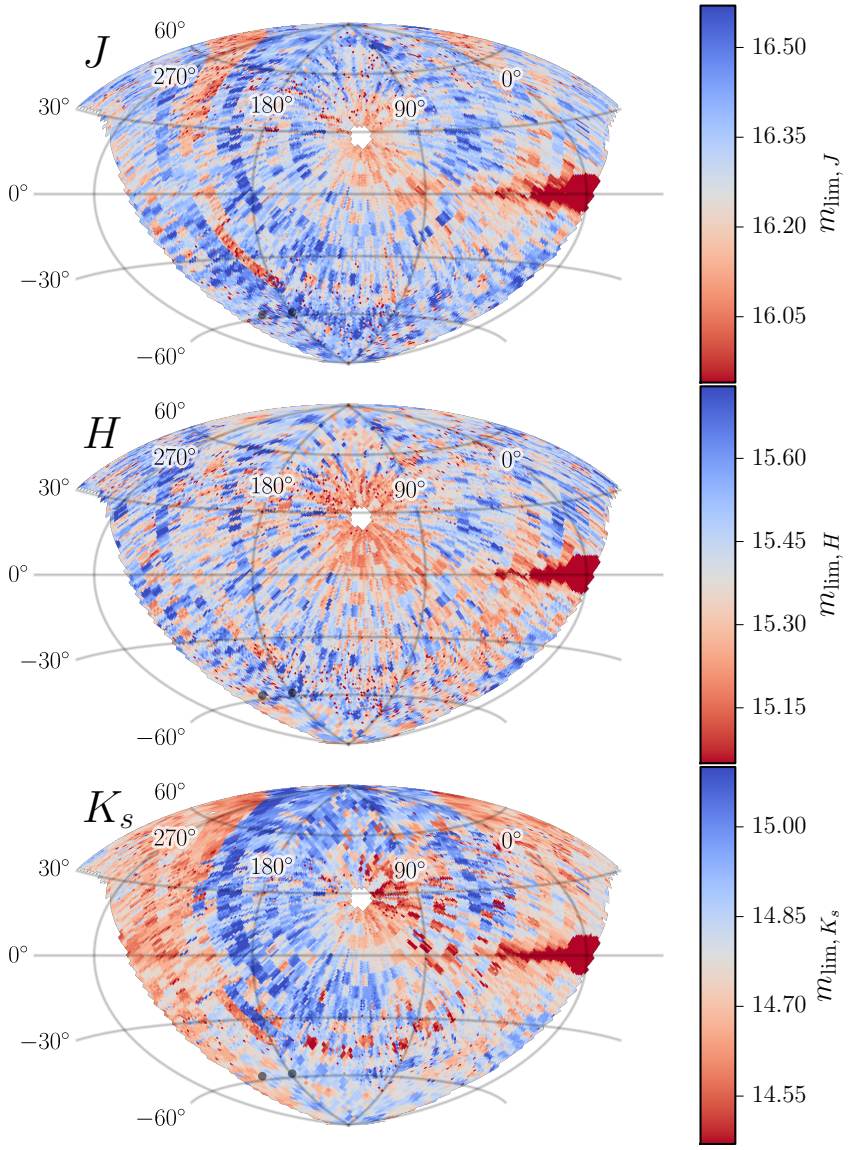


Figure 2.4: Limiting magnitude of the 2MASS survey in all three passbands, across the PS1 survey footprint. The limiting magnitude is defined as the apparent magnitude at which 50% of point sources are detected. Effective survey depth is relatively uniform over most of the sky, but falls off precipitously towards the Galactic Center due to source crowding.

*Again, do you not see that even stones are conquered by time, that tall turrets fall and rocks crumble, that the gods' temples and their images wear out and crack, nor can their holy divinity carry forward the boundaries of fate, or strive against nature's laws? Again, do we not see the monuments of men fall to pieces, [asking whether you believe that they in their turn must grow old?] Do we not see lumps of rock roll down torn from the lofty mountains, too weak to bear and endure the mighty force of time finite? For they would not fall thus suddenly torn off, if they had endured all through from time infinite and all the wrenchings of the ages without breaking up.*

Lucretius, *de rerum natura*, 5.306–317

# 3

# Validation

This chapter validates the model developed in §§ 1 and 2, by applying it both to simulated data, in § 3.1, and to real data, in § 3.2. The goal of this chapter is to verify that we can recover accurate and unbiased inferences about individual stars and line-of-sight distance–reddening profiles from stellar photometry, both simulated and real.

## 3.1 Tests with Mock Photometry

The first and most straightforward test of our method is to generate mock photometry for stars of varying stellar type, distance and extinction, and to see how well we can recover those parameters. This is less of a test of the particular stellar model used than a demonstration that photometry alone is capable of sufficiently constraining stellar parameters. We find that our method is capable of accurately recovering both single-star parameters and the line-of-sight reddening profile. In the mock-photometry tests described here, we use only PS1 passbands, rather than the full PS1+2MASS model.

### 3.1.1 Generating Mock Catalogs

In order to generate a mock photometric catalog for a particular region on the sky, we begin by drawing intrinsic stellar types (metallicities and absolute $r_{\mathrm{P1}}$ magnitudes) and distances from our priors (See § 1.2.2). We assign a reddening to each star, either according to an assumed distance – reddening relationship, or from a reddening distribution we define, depending on the purpose of the mock catalog. For each star in the catalog, we generate model magnitudes, as described in §§ 1.2.1 and 2.3.

We determine which passbands each star is detected in, according to our probabilistic completeness model, Eq. (2.3). In the remainder of the tests with mock photometry described in this thesis, we use PS1 passbands only, and reject simulated stars which do not have detections in all PS1 passbands.

We apply magnitude-dependent Gaussian photometric errors to each simulated star to obtain observed magnitudes. The error we apply to each star in each passband is a function of the model apparent magnitude:

$$\sigma^2(m) = \sigma_{\rm floor}^2 + \sigma_0^2 \exp\left[\frac{2\,(m - m_{\rm lim})}{\Delta m_3}\right] . \tag{3.1}$$

As before, $m_{\rm lim}$ is the $5\sigma$ limiting magnitude in the given passband. We set the error floor to $\sigma_{\rm floor} = 0.02$. For PS1 passbands, we find that $\sigma_0 = 0.16$ and $\Delta m_3 = 0.8$ give a reasonable fit to the photometric uncertainties.

Our final catalog thus contains noisy observed magnitudes of each star, along with the photometric uncertainty in each passband. As a final step, we plug the observed magnitudes back into Eq. (3.1) to obtain a new estimate of the photometric uncertainties for each star. The final catalog that we pass to our pipeline thus reports inexact photometric uncertainties, much as a realistic catalog would. The usefulness of these mock catalogs is that they allow us to generate a large amount of photometry for stars whose 'true" distances and reddenings are known.

### 3.1.2 Single-Star Tests

We illustrate the typical appearance of single-star posterior distributions in distance and reddening in Fig. 3.1. For each of the four simulated stars in Fig. 3.1, the "true" distance and reddening are indicated by a dot, while the background heat map shows the probability density inferred by our pipeline.

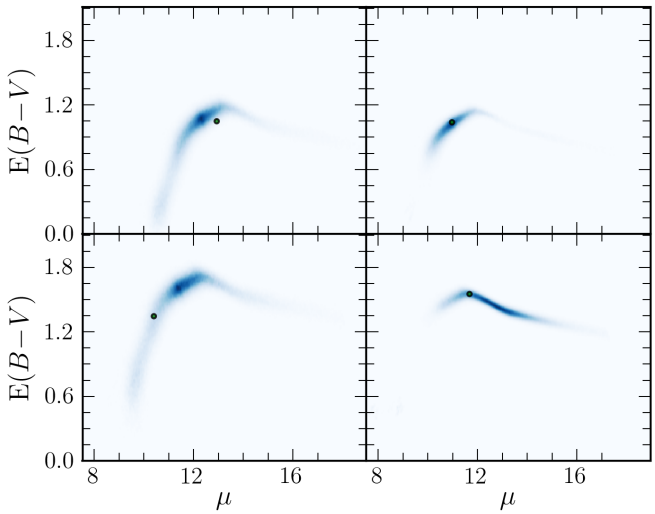


Figure 3.1: Distance and reddening estimates for four simulated stars. The joint posterior in distance and reddening is shown as a heat map. As this is mock photometry, we know the "true" distances and reddenings for the stars, which are shown as green dots. The true stellar parameters lie in regions of high inferred probability, as expected. The shape of the probability density functions traces that of the stellar locus. The probability density at closer distances corresponds to the main sequence, with increasing reddening compensating for the bluer intrinsic colors as one travels up the stellar locus. The peak in reddening corresponds to the main-sequence turnoff. Distances beyond the turnoff correspond to the giant branch.

In order to determine how far off our estimates are on average, we define the centered probability density

$$\tilde{p}(\Delta\mu,\ \Delta E) \equiv \frac{1}{N}\sum_{i=1}^{N} p(\mu_i^* + \Delta\mu,\ E_i^* + \Delta E)\ , \tag{3.2}$$

where $\mu_i^*$ and $E_i^*$ are the true distance modulus and reddening, respectively, for star $i$. For a simulated line-of-sight, this function gives the average probability density of our inference being offset from the true stellar parameters by $(\Delta\mu,\ \Delta E)$. We plot $\tilde{p}$ for a typical line of sight in Fig. 3.2. The typical spread of in $\Delta\mu$ and $\Delta E$ varies across different lines of sight, but the centered probability density generally peaks at the origin, as should be expected. In the bottom two panels of Fig. 3.2, we show the effect of applying flat priors to the stellar parameters, in place of the priors developed in § 1.2. The effect is to widen and bias the inferred probability density functions. Due to the near-alignment of the reddening vector with the PS1 stellar locus for much of the main sequence, this bias remains even for stars with low observational uncertainties. The stellar priors are thus important in correctly inferring stellar parameters from Pan-STARRS 1 photometry. In the right two panels of Fig. 3.2, we only use inferences for stars with low signal-to-noise detections. The low signal-to-noise population is generated using an inflated error model that applies $3\times$ the normal observational uncertainty to the mock photometry. As expected, the inferred parameters for such stars are less constrained, but they are nonetheless unbiased.

In Table 3.1, we present typical uncertainties in the inferred distance and reddening of individual stars. To do this, we generate mock catalogs along two different lines of sight. For our high-Galactic-

latitude target, we choose the North Galactic Pole, where the stellar population is dominated by the halo. Here, we apply reddenings of $\mathrm{E}(B-V) \lesssim 0.1$ to the simulated stars. For the low Galactic latitude target, we choose $\ell = 45^\circ$, $b = 0^\circ$, and draw reddening uniformly from the range $0 \leq \mathrm{E}(B-V) \leq 2$. We run the two mock catalogs through our pipeline, and compare the inferred distances and reddenings, drawn from the posterior probability density $p(\mu, \mathcal{A})$, to the true values. For this test, we allow our inferred reddenings to go slightly negative ($\mathrm{E}(B-V) > -0.25$), to avoid introducing a bias into the inferred values. We give the median, and 15.87th and 84.13th percentiles of $\frac{\Delta d}{d}$ and $\Delta\mathrm{E}(B-V)$, equivalent to the one-standard-deviation range for a Gaussian distribution.

Uncertainties in distance modulus can be transformed to uncertainties in distance by making use of the relation

$$\frac{d}{10\ \mathrm{pc}} = 10^{\mu/5}\,. \tag{3.3}$$

Let $\mu_{\mathrm{inferred}} = \mu_{\mathrm{true}} + \Delta\mu$. Then,

$$\frac{\Delta d}{d} \equiv \frac{d_{\mathrm{inferred}} - d_{\mathrm{true}}}{d_{\mathrm{inferred}}} = 10^{\Delta\mu/5} - 1\,. \tag{3.4}$$

Similarly, we define $\Delta\mathrm{E}(B-V)$ as $\mathrm{E}(B-V)_{\mathrm{inferred}} - \mathrm{E}(B-V)_{\mathrm{true}}$.

Our distance and reddening estimates are unbiased. However, if one selects a subsample of stars of a certain known type, a bias in distance is introduced. Thus, distance estimates for mock dwarf stars are biased low, as the model assigns some probability to the possibility of them being giants.

Table 3.1: Uncertainty in Inferred Distances and Reddenings

| | Low Latitude | | High Latitude | |
|---|---|---|---|---|
| | $\frac{\Delta d}{d}^*$ (%) | $\Delta E(B-V)$ | $\frac{\Delta d}{d}$ (%) | $\Delta E(B-V)$ |
| $-1 < \mathcal{M}_r \leq 4$ | $-20\,^{+41}_{-30}$ | $-0.03\,^{+0.07}_{-0.12}$ | $-37\,^{+48}_{-32}$ | $-0.03\,^{+0.09}_{-0.11}$ |
| $4 < \mathcal{M}_r \leq 6$ | $6\,^{+55}_{-33}$ | $0\,^{+0.12}_{-0.20}$ | $12\,^{+79}_{-37}$ | $0\,^{+0.10}_{-0.12}$ |
| $6 < \mathcal{M}_r \leq 8$ | $23\,^{+97}_{-34}$ | $0.17\,^{+0.28}_{-0.36}$ | $8\,^{+92}_{-21}$ | $0.04\,^{+0.22}_{-0.20}$ |
| $8 < \mathcal{M}_r \leq 10$ | $33\,^{+261}_{-39}$ | $0.29\,^{+0.62}_{-0.42}$ | $4\,^{+31}_{-14}$ | $0.02\,^{+0.33}_{-0.09}$ |
| $10 < \mathcal{M}_r \leq 12$ | $5\,^{+14}_{-15}$ | $0.02\,^{+0.13}_{-0.13}$ | $1\,^{+15}_{-12}$ | $0\,^{+0.10}_{-0.09}$ |
| Dwarfs† | $9\,^{+63}_{-33}$ | $0.01\,^{+0.16}_{-0.20}$ | $4\,^{+50}_{-18}$ | $0.01\,^{+0.17}_{-0.12}$ |
| All Stars | $-3\,^{+55}_{-35}$ | $-0.01\,^{+0.12}_{-0.16}$ | $2\,^{+45}_{-23}$ | $0.01\,^{+0.16}_{-0.12}$ |

* $\frac{\Delta d}{d}$ is given in percent. See Eq. (3.4).
† Dwarfs are defined here as all stars in the range $4 < \mathcal{M}_r \leq 12$.

Inversely, distances to giants are biased high. A star drawn at random, however, has an unbiased distance estimate. Distance and reddening constraints depend upon the quality of the photometry and direction on the sky, and therefore vary significantly on a star-per-star basis. It is, in general, more informative to look at the detailed shape of the posterior distribution for a given star in distance and reddening space (See Fig. 3.1).

Next, we test that the true stellar parameters are drawn from the probability density functions we calculate. For each simulated star, we derive the posterior density $p(\mu,\ E)$, based on the simulated photometry. Since we know the true distance modulus $\mu^*$ and reddening $E^*$ of the star, a natural question is whether $\mu^*$ and $E^*$ are drawn from $p(\mu,\ E)$. This cannot be answered for a single star, but we can test this hypothesis for a large number of stars. Assign a percentile to a given star as fol-

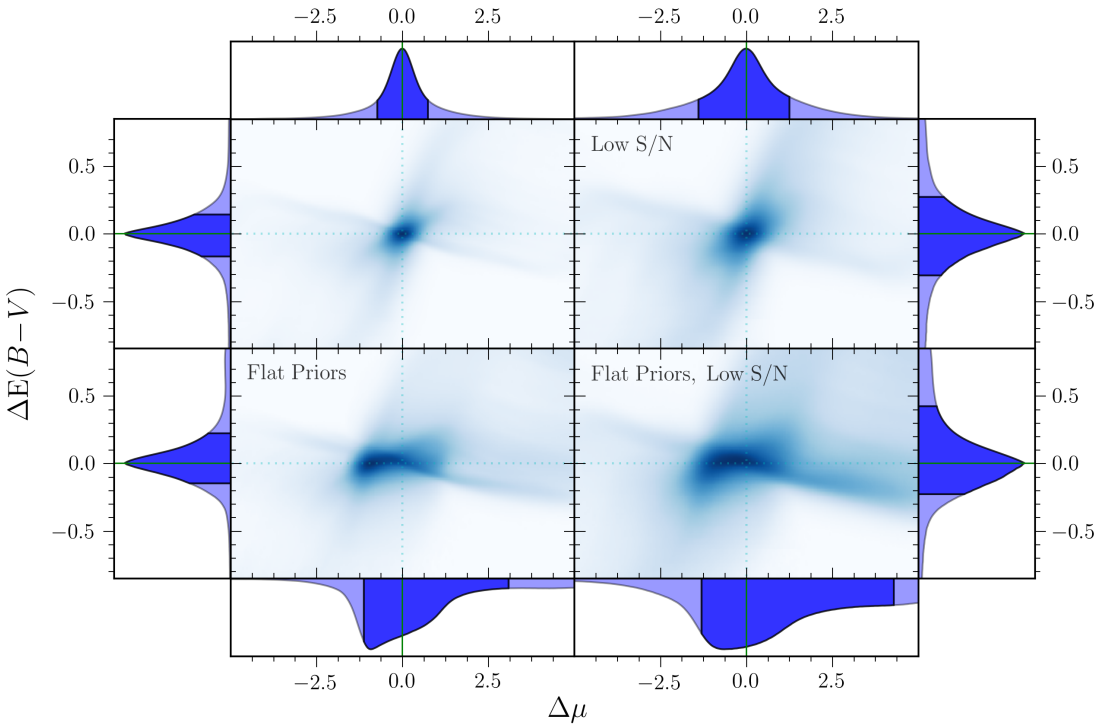


Figure 3.2: Centered and stacked probability densities on a linear scale for 5000 stars along a simulated line of sight pointed at $\ell = 90°$, $b = 20°$. In the bottom panels, we fit the stars using flat priors, so that only the likelihood function comes into play. In the right panels, we show inferences for low signal-to-noise detections, generated using $3\times$ the normal observational uncertainties. Removing the priors biases the inferred distances and, to a much lesser extent, reddenings. Inferred distances and reddenings for stars with high signal-to-noise detections have smaller uncertainties. In each panel, each stellar probability density function has first been centered on the true distance and reddening, before the probability densities for the stars have been summed, as described in the text. The "X" shape of the stacked probability densities in the top-left panel reflects the existence of separate giant and dwarf modes. The feature stretching from the bottom left to the top right corresponds to the main sequence, while the perpendicular feature corresponds to the giant mode. The histograms bordering each panel show the distribution of $\Delta\mu$ and $\Delta\mathrm{E}(B-V)$, with the 15.87% to 84.13% region shaded.

lows:

$$P(\,p < p^*) \equiv \int_{p(\mu,\,E\,)\,<\,p^*} \mathrm{d}\mu\,\mathrm{d}E\;p(\mu,\,E\,)\;, \tag{3.5}$$

where $p^* \equiv p(\mu^*,\,E^*)$. This represents the probability that the true stellar parameters would be found at a point in $(\mu, E)$-space of lower posterior density. If $(\mu^*, E^*)$ lies at the point of maximum posterior density, then $P(\,p < p^*) = 1$. Conversely, if $(\mu^*, E^*)$ lies in a region of vanishing probability density, then $P(\,p < p^*) \approx 0$. This percentile is therefore similar to a cumulative distribution function, and is uniformly distributed between 0 and 1. A straightforward test of whether $P(\,p < p^*) \sim U(0,\,1)$ is to generate mock photometry for a large number of stars, to calculate the percentile for each simulated star, and to then bin the results. Each bin is expected to contain the same number of stars, with the precise number of stars in the bins determined by a multinomial distribution. We can therefore derive approximate confidence intervals for the number of stars that should fall into any given bin. Fig. 3.3 shows this test for a set of 1000 simulated stars along a line of sight with Galactic coordinates $\ell = 90°$, $b = 10°$. The results are consistent with our expectations, indicating that our method recovers correct posterior densities for the simulated photometry.

### 3.1.3 Mock Line of Sight

Finally, we demonstrate that we are able to recover line-of-sight reddening profiles for simulated photometry. We first invent an arbitrary relationship $\mathrm{E}(B-V)(\mu)$ between distance and reddening. We add in low-level scatter to the distance-reddening relationship, as the reddening relation across

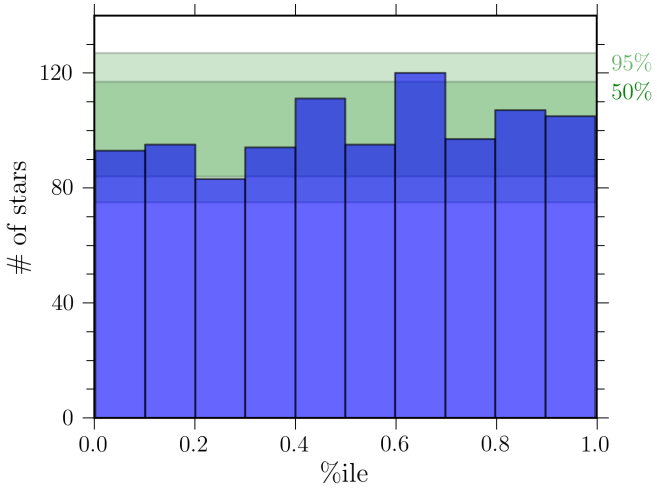


Figure 3.3: Distribution of percentiles for simulated photometry of 1000 stars, as defined in Eq. (3.5). The percentiles are expected to be drawn from the standard uniform distribution, resulting in each bin being of equal height. In 50% of trials, we would expect all the bins to fall within the dark green band, and in 95% of trials, all the bins should lie within the light green band. The percentiles are consistent with being drawn from a uniform distribution, indicating that we are sampling from the model correctly.

one HEALPix pixel may vary. We then generate mock photometry for 150 stars along the line of sight. We then infer our model parameters from the simulated photometry, following the procedure outlined in § 1.5, first determining a posterior density in distance and reddening space for each star, and then combining the information from all of the stars to find the range of allowable reddening profiles. Our final product is thus a set of reddening profiles, drawn from the probability density over reddening profiles (See Eq. (1.12)). As described in §§ 1.3 and 1.5.3, we parameterize the reddening as a piecewise-linear function in distance, and apply a log-normal prior to the differential reddening in each distance bin, with the mean in each bin chosen to match a smooth model of the space density of dust throughout the Galaxy. The results for one simulated line of sight, shown in Fig. 3.4, demonstrate that we are able to correctly infer the reddening profile for mock data. The method

produces the best results at distances where there are many stars. We choose in this demonstration to use a finer distance binning than normal – 40 distance bins instead of the usual 30 – in order to highlight one of the degeneracies in our parameterization. Because we represent the distance–reddening relation by a piecewise-linear function, clouds can only appear at discrete distances. This sometimes leads to a cloud being placed at different discrete distances in different MCMC samples, as can be seen in Fig. 3.4.

## 3.2 Tests with Real Data

We have found that we can recover stellar distances and reddenings, as well as line-of-sight distance–reddening profiles, from simulated photometry. These tests assume that our stellar templates are perfect, which is surely not the case. In this section, we therefore show that our stellar templates have accurate colors and luminosities, and that our rejection method (See § 1.5.2) can screen areas of stellar parameter space that are not well represented by the models.

### 3.2.1 Colors

We compare our model colors to PS1 stellar photometry from low-extinction regions at high Galactic latitudes. It is important to choose low-extinction regions, so that assumptions about the reddening law and what percentage of the total dust column is in front of each star play only a minor role. This allows us to obtain a comparison between the intrinsic colors in our model and of real stars. We de-redden the stellar colors assuming that they are behind the full dust column predicted by Schlegel *et al.* (1998, SFD).

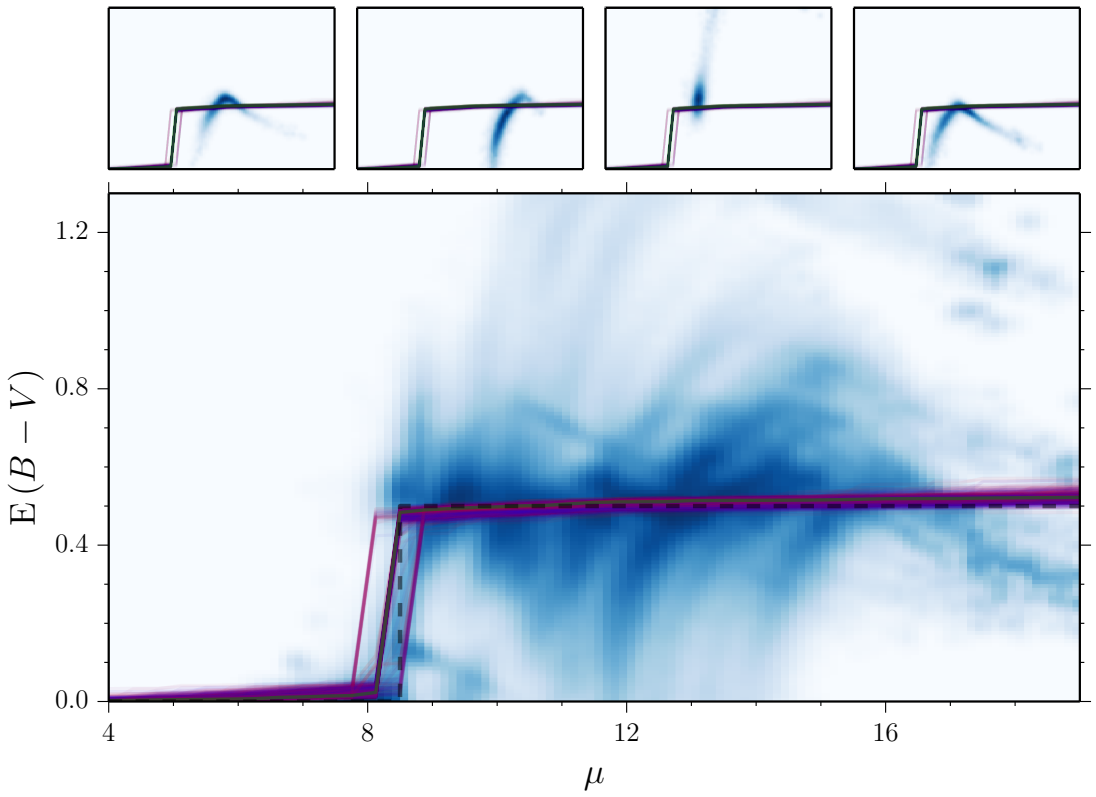


Figure 3.4: Recovery of the line-of-sight reddening profile from simulated photometry for 150 stars, taken to be at a Galactic longitude of $\ell = 90°$, and latitude $b = 10°$. The large panel shows the inferred posterior densities of the stars, stacked on top of one another. The contrast is stretched at each distance for purposes of visualization. This gives a picture of the information which is fed into the second stage of our analysis, in which we recover the reddening as a function of distance from the individual stellar probability densities (See Eq. (1.12)). The stacked image, however, plays no direct role in this inference. The curves show sampled reddening profiles, conditioned on the mock photometry. The green curve traces the most probable reddening profile. The remaining curves are colored according to the logarithm of their probability density, with blue denoting high probability and red denoting low probability. The upper four panels show individual stellar posterior density functions over the same domain, with the same reddening profiles overplotted. We recover a reddening profile similar to the original, which had a single cloud of depth $\mathrm{E}(B-V) = 0.5$ mag at distance modulus $\mu = 8.5$ (shown as a dashed black line on the plot). At large distances, beyond the most distant stars, the distance–reddening relation is constrained by the prior that there be little dust far outside the plane of the Milky Way. Each star is consistent with the range of possible reddening profiles. The cloud is inferred to lie in different distance bins in different samples, reflecting the discrete nature of our line-of-sight reddening parameterization.

The results for the North Galactic Pole are shown in Fig. 3.5. We compute an evidence for each star, as described in § 1.5.2. As expected, objects which lie far from the stellar locus in color-color space tend to have lower evidence. This helps us to reject objects that are either not stars, are not included in our stellar model (e.g., young and BHB stars), or that have particularly bad photometry. In the window shown here, 15% of the detected objects would fail an evidence cut of $\ln Z > \ln Z_{\max} - 20$. These objects tend to have problematic photometry for which the PS1 pipeline may have produced inaccurate results, though some are variables, quasars, and unrecognized galaxies, which our technique is not designed to handle. Our line-of-sight reddening inferences are not strongly dependent on the choice of the evidence threshold.

### 3.2.2 Distances

Correct distance determination requires not only correct model colors, but correct absolute magnitudes. We therefore compare our stellar models to globular and open clusters. In Fig. 3.6, we compare our model magnitudes to photometry from four globular and open clusters.

We find that the model absolute magnitudes match the main sequence. The model magnitudes are unreliable past the main sequence turnoff, particularly for younger clusters. Our model magnitudes trace the giant branch of intermediate-age clusters – typical of the age of most stars in the Galaxy – somewhat better. Nevertheless, we expect that most of the information in our dust maps will come from the main sequence, where distance and reddening estimates are better constrained. Massive young blue stars and blue horizontal branch stars, which are not included in the stellar templates, are found to have low evidence, allowing them to be identified and excluded from the line-of-

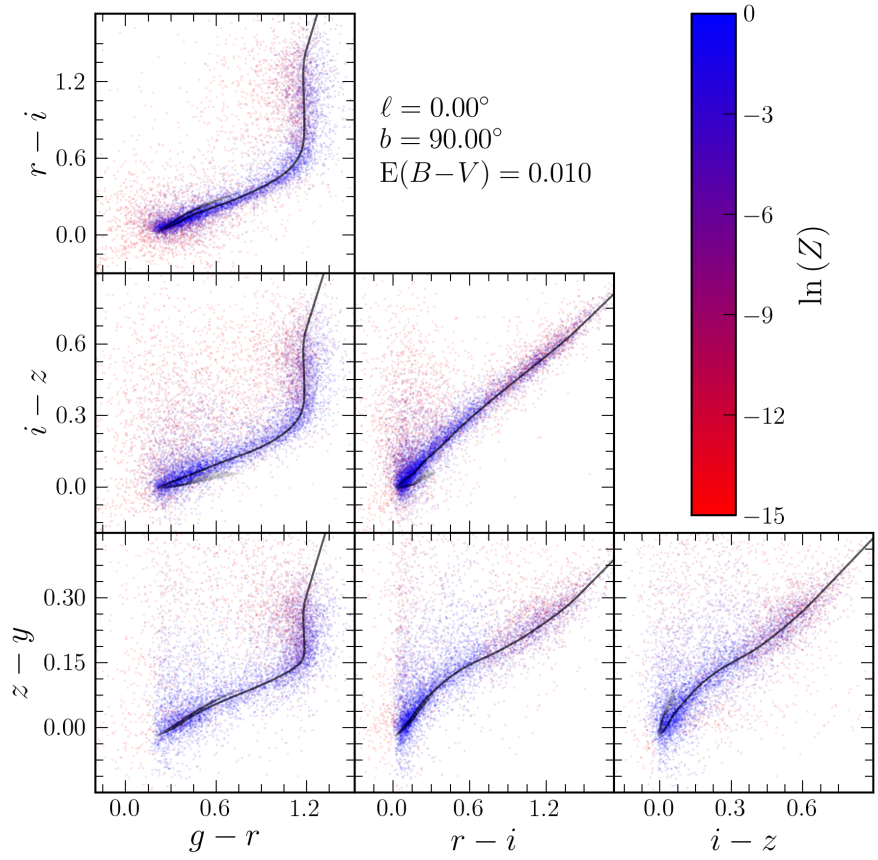


Figure 3.5: Comparison of PS1 stellar colors in the vicinity of the North Galactic Pole with our model colors. Each object is colored according to the evidence $Z$ we compute (See § 1.5.2). Objects represented by redder dots have a lower probability of being drawn from our stellar model. Those below a chosen threshold are rejected before the line-of-sight reddening determination. The solid black line traces our model stellar colors.

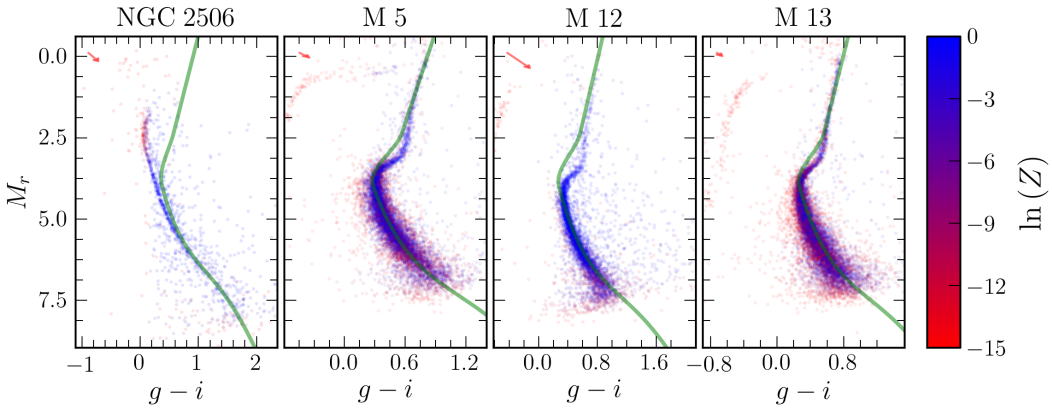


Figure 3.6: PS1 color-magnitude diagrams of three globular and one open cluster. For each cluster, the model isochrone with the catalog metallicity of the cluster is overplotted. The stellar photometry has been de-reddened and shifted by the catalog distance modulus to produce absolute magnitudes. The reddening vector is plotted in the top left corner of each panel in red for reference. Each star is colored by its evidence, with red stars unlikely to be drawn from our stellar model. In particular, stars which are blueward of the the main-sequence turnoff, which are bluer than any star in our template library, have low evidence.

sight dust inference. Inclusion of age-dependent stellar models, and therefore more reliable distance and reddening determinations for the most massive stars, could potentially increase the distance to which our dust maps are reliable, and is an important direction for future work.

*The door of death therefore is not closed for the heavens, nor for the sun and earth and the deep waters of the sea, but stands open and awaits them with vast and hideous maw. Therefore also you must confess that these same things have had their birth; for things which are of mortal body could not have despised the mighty strength of immeasurable ages from infinite time up to this present.*

Lucretius, *de rerum natura*, 5.373–379

# 4

# Results

After burning through ∼200 CPU-years on the Harvard Odyssey compute cluster, we obtain a map of dust across the entire footprint of the PS1 survey – that is, the sky north of a declination of $\delta \approx -30°$. This map is based on both PS1 and 2MASS photometry, as described in § 2. The map is built sightline-by-sightline, using the method developed in § 1, following the sampling strategy detailed in § 1.5. In this chapter, I

first showcase the map in § 4.1. Then, in § 4.2, I compare this 3D dust map with previous 2D and 3D maps. Finally, in § 4.3, I describe how to access the map.

## 4.1 Distance Slices of Map

In Figs. 4.1 and 4.2, I present the differential reddening in four spherical shells, centered on the Sun. Each panel shows the median dust reddening in a different range of Solar-centric distances. Due to perspective, dust at high Galactic latitudes resides nearby, as Galactic dust lies in a thin disk. The map recovers the wealth of structure seen in the ISM across a wide range of scales, from thin filaments to large cloud complexes. Large, coherent cloud complexes appear at consistent distances.

Fig. 4.3 gives a closer view of the anticentral region ($\ell \sim 180°$). Different features appear clearly in each rendered distance slice. The Perseus, Taurus and Auriga cloud complexes dominate the anticentral region in the closest distance slice, while the Orion molecular cloud complex ($\ell \sim 210°$, $b \sim -15°$) and the California nebula ($\ell \sim 160°$, $b \sim -8°$) appear very strikingly in the second distance slice. Of particular interest is the ring-like structure that Orion A and B appear to be embedded within. This ring-like structure is only apparent when the background dust is removed. In particular, the northeast portion of the ring is confused with the plane of the Galaxy in projection. Schlafly *et al.* (2015) discusses the "Orion ring," including possible formation scenarios for the ring, in greater depth.

Fig. 4.4 shows the Galactic plane from $\ell = 60°$ to 155° in more detail. The Cepheus flare, which lies at the center of the frame, at $95° \lesssim \ell \lesssim 110°$, $b \approx 15°$, separates into two components at different distances, visible in the first and third panels. Using a modified version of the methods presented

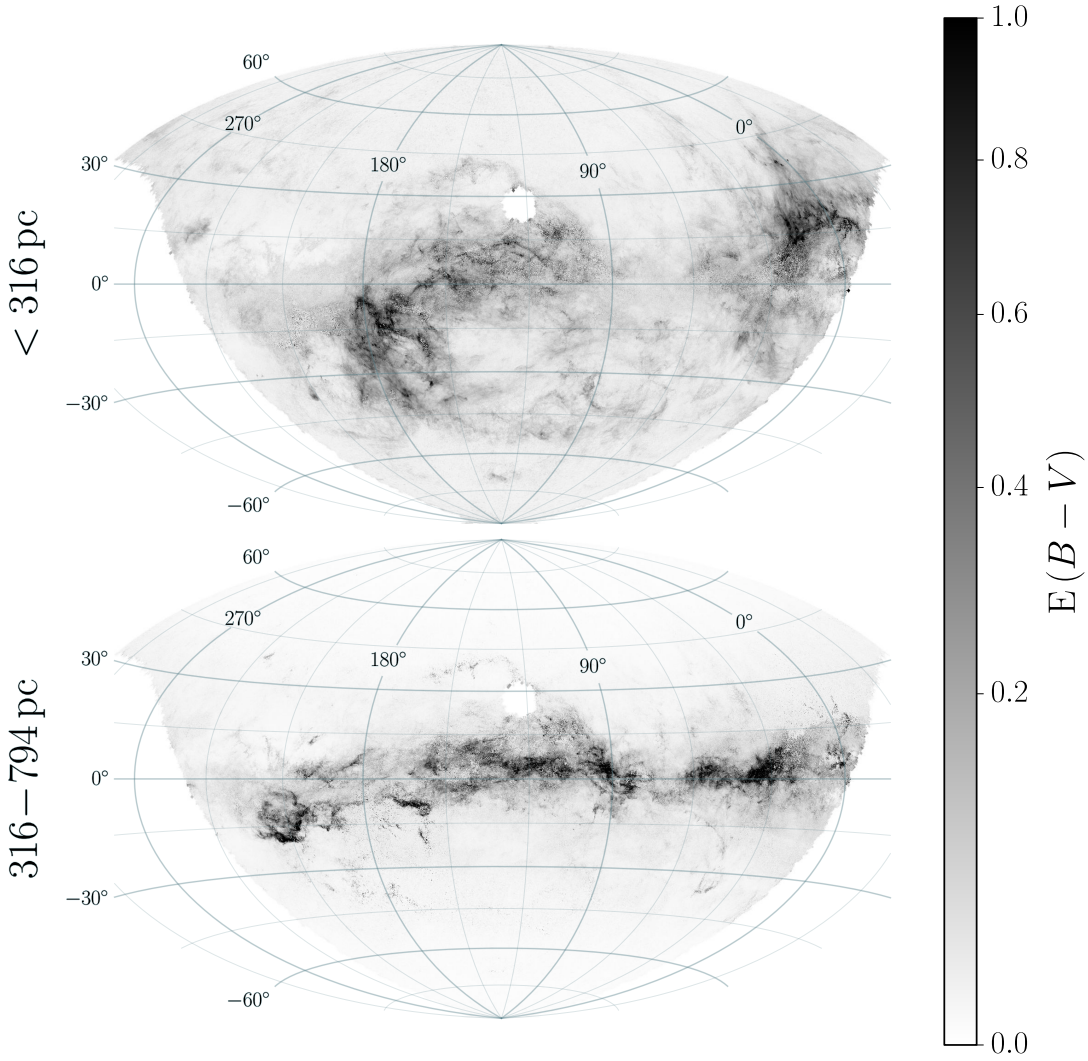


Figure 4.1: Median differential reddening in two Solar-centric distance ranges. The distance breaks are chosen to coincide with distance moduli $\mu = 7.5$ and 9.5, which line up with edges of distance bins in our map. We adopt a square-root stretch, in order to capture both low- and high-reddening features. The hole at $\ell \approx 120°$, $b \approx 30°$ corresponds to declinations above $\sim 84°$, which had not yet been fully processed at the time we created our 3D map.

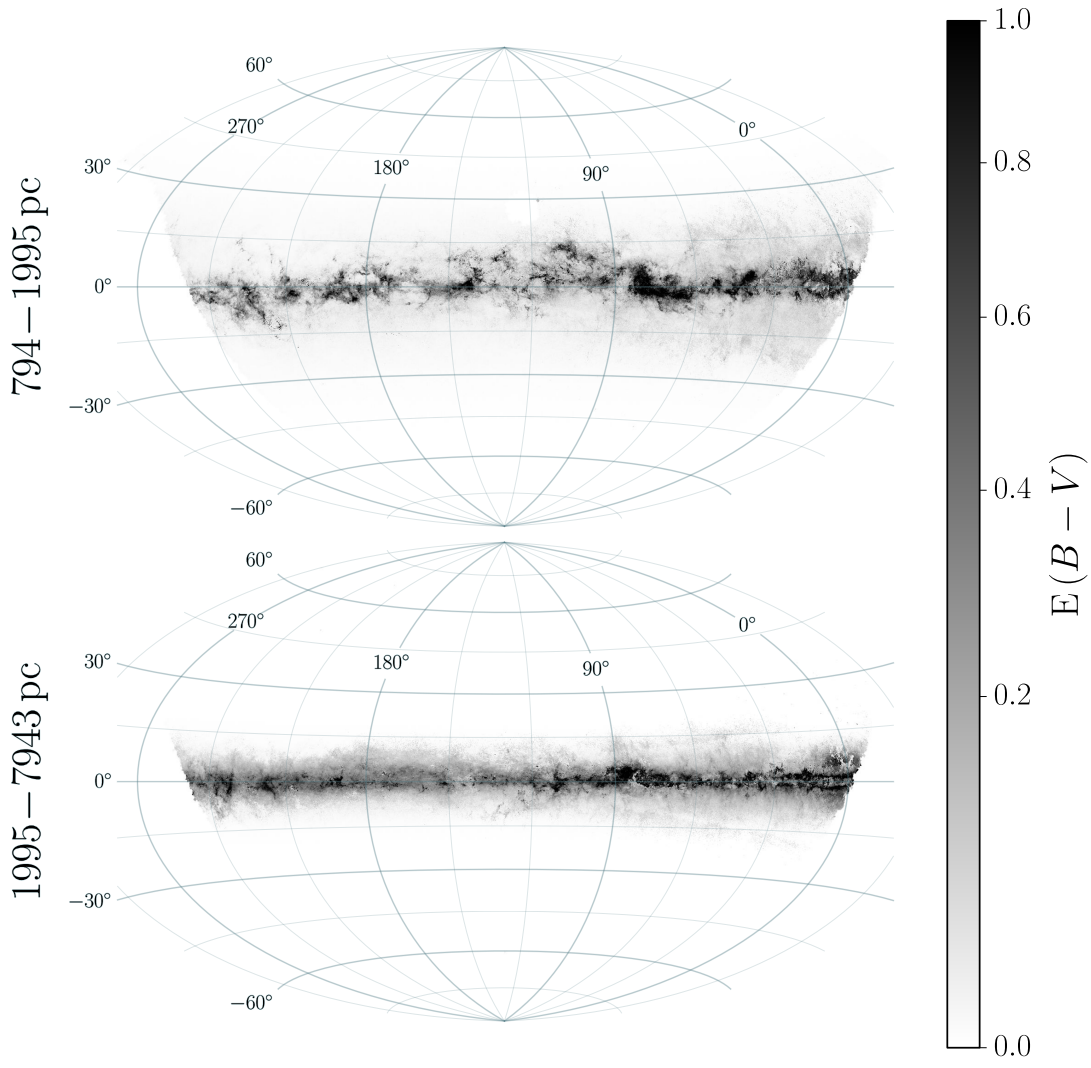


Figure 4.2: As in Fig. 4.1, but with breaks at distance moduli $\mu = 11.5$ and 14.5.

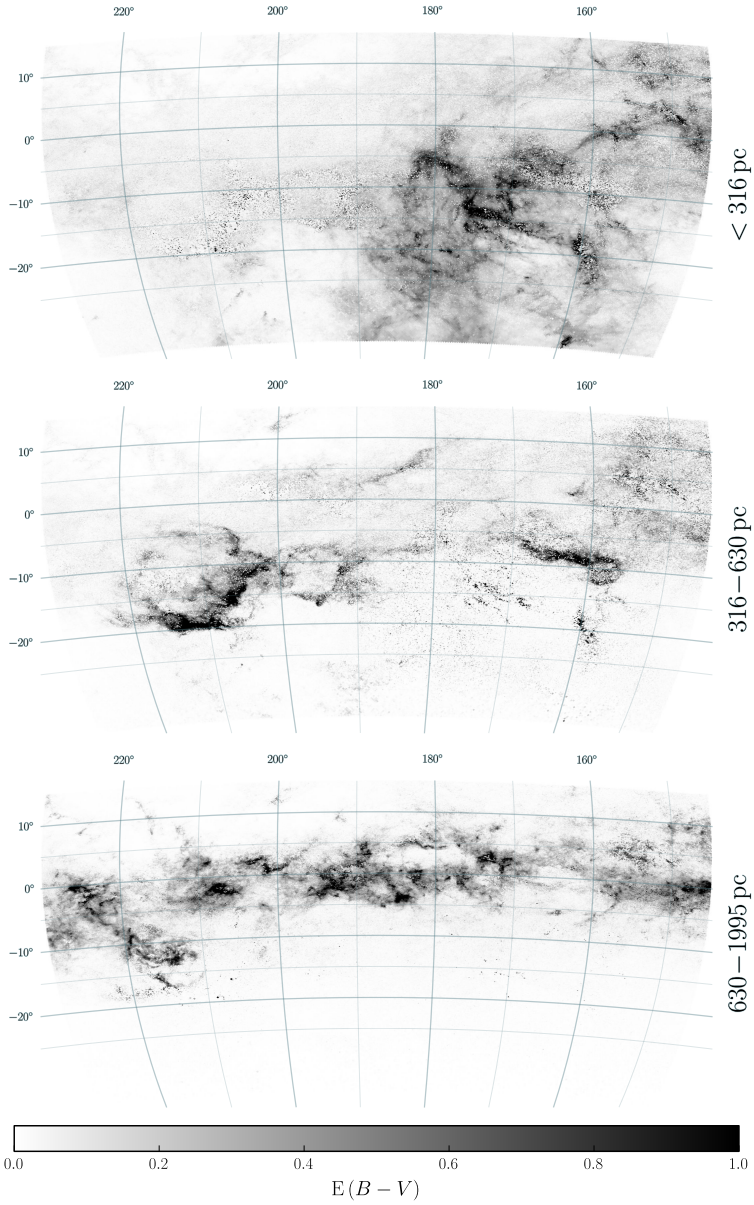


Figure 4.3: A closer view of the dust in the anticentral region in three distance bins. As in Figs. 4.1 and 4.2, we plot the median differential reddening. The Taurus-Perseus-Auriga complex is visible in the right half of the nearest distance bin. In the second distance bin, the Orion complex is visible on the left, while the California cloud is visible on the right. Note the ring-like shape of the Orion complex, which is only revealed by 3D mapping when confusion from background dust is removed. See Schlafly *et al.* (2015) for discussion of this feature. Monoceros R2 appears beyond Orion, in the third distance bin, flanked by the plane of the Galaxy at yet greater distance.

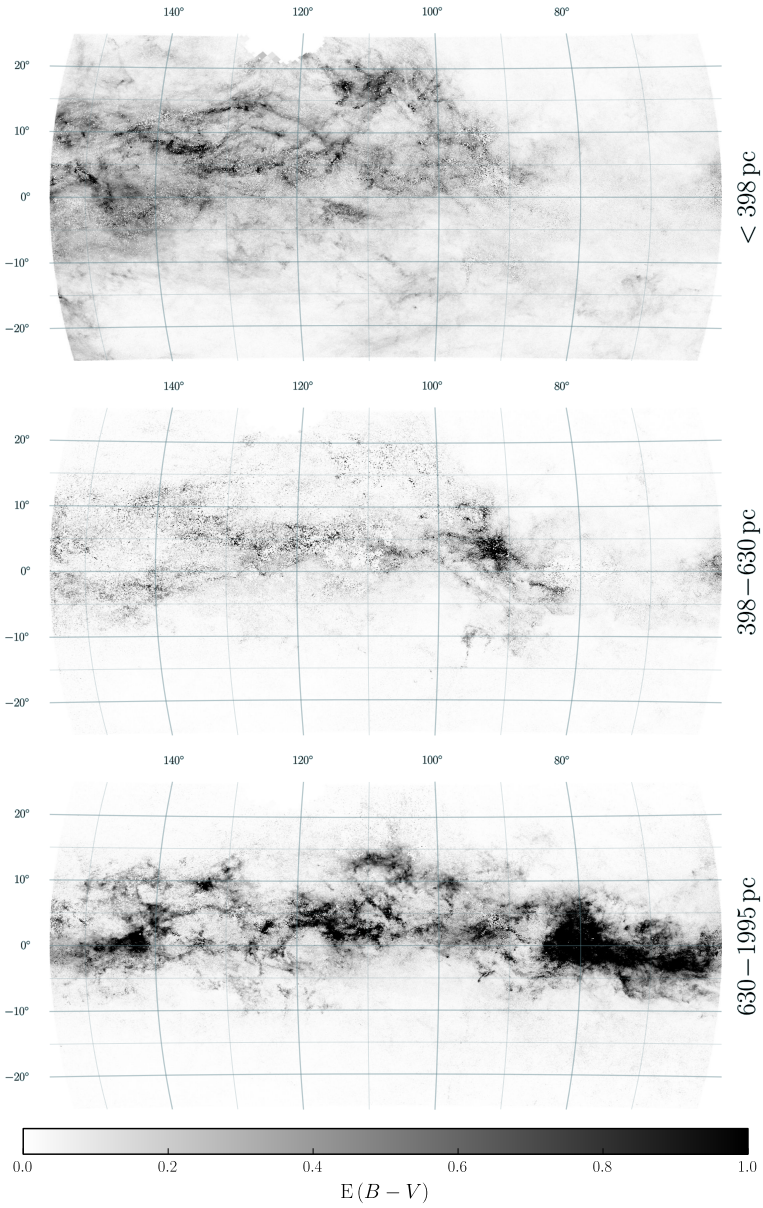


Figure 4.4: A closer view of the dust in the direction of Cepheus and Polaris flares and the eastern portion of the Great Rift, including Cygnus X. The Cepheus flare ($95° \lesssim \ell \lesssim 110°, b \approx 15°$) separates into two components in distance, visible in the first and third panels. The dust associated with the Cygnus X region ($\ell \approx 80°, b \approx 0°$) appears in the third panel.

in this thesis along individual sightlines, Schlafly *et al.* (2014b) finds that the two components of the Cepheus flare lie at distances of 360 $\pm$ 35pc and 900 $\pm$ 90pc. The dust associated with Cygnus X ($\ell \approx 80°$, $b \approx 0°$) appears in the third panel, along with a wealth of fine structure along the Galactic plane.

We note that each pixel is fit independently, and our only prior assumption about the spatial structure of the dust is that if forms a diffuse disk, as shown in Fig. 1.3. The detailed spatial structure in the interstellar medium that our analysis reveals indicates that the PS1 and 2MASS photometry dominates over our priors out to a distance of several kiloparsecs and reddening of $E(B-V) \approx$ 1.5 mag. With the assumption of spatial correlations between neighboring pixels, we expect that one would be able to significantly reduce the uncertainty in the map, and achieve better distance resolution (See, e.g., Sale & Magorrian 2014).

### 4.1.1 Maximum & Minimum Reliable Distances in Map

Our 3D dust map is based on measurements of stellar distances and reddenings. Beyond the most distant stars, we have no sensitivity to dust, and in front of the nearest stars, we have no information about the distance to the dust. Therefore, we estimate the minimum and maximum distance to which our map is reliable by locating the nearest and farthest stars in each pixel. Outside of this distance range, our line-of-sight reddening inferences are dominated by our priors. Using the improved stellar parameter inferences (described in § 1.7), we define the minimum reliable distance in each line of sight as the distance out to which there are $N_{\rm closer}$ observed main-sequence stars, and the maximum reliable distance as the distance beyond which there are $N_{\rm farther}$ observed main-sequence

stars.

For this calculation, we count each Markov Chain sample in stellar distance as a fraction of a star. We exclude stars that fail to converge, for which the model is a very poor match to the data (as determined by the Bayesian evidence for the star; See § 1.5.2), or which are inconsistent with the inferred line-of-sight reddening profile. We consider a star inconsistent with the line-of-sight reddening inference if none of the 100 stored Markov Chain samples of the stellar distance and reddening is within a fractional distance $\sigma_\delta$ (the modeled intra-pixel scatter in the dust column; See § 1.7) of the line-of-sight reddening profile. Such objects are likely not well fit by any of our stellar templates, or alternatively signal that there is more variation in the dust column at fine angular scales than we allow.

In determining the minimum and maximum reliable distances in the 3D dust map, we use only main-sequence stars. This is because we consider our inferences for giants to be less reliable than our inferences for dwarfs. The colors and luminosities of giants depend more strongly on metallicity and age, the latter of which we do not model.

In the left two panels of Fig. 4.5, we show the results obtained by requiring $N_{\mathrm{closer}} = 2$ and $N_{\mathrm{farther}} = 10$. The results are qualitatively similar for other choices of these parameters, as long as they are small compared to the typical number of stars in a pixel. The closest reliable distance is set almost entirely by the angular pixel scale. The nearby density of stars is, to a very rough estimation, uniform, meaning that the distance to the closest star in a pixel is a function primarily of the solid angle covered by the pixel. Accordingly, the top left panel of Fig. 4.5 is essentially a map of pixel solid angle, with boundaries in distance following pixel scale boundaries.

The farthest reliable distance of the 3D dust map is strongly influenced not only by the pixel

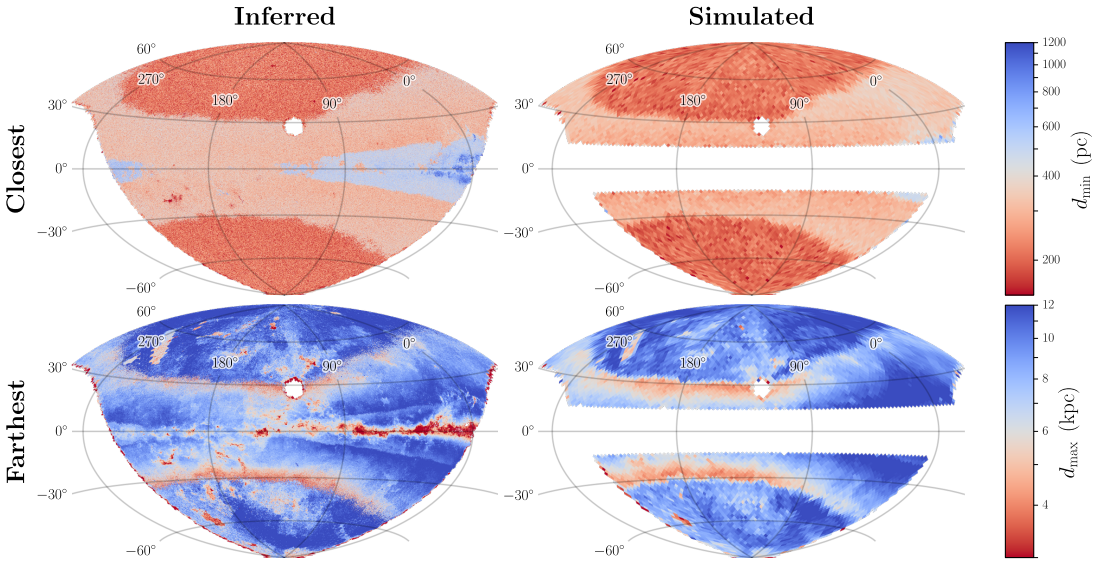


Figure 4.5: The minimum and maximum reliable distances in the 3D dust map. The left two panels are based on the inferred distribution of stars along each line of sight, while the right two panels are based on simulated stellar catalogs generated from our Galactic priors. We consider the map reliable if there are at least two stars closer than the given distance, and at least ten stars beyond the distance. Pixel size, survey depth and completeness, stellar density throughout the Galaxy and the presence of dust all affect the distribution of observed stars along the line of sight, and therefore the distance range over which the map is reliable. Sharp transitions in reliable distance occur at pixel size boundaries, where the number of stars per pixel changes discontinuously, as well as in patches of the sky with missing PS1 passbands.

scale, but also by the distribution of stars throughout the Galaxy, the 3D distribution of dust and the survey depth. The survey depth plays a larger role in the far limit because the most distant observed stars lie preferentially near the limiting survey magnitude. The closest stars, by contrast, are distributed more evenly in apparent magnitude. Accordingly, the high-latitude patches with particularly shallow maximum reliable distances (e.g., the shallow patch near $\ell = 205°, b = -55°$) correspond to areas which are missing one or more PS1 bands, or which have fewer observation epochs in the PS1 $3\pi$ survey, and therefore worse coverage.

As a check on these estimated nearest and farthest reliable distance maps, we construct equivalent maps using simulated stellar catalogs. For each pixel in our map, we use our Galactic priors and the estimated limiting magnitudes for $grizy_{\mathrm{P1}}$ and 2MASS $JHK_s$ to generate an equal number of stars as actually observed. We then determine the distance in front of which there are $N_{\mathrm{closer}}$ and beyond which there are $N_{\mathrm{farther}}$ main-sequence stars. In order to remove the complicating factor of the line-of-sight dust inference, we restrict this test to $|b| > 15°$ and to pixels for which $\mathrm{E}(B-V)_{\tau_{353}} < 0.05$ mag, and assume for our simulated catalogs that there is zero dust extinction. In these comparisons, we find that a halo number density close to the value given in Jurić *et al.* (2008) is required to reproduce inferred map depths of Fig. 4.5. The results for a halo strength of $n_h = 0.004$, binned down to `nside` $= 64$, are shown in the right two panels of Fig. 4.5.

These results indicate that while we dialed down the halo strength in our priors, the data, as reflected in our photometric stellar inferences, nonetheless prefers a stronger halo. In future work, we will investigate the implications of our stellar and line-of-sight dust inferences for a global Galactic structure model.

### 4.1.2 Individual Stellar Reddenings

In order to test the accuracy of our reddening inferences for individual stars, we compare our photometric reddenings to independently measured reddenings for a sample of stars. For this, we use the set of stellar reddening standards developed by Schlafly & Finkbeiner (2011). The Sloan Extension for Galactic Understanding and Exploration (SEGUE; Yanny *et al.* 2009) obtained moderate-resolution spectroscopy for 240,000 stars with SDSS photometry. Whereas most of the SDSS footprint is at low reddening, some of the SEGUE targets are at moderate reddening, up to $\sim$1 mag in E($B-V$). The SEGUE Stellar Parameter Pipeline (SSPP) fits an atmospheric model to each star to derive the temperature, metallicity, and gravity of the star, as well as other parameters (Lee *et al.* 2008a,b; Allende Prieto *et al.* 2008). These stellar parameters were used by Schlafly & Finkbeiner (2011) to predict the intrinsic colors of stars, and to study the effect of reddening by attributing the differences between the observed and intrinsic colors to dust. Empirically adjusted SDSS colors based on model atmospheres can then be compared with observed SDSS photometry to obtain reliable reddening estimates. We select the same sample of 200,000 SEGUE target stars as Schlafly & Finkbeiner (2011), which excludes white dwarfs and M dwarfs (the former because they are not contained in our model, and the latter because of their unreliable spectral classification).

We estimate the reddening of each selected SEGUE target star in a manner similar to that of Schlafly & Finkbeiner (2011), based on a comparison of the predicted and observed data in the four SDSS colors, assuming a Fitzpatrick (1999) reddening vector with $R_V = 3.1$. The details of how one derives reddening from on SEGUE-determined intrinsic colors and observed SDSS colors are

described in § A.4.

As described in § 1.7, after generating our 3D dust map, we reweight the naively inferred parameters for each star in order to take the line-of-sight reddening profile into account. In order to demonstrate the improvement in stellar inferences after this reweigthing procedure, we compare the SEGUE standards to our stellar reddening inferences, both with and without the 3D-dust-informed reweighting.

Fig. 4.6 therefore compares reddening inferences from our PS1+2MASS-based stellar inferences to the SEGUE-based estimates. We bin the stars by the reddening expected from the dust maps of Schlegel *et al.* (1998, SFD), and plot a histogram of the difference in the two reddening measures in each bin. We place the SFD reddening on the $x$-axis because it is a good proxy for reddening and is independent of both of the two reddening estimates we wish to compare. Placing either the SEGUE-derived reddening or the Bayesian reddening along the $x$-axis would introduce spurious trends in the resulting comparison. We draw multiple samples for each star, from the samples stored for our PS1+2MASS-based reddenings and the Gaussian uncertainties in the SEGUE reddenings. The top panel of Fig. 4.6 conducts this comparison with unweighted samples, while the bottom panel conducts the comparison using the reweighting scheme introduced in § 1.7.

The agreement with SEGUE reddening estimates improves significantly after reweighting our PS1+2MASS-based stellar inferences, as can be seen from comparison of the upper and lower panels of the figure. The improvement is most pronounced at low reddenings. This is likely due to the fact that we do not allow negative stellar reddenings when deriving the 3D dust map, while the SEGUE-based estimates have no hard bound that $\mathrm{E}(B-V) \geq 0$. For the unweighted PS1+2MASS-based

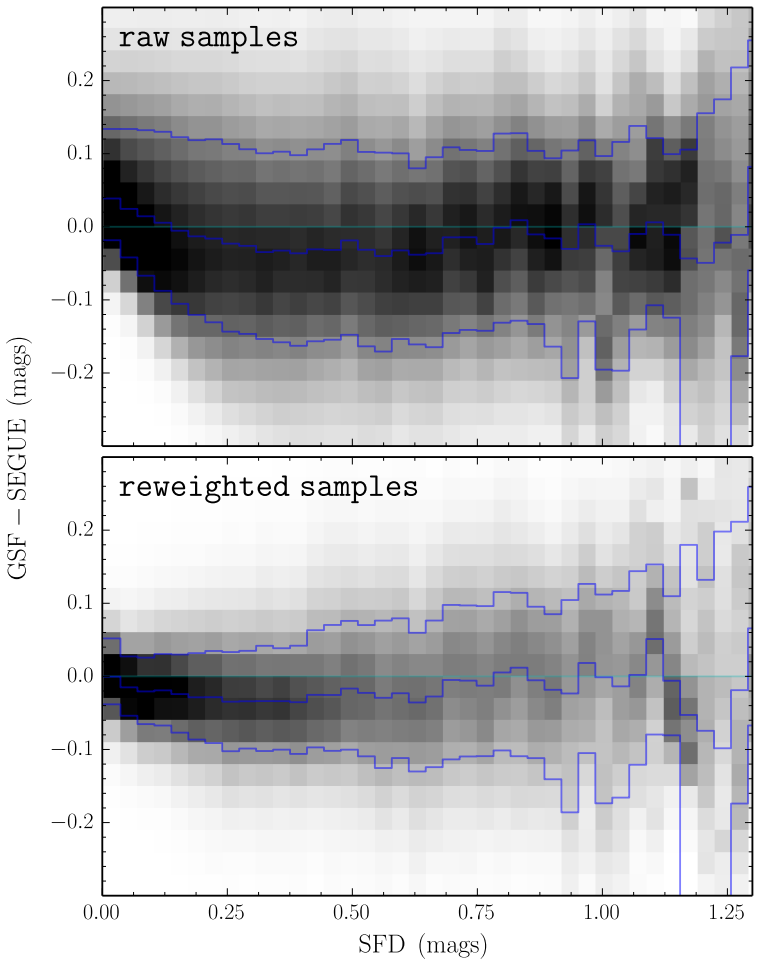


Figure 4.6: Histograms of the residuals of our PS1+2MASS-based stellar reddenings (referred to as "GSF" here), versus reddening estimates obtained by comparing SEGUE spectral classifications with SDSS photometry. The histograms are spread out along the $x$-axis by the local SFD reddening. The blue lines trace the 16th, 50th and 84th percentiles of the residuals in each bin of SFD reddening. In the upper panel, we use unweighted samples drawn from the individual stellar parameter Markov Chains. In the lower panel, we use reweighted samples, as described in the text (See §§ 1.7 and 4.1.2).

reddening samples, the non-negativity constraint causes a negative slope vs. the SEGUE reddening measurements at low reddening. The improvement from reweighting the samples is negligible for $E(B-V) \gtrsim 1$ mag, due to the fact that we allow the individual stars to deviate from the local line-of-sight reddening profile by about 10%. The scatter between the unweighted samples and SEGUE reddening estimates is approximately 0.15 mag in $E(B-V)$, with the overall estimate being unbiased to within 0.03 mag. This result is indicative of the accuracy we achieve for high-signal-to-noise detections, as most SEGUE targets are well above the detection limit in PS1.

## 4.2 Comparison with Previous Dust Maps

Schlafly *et al.* (2014a) compares an earlier version of our 3D dust map with the two-dimensional, far-infrared emission-based SFD (Schlegel *et al.* 1998) and *Planck* dust maps (Planck Collaboration 2014). Here, I repeat this comparison using the newer 3D dust map described in this thesis, and additionally compare our dust map with previous 3D dust maps, which are also based on stellar photometry.

### 4.2.1 2D Dust Maps

It is possible to obtain a 2D dust map from our 3D map by projecting out distance, i.e., by taking the cumulative reddening out to some large distance. Such a map is of particular interest for extragalactic astronomy, where Milky Way dust is essentially a foreground screen to be removed. As discussed in § 0.3, several all-sky 2D maps of dust reddening already exist, among them Burstein & Heiles (1982), based on HI emission and galaxy number counts, Schlegel *et al.* (SFD; 1998) and two recent

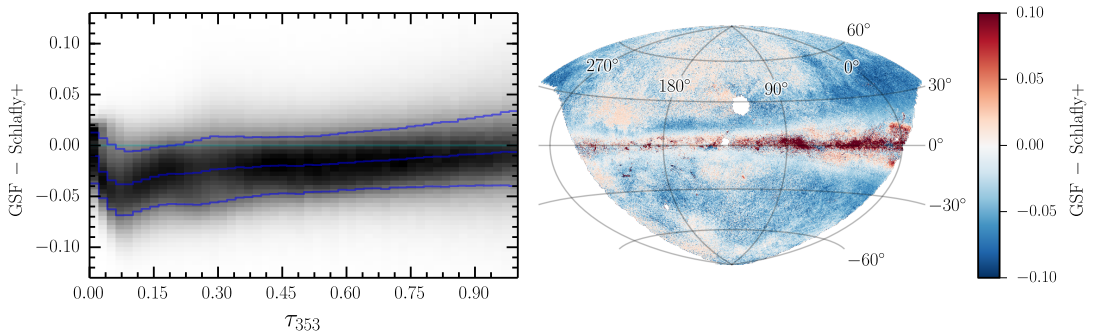


Figure 4.7: A comparison of our new 3D dust map ("GSF"), integrated to 4.5 kpc, with the 2D map presented in Schlafly *et al.* (2014a). The left panel shows the difference between our map and Schlafly *et al.* (2014a) as a function of a third reddening measure with uncorrelated errors, the *Planck* $\tau_{353\,\mathrm{GHz}}$-based dust reddening map. The right panel maps the median residuals between our map and Schlafly *et al.* (2014a) across the sky. All units are in magnitudes of E($B-V$).

reddening maps derived from *Planck* data (Planck Collaboration 2014), which model dust optical depth and temperature from far infrared emission, and then calibrate a dust optical depth to reddening relation. Near-infrared stellar colors have also been used to determine dust reddening more directly, as in the NICE/NICER/NICEST family of algorithms (Lada *et al.* 1994; Lombardi & Alves 2001; Lombardi 2009, respectively) discussed earlier, and Rowles & Froebrich (2009).

Schlafly *et al.* (2014a) compares a 2D projection of an earlier version of our 3D dust map with the widely used SFD reddening map, as well as the newer *Planck* reddening maps. We repeat a number of the same tests for our new 3D dust map.

We begin, however, with a comparison between the map presented in this thesis and the map presented in Schlafly *et al.* (2014a). The most important differences between the 3D maps used here and in Schlafly *et al.* (2014a) are addition of near-infrared 2MASS photometry in our newer map, and that we sample here from the full posterior distribution on line-of-sight reddening, rather than

finding the maximum-likelihood line-of-sight reddening. Because Schlafly *et al.* (2014a) requires that each star be detected in $g_{\rm P1}$, and because we incorporate near-infrared 2MASS photometry alongside PS1 photometry, our map reaches to deeper dust extinctions. This is apparent in the right panel of Fig. 4.7, where our new map predicts more reddening both in the inner Galactic plane and in dense dust clouds off the plane, such as Orion, Taurus and Perseus.

At reddenings below $\mathrm{E}(B-V) \lesssim 0.08$ mag, our new map predicts significantly less reddening than Schlafly *et al.* (2014a), as can be seen in the left panel of Fig. 4.7. Beyond $\mathrm{E}(B-V) \approx 0.1$ mag, our reddening scales agree very closely, with our new map predicting $\sim 4\%$ more reddening. The scatter between the two reddening measures comes to $\sim 0.04$ mag, with a maximum median offset of 0.04 mag at $\mathrm{E}(B-V) \approx 0.08$ mag, decreasing gradually to an offset of less than 0.01 mag between the two measures at $\mathrm{E}(B-V) = 1$ mag. The behavior of the residuals suggests that at very low reddenings, our new 3D dust map prefers essentially zero reddenings too strongly. This may be due to the stronger priors on dust reddening used in the present work, or due to slight differences in our new combined PS1-2MASS stellar locus, versus the PS1 stellar locus used in Schlafly *et al.* (2014a).

Next, we compare our inferred cumulative reddening out to 5 kpc with the SFD map, the *Planck* $\tau_{353\,\mathrm{GHz}}$-based reddening (hereafter, denoted simply as $\tau_{353}$, with units of magnitudes of $\mathrm{E}(B-V)$), and the *Planck* radiance-based map (hereafter denoted $\mathcal{R}$, likewise with units of magnitudes of $\mathrm{E}(B-V)$). All three of these maps are derived by modeling dust emission, and should therefore have different types of systematic errors than our stellar reddening-based dust map.

The upper panel of Fig. 4.8 shows the SFD reddening across the footprint of our map, while

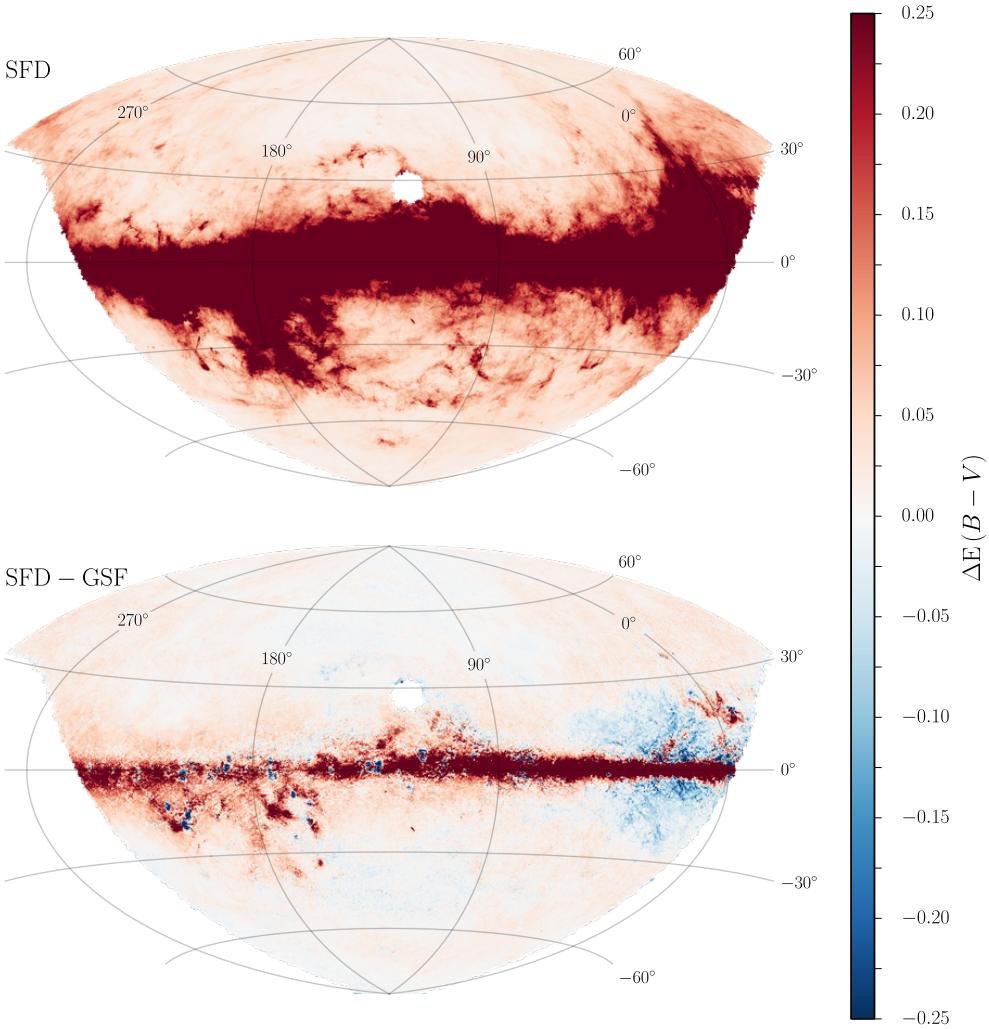


Figure 4.8: A comparison of the 2D SFD reddening map with our PS1-based map ("GSF"), integrated out to 5 kpc. The top panel shows the SFD reddening over the footprint of the PS1 survey, clipped to 0.25 mag, while the bottom panel shows the residuals after subtracting off the median cumulative reddening out to 5 kpc predicted by our 3D dust map. Both panels use the same color scale, and the units are magnitudes.

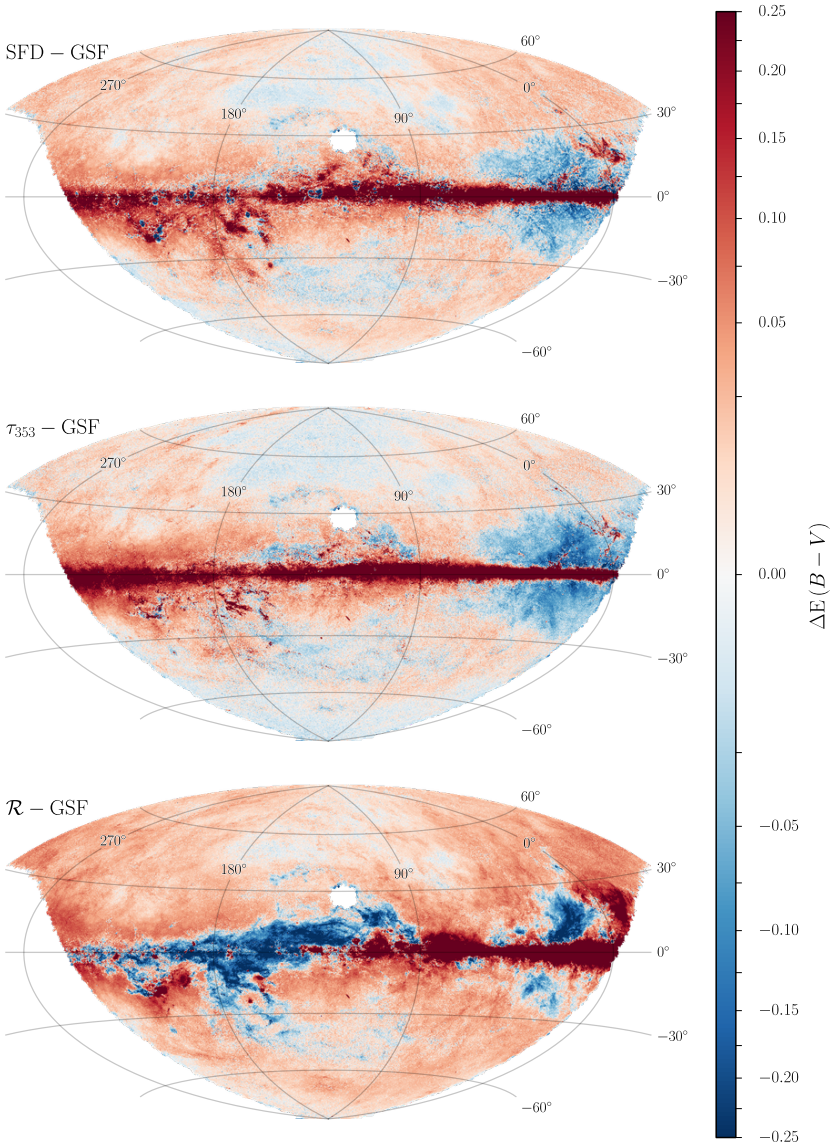


Figure 4.9: A comparison of our PS1-based reddening to 5 kpc (denoted by "GSF") with SFD, the *Planck* $\tau_{353\,\mathrm{GHz}}$-based reddening, and the *Planck* radiance-based map (denoted by $\mathcal{R}$). Each panel shows the residuals between one of the three emission-based dust maps and the median integrated reddening in our map on a square-root stretch. The units are magnitudes of $\mathrm{E}(B-V)$. Out of the plane of the Galaxy, we agree well with the emission-based maps. Deep in the plane of the Galaxy, where extinction and stellar crowding prevent us from observing stars beyond all of the dust, our 3D dust map traces less total extinction than the emission-based maps. Milky Way dust is optically thin in emission, whereas it is optically thick in optical/NIR extinction, so the fact that emission-based maps trace dust out to greater distances should not be surprising.

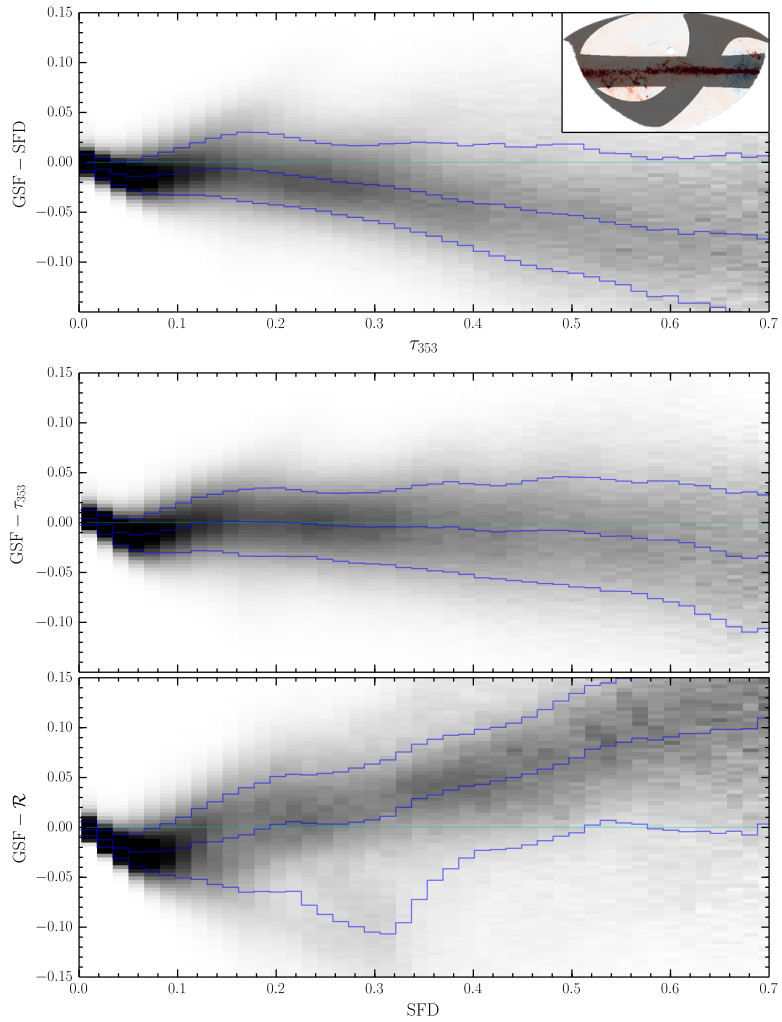


Figure 4.10: A comparison of our PS1-based reddening to 5 kpc (denoted by "GSF") with SFD, the *Planck* $\tau_{353\,\mathrm{GHz}}$-based reddening, and the *Planck* radiance-based map (denoted by $\mathcal{R}$). Each panel shows histograms of the residuals between one of the emission-based maps and posterior samples drawn from our map. Instead of showing a single histogram in each panel, we divide up the sky according to $\mathrm{E}(B-V)$, and produce a histogram for each $\mathrm{E}(B-V)$ bin. Each histogram is shown at a different location along the $x$-axis, according to the $\mathrm{E}(B-V)$ bin it was computed in. In the upper panel, we put the $\tau_{353\,\mathrm{GHz}}$-based reddening estimate, in magnitudes, along the $x$-axis, since its errors should be largely uncorrelated with the errors in the PS1 and SFD reddening estimates. In the bottom two panels, we use the SFD reddening estimate, in units of magnitudes, as our proxy for reddening, likewise because its errors should be uncorrelated with those of the quantities along the $y$-axis. An inset in the top-right panel shows the regions that are masked in this analysis. The detailed behavior of the residuals, particularly at large reddenings, depends on which regions are masked, indicating that there are systematic differences in the residuals between our reddening map and emission-based map in different regions of the sky.

the lower panel shows the residuals after subtracting off our 5 kpc map. Off the Galactic plane, the residuals are small, while larger residuals are found in the plane of the Galaxy, where there is significant dust past 5 kpc, and where PS1 does not necessarily detect stars beyond all of the dust. Near the Galactic center, but several degrees off the plane of the Galaxy, one noticeable feature is a blue halo, where we infer more dust than SFD. The residuals are correlated with dust reddening in this area, indicating a scale offset between the two maps, rather than a constant offset.

The "blue halo" is again apparent if we compare our map to the the *Planck* $\tau_{353}$ map. In Figs. 4.9 and 4.10, we compare our inferred reddening at 5 kpc with SFD, $\tau_{353}$, and $\mathcal{R}$. Fig. 4.9 map the residuals across the PS1 survey footprint on a square-root stretch, emphasizing small-amplitude differences. In Fig. 4.9, the *Planck*-based maps have been scaled by a constant factor to match our inferred PS1 reddening for $|b| > 20°$.

As the "blue halo" occurs in the direction of the nearby Aquila Rift, it is possible that the cloud has anomalous dust properties. For example, the grain size distribution or composition may vary, so that $R_V = 3.1$ is not a good assumption in the Aquila Rift. Another possible explanation for the "blue halo" is that our stellar inferences may be systematically biased towards greater reddenings in this direction due to limitations in our Galactic model. Our priors do not, for example, include a radial metallicity gradient in the disk components of the Galaxy, which could lead to biased metallicity estimates for stars towards the Galactic center. We leave this question for future investigation.

In Fig. 4.10, we plot the residuals of our inferred reddening to 5 kpc with SFD and the *Planck* emission-based maps as a function of reddening. Here, we do not scale the *Planck* maps by any factor to bring them into alignment with our map. To conduct this comparison, we compare the

emission-based maps to multiple random realizations drawn from the posterior on reddening to 5 kpc from our 3D dust map. We restrict our comparison to high-Galactic-latitude regions ($|b| > 30°$), and cut out the ecliptic plane ($|\beta| < 20°$), where imperfectly subtracted Zodiacal light might contaminate the emission-based reddening maps. When comparing our PS1-based reddening with SFD, we place the *Planck* $\tau_{353\,\mathrm{GHz}}$-based reddening on the $x$-axis, as its errors are uncorrelated with both maps on the $y$-axis. When displaying the residuals between our PS1-based reddening and the *Planck* reddening maps, we place SFD along the $x$-axis for the same reason.

For reddenings above $\mathrm{E}(B-V) \gtrsim 0.05$ mag, we see broadly similar residuals as found in Schlafly *et al.* (2014a), with with different behaviors above and below $\mathrm{E}(B-V) \approx 0.15$ mag. Above $\mathrm{E}(B-V) \approx 0.15$ mag, our map predicts about 10% less reddening than SFD, but is in good agreement with $\tau_{353}$. As in Schlafly *et al.* (2014a), we find an overall difference in scale between our PS1-based map and the *Planck* $\mathcal{R}$-based map. For $\mathrm{E}(B-V) \lesssim 0.05$ mag, we see the same residual between our map and the emission-based maps as found between our map and Schlafly *et al.* (2014a). For these small reddenings, our map favors essentially zero reddening too heavily.

The exact behavior of the residuals depends on which regions of the sky are masked in the analysis, indicating that there are spatially-dependent systematic differences in the residuals between our reddening map and emission-based maps. However, the essential features remain the same, with different slopes in the residuals below and above $\mathrm{E}(B-V) \approx 0.15$ mag, and our map favoring lower reddening below $\mathrm{E}(B-V) \approx 0.05$ mag.

A striking difference between our 3D dust map and SFD is the prominence of fine filamentary structure in the former. An example of this difference is shown in Figs. 4.11 and 4.12, which com-

pares the 3D map, integrated to 8 kpc, with SFD. Although SFD nominally has a similar angular resolution (6.1′) as our 3D dust map, our map often appears sharper. This is likely due to the resolution of the SFD correction, which at 0.8° is much coarser than the 100 $\mu$m IRAS map that SFD uses to trace dust emission. If fine filaments in the interstellar medium are colder than their surroundings, the SFD temperature map will overestimate their temperature. Since hotter dust emits more strongly per unit column density than cold dust, SFD will therefore underestimate the column density of regions where the temperature has been overestimated. In regions where the temperature of the interstellar medium varies on small angular scales, the SFD temperature map therefore has the effect of smoothing out fine features, such as cold filaments and the cores of dense clouds. This conclusion is bolstered by the fact that the *Planck* $\tau_{353}$-based reddening map, which does not suffer from a low-resolution temperature correction, shows the same filamentary features as our 3D dust map.

### 4.2.2 Marshall et al. (2006)

Marshall *et al.* (2006) developed a method to determine the reddening-distance relation along individual lines of sight by comparing 2MASS $J - K_s$ stellar colors to those of simulated catalogs based on the Besançon model of the Galaxy (Robin *et al.* 2003). Marshall *et al.* (2006) then applied this method to a regular grid of sightlines separated, by 15′ covering the region $|\ell| < 100°$, $|b| < 10°$. The result is a 3D map of reddening in the inner Galaxy, extending to a maximum extinction of $\sim 1.4 - 3.75$ mag in the 2MASS $K_s$ band (equivalent to $\sim 4.5 - 12$ mag in $E(B-V)$), and a maximum distance of $\sim 7$ kpc. Because Marshall *et al.* (2006) use only giants in their analysis, the dust map they produce has little information in the nearest kiloparsec. We will refer to this map as the

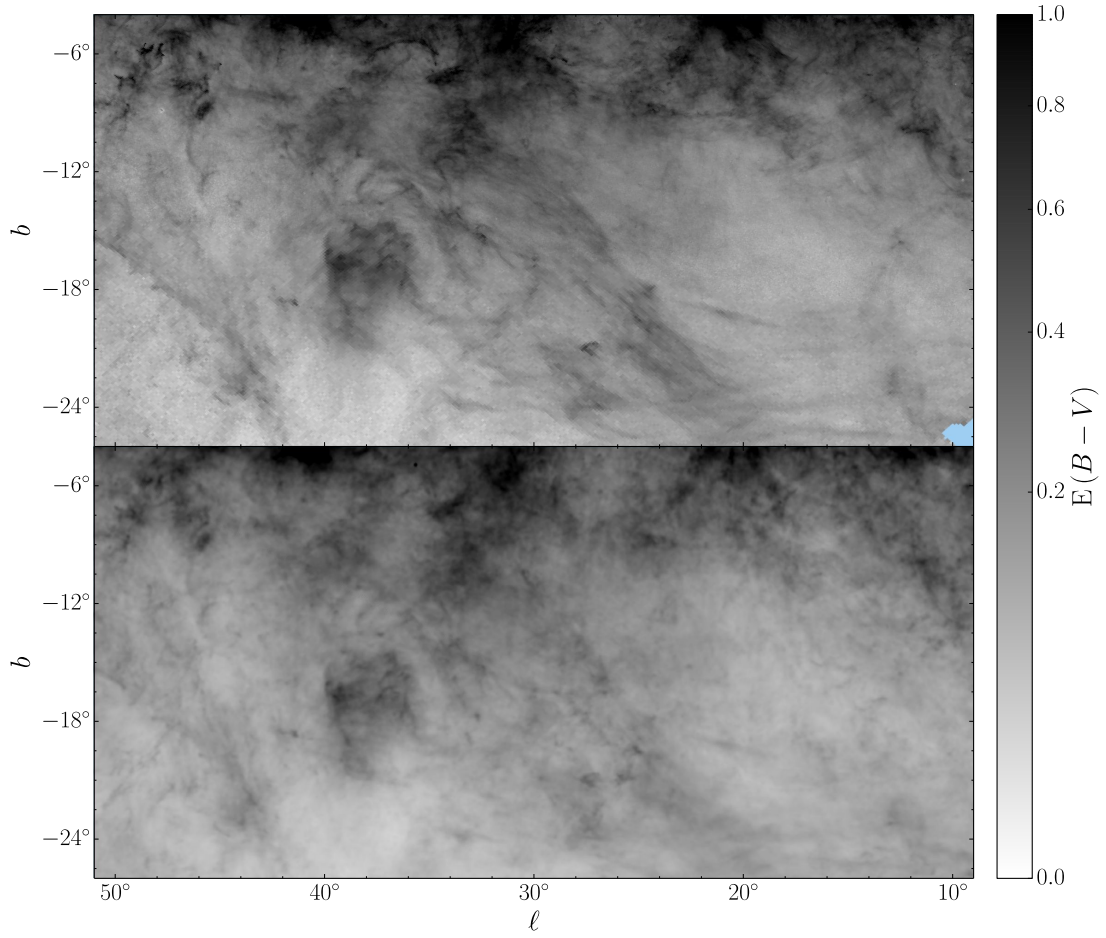


Figure 4.11: Reddening in the Aquila South region, showing fine filamentary structure in our 3D map (top panel) which is missing in SFD (bottom panel). The top panel shows median cumulative reddening to 8 kpc from the 3D map, while the bottom panel shows SFD reddening. The maps are shown with a square-root stretch, with units of magnitude. Although both maps have similar nominal angular resolution, SFD relies on a relatively low-resolution temperature correction, which may cause cold filamentary structures to be blurred out.

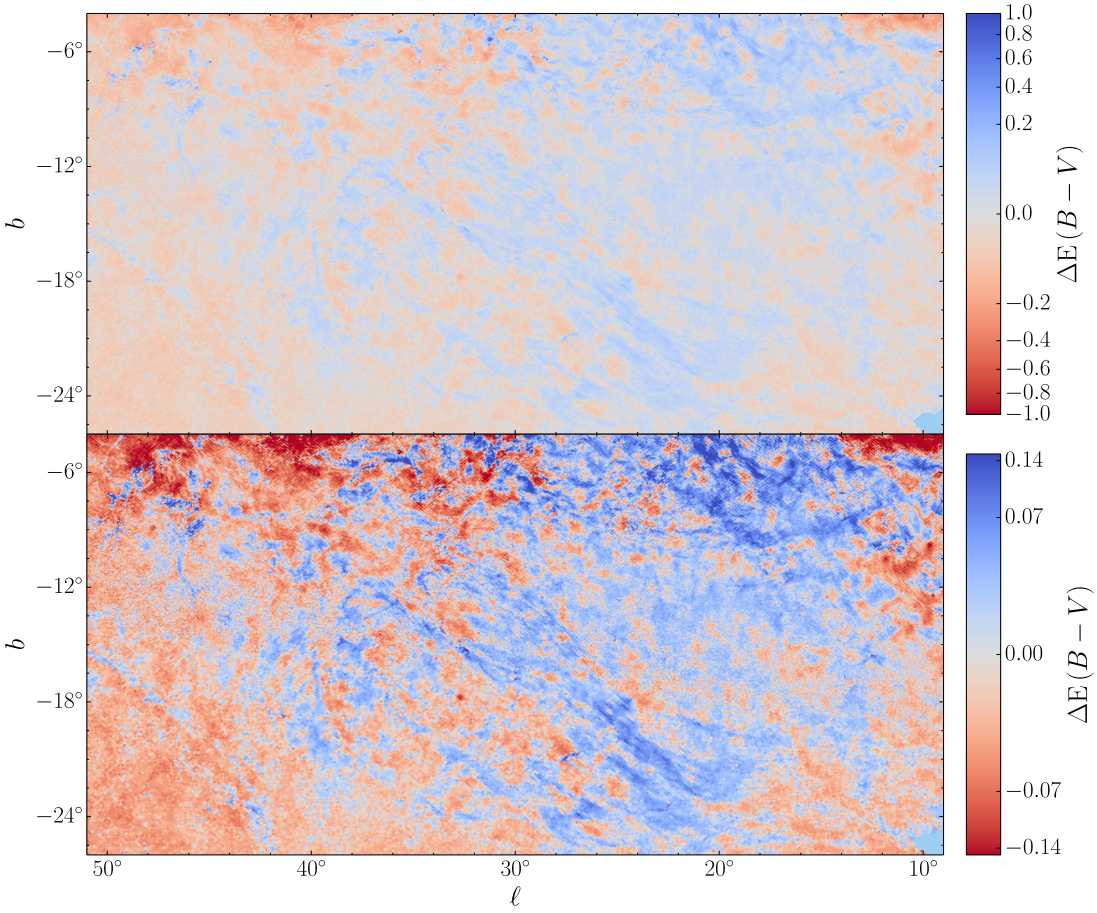


Figure 4.12: Reddening residuals in the Aquila South region between the median integrated reddening (to 8 kpc) in our 3D dust map and SFD. Positive values (blue) indicate that our 3D dust map infers more reddening. Before the residuals are taken, the median scale difference between the two maps has been divided out. In detail, the reddening of the 3D dust map has been multiplied by a uniform factor of 0.86. Both panels show the residuals on a square-root color stretch, which emphasizes small residuals. The bottom panel uses a narrower scale, and thus shows small residuals more clearly. While most of the recognizable structure from Fig. 4.11 cancels out (e.g., the cloud at $\ell \approx 38°$, $b \approx -18°$), filamentary structure remains. As discussed in the text, this is likely due to the SFD temperature map blurring out small-scale features in the map.

"Marshall map."

Our dust map overlaps with the Marshall map in the approximate region $0^\circ < \ell < 100^\circ$, $|b| < 10^\circ$. Fig. 4.13 shows the cumulative reddening at increasing distances in both the Marshall map and our 3D dust map. When converting from extinction to reddening, we assume $A_{Ks} = 0.320\,\mathrm{E}(B-V)$, as calculated by Yuan *et al.* (2013) for a 7000 K source spectrum at $\mathrm{E}(B-V) = 0.4$ mag, using the Cardelli *et al.* (1989) reddening law and assuming $R_V = 3.1$. We mask our map beyond our predicted maximum reliable distance, as determined in § 4.1.1. In the large-distance limit, our maps show good qualitative agreement outside of the masked areas. Fig. 4.14 shows the differential reddening in the two maps in bins of increasing distance.

In the nearest two to three kiloparsecs, our map shows clearly differentiated structures at discrete distances that are spread over several distance bins in the Marshall dust map. For example, the Cygnus rift (located at $\ell \sim 80^\circ$, $b \sim 0^\circ$) appears clearly in our map in the distance bin spanning $0.5 - 1$ kpc, while in the Marshall map, it is spread over all the distance bins closer than $\sim 3$ kpc, and is therefore not cleanly separated from superimposed dust structures at greater distances. The greater distance resolution of our map at nearby distances is most likely due to the fact that we use both main-sequence stars and giants, while Marshall *et al.* (2006) relies solely on giants, which are saturated nearby and form a larger fraction of the observable stellar population at greater distances.

In addition to better distance resolution in the first few kiloparsecs, the greater source density of PS1 relative to 2MASS allows us to achieve better angular resolution than the Marshall map. Fig. 4.15 demonstrates the difference in angular resolution between the two maps. In most of the region of overlap between our reddening map and the Marshall map, we achieve an angular resolution of $3.4'$,

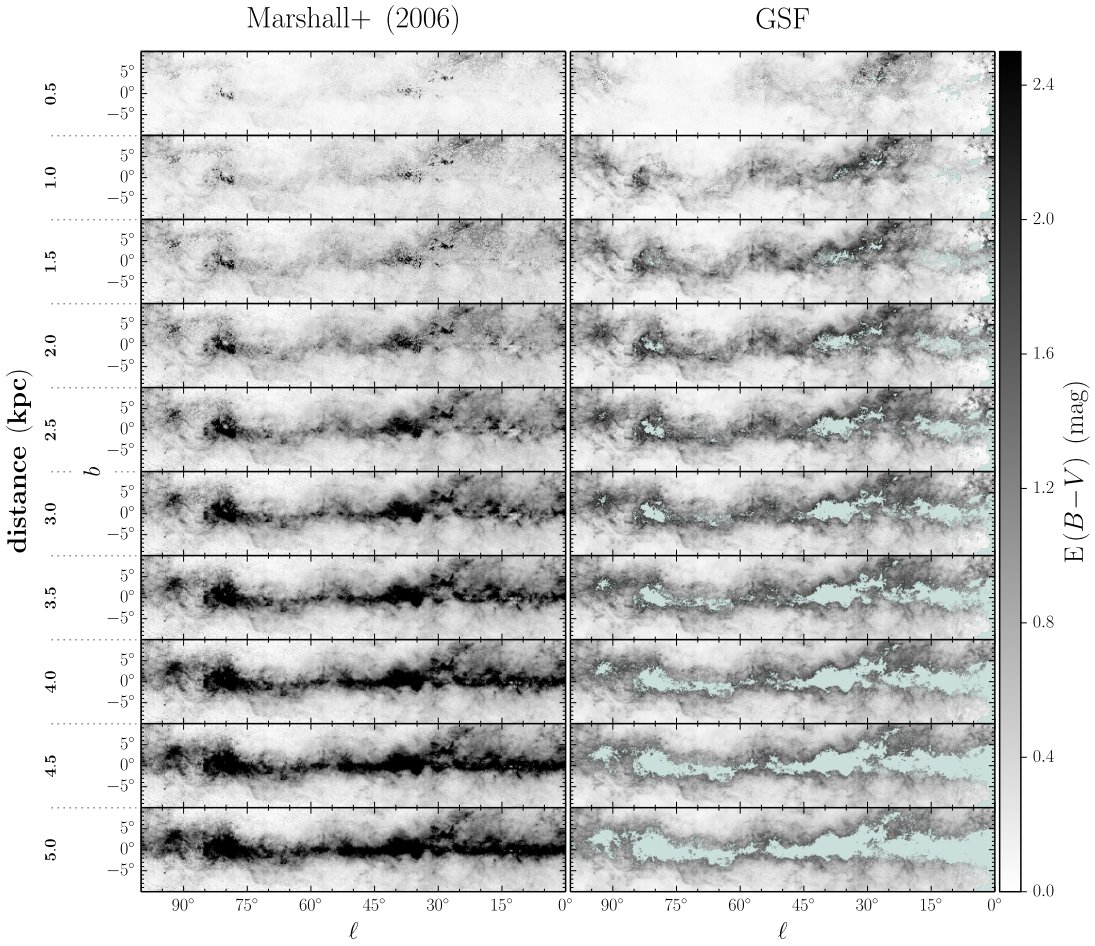


Figure 4.13: A comparison of the median cumulative reddening out to increasing distances in the Marshall map (left panel) and our map (right panel). Regions beyond the maximum reliable distance in our map are masked out in blue in the right panel. At large distances, the two maps agree qualitatively, with the masked regions in our map corresponding to the most heavily obscured regions in the Marshall *et al.* (2006) map. The Marshall map has greater depth, but lower angular resolution, and lower distance resolution in the nearest two to three kiloparsecs.

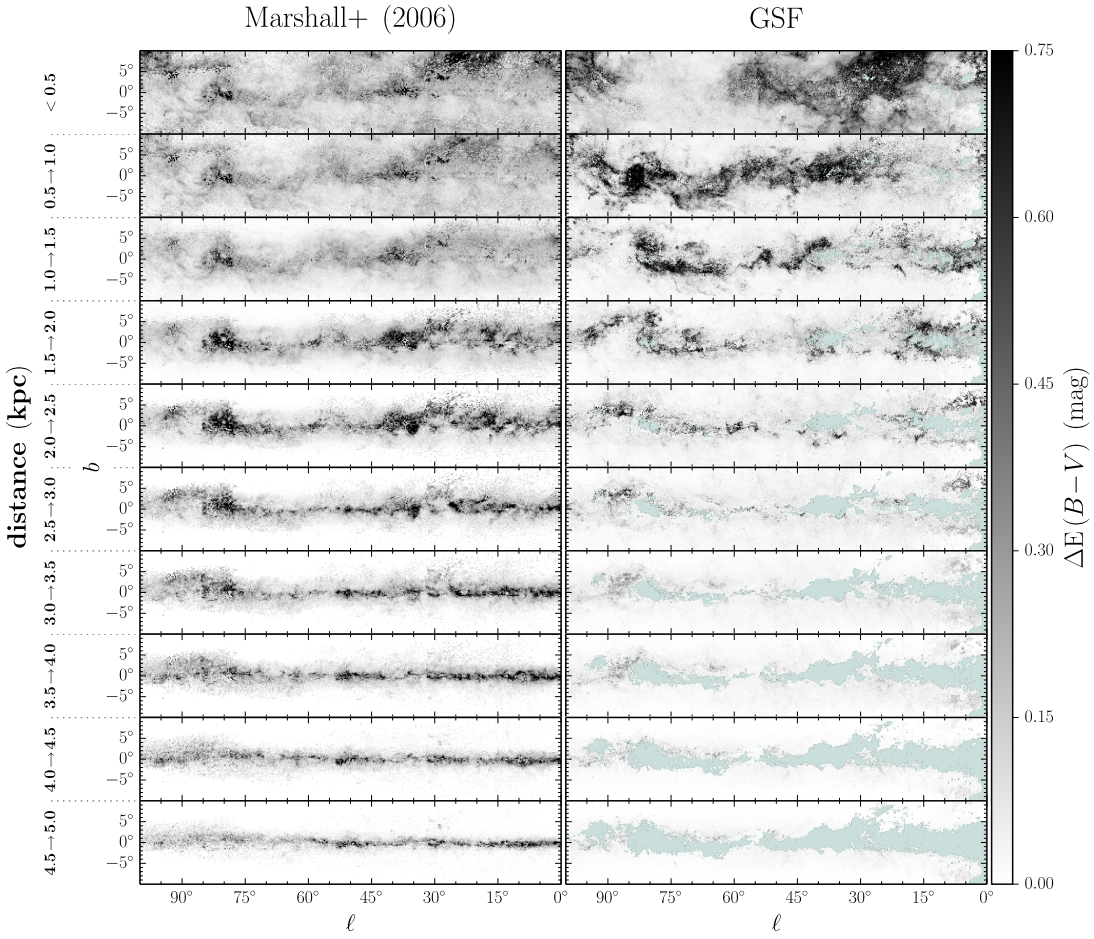


Figure 4.14: A comparison of the median differential reddening in bins of increasing distance in the Marshall map (left panel) and our map (right panel). In the nearest two to three kiloparsecs, we achieve much better distance resolution, as evidenced by the differentiated structures visible in successive distance bins.

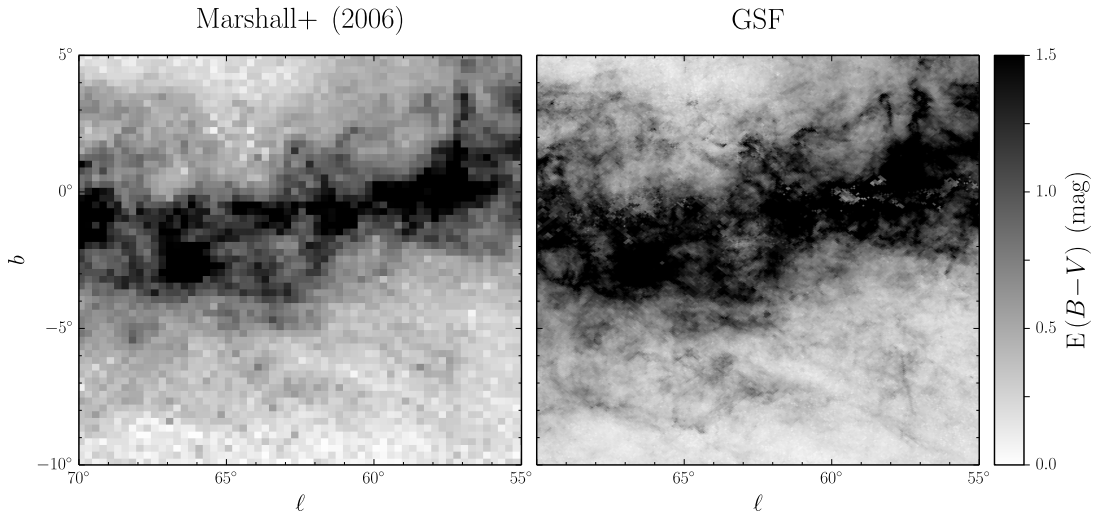


Figure 4.15: A zoom-in of median cumulative reddening to 3 kpc, showing the difference in angular resolution between the Marshall 3D reddening map (left panel) and our map (right panel), as well as the lower noise of the latter. The Marshall dust map has an anuglar resolution of 15′, while our dust map has a typical angular resolution of 3.4′ in the region of the Galactic plane displayed above. The reliability mask has not been applied our map in this figure.

as opposed to the constant 15′ resolution of the Marshall map. This allows us to resolve detailed filamentary structure not seen in the latter map. As dust reddening can vary significantly on small angular scales, this increased angular resolution will be important in practice for correctly de-reddening extinguished sources in regions with complex dust structure.

Deep in the plane of the Galaxy, where high extinction reduces source counts, our finer angular resolution limits the distance to which our map can trace dust, compared to the Marshall map. Although the PS1 3$\pi$ survey is deeper than 2MASS, the 2MASS passbands are less affected by dust extinction, and the advantage of PS1 decreases in regions of high extinction. In such regions, the greater depth of PS1 does not fully compensate for our smaller pixels, limiting the depth to which we trace dust deep in the Galactic plane. The fact that our map derives its most accurate reddening

information from main-sequence stars also limits the maximum extinction to which it is reliable.

### 4.2.3 Lallement et al. (2013)

Combining distance and reddening estimates for $\sim$23, 000 stars with the assumption of spatial correlation in dust density, Lallement *et al.* (2014) infer reddening in 3D out to a distance of $\sim$800 pc from the Sun. We find close morphological agreement between our 3D dust map and that of Lallement *et al.* (2014), with some differences which are worth taking note of.

In Fig. 4.16, we show the distribution of dust and stars in a slice 25 pc above the Galactic plane, level with the Sun. We show the median dust density. In order to generate the stellar locations, we draw a sample at random from the improved distance posterior of each star (See § 1.7), and select only those stars that lie within 5pc of the chosen plane. For display purposes, we only display one out of every thousand stars.

Just as Lallement *et al.* (2014), we find cavities in the dust density in the directions of $\ell = 70^\circ$ and $225^\circ$. The overall morphology of the dust structure in the right panel of Fig. 4.16 matches that of Fig. 1 in Lallement *et al.* (2014).

The most obvious difference between our maps and those of Lallement *et al.* (2014) is the different voxel shapes employed in our work and theirs. Lallement *et al.* (2014) use small cubic voxels, and assume a spatial correlation function that favors similar dust densities in nearby voxels. This allows them to densely sample the reddening distribution, with voxels that are not directly constrained by stellar reddening measurements being constrained by neighboring voxels. In contrast, we infer the dust distribution in each line of sight separately, without assuming spatial correlations in the dust

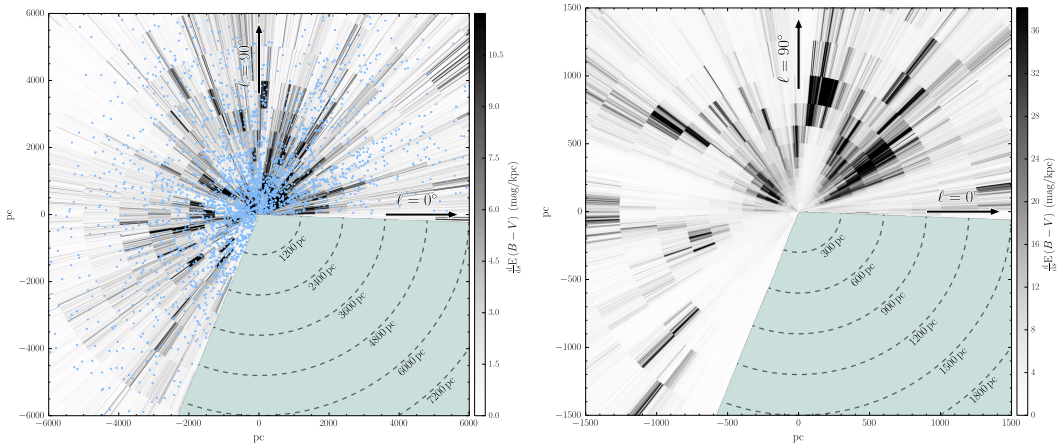


Figure 4.16: Dust density in a 10pc-thick slice lying 25 pc above the Galactic plane (i.e., level with the Sun), with positions of stars within this slice overplotted in the left panel. In detail, we show the median (over multiple realizations of the 3D dust map) of the reddening column density along each sightline passing through the slice (i.e., into the page). The Sun is at the origin of each panel, with the right panel being a zoomed-in version of the left (without the overplotted stars). Only every 1000th star has been plotted. The dust map is reliable out to distances at which the stellar density becomes too small to trace the dust column. Compare with Fig. C2 of Lallement *et al.* (2014), in which the stellar density is concentrated within $\sim$200 pc of the Sun.

density, as laid out in § 1.1. While our map has excellent angular resolution, it has distance bins with a width of about 25%, giving our voxels their pencil-beam shape.

Although we see roughly the same structures, such as cavities in the reddening distribution centered on $\ell = 70°$ and 225°, the distances we derive for a number of clouds is greater than the distances Lallement *et al.* (2014) find. In particular, while Lallement *et al.* (2014) place the Cygnus rift between 500 and 600 pc, we place it at a distance of 800 to 1000 pc.

## 4.3 Accessing the Map

Our 3D dust map can be accessed at `http://argonaut.skymaps.info`. The website provides an interface for querying individual lines of sight, as well as the ability to download the entire map

and software to read it. We also provide an API through the website, which allows users to query the map remotely with a few lines of code, without the need to download the entire data cube. The data is also accessible at http://dx.doi.org/10.7910/DVN/40C44C, through the Harvard Dataverse.

### 4.3.1 Data Cube

The basic data product our map contains is samples of the differential reddening in 31 distance bins, in each of 2.4 million pixels. The data structure is thus

$$\left(2.4 \times 10^6 \text{ pixels}\right) \times (500 \text{ samples}) \times (31 \text{ distance bins}) \ .$$

This allows us to determine the probability density of the cumulative reddening to any distance (within a few kiloparsecs) in the $3\pi$ steradians covered by the PS1 survey.

We encourage users to use the Markov chain samples of reddening versus distance provided by our interface in their analyses, as the samples contain the full statistical information generated by our method. These samples can be queried using our web API, downloaded as an ASCII table for individual lines of sight, or accessed directly in the complete data cube provided for download.

An additional, and larger, dataset that we produce while generating the 3D dust map is a library of photometrically determined stellar parameters. As described in §§ 1.1 and 1.5, we infer the probability distribution of distance modulus, reddening, metallicity and absolute $r_{\mathrm{P1}}$-magnitude for each

star. We thus have a second data cube with shape

$$\left(8 \times 10^8 \text{ stars}\right) \times (100 \text{ samples}) \times (4 \text{ parameters}) \ .$$

In addition, we store quality assurance information for each star, including whether the Markov Chain converged during the fitting procedure, and the Bayesian evidence for the stellar model, which is similar to the $\chi^2$ statistic in maximum-likelihood fitting. Point sources with poor evidence are likely either of stellar types not contained in our model, such as very young stars or binary systems, or are not stars (e.g., white dwarfs, quasars, unresolved galaxies).

# 5

# Conclusion

This thesis has presented a general method for deriving a three-dimensional map of Galactic reddening from stellar photometry. This technique is based on grouping stars into pixels, determining the joint posterior of distance and reddening for each star, and then inferring the distance–reddening relation in each pixel. I have applied this method to ∼800 million stars with high-quality multiband photometry in Pan-STARRS 1, using

matched 2MASS photometry for $\sim$200 million stars, obtaining a three-dimensional map of dust reddening covering the three quarters of the sky at declinations of $\delta > -30^\circ$. This map provides a window into the structure of the interstellar medium, revealing detailed structure from the smallest scales in the map, $3.4'$, all the way to large cloud complexes spanning many degrees. I provide interfaces to query and download the map at `http://argonaut.skymaps.info`.

Projecting the map down to two dimensions, I find good agreement with emission-based dust maps at high Galactic latitudes, where one would expect our method to trace the entire dust column. Comparison with the 3D map of nearby dust presented in Lallement *et al.* (2014) shows the same morphological features. In comparison with the 3D dust map of the inner Galactic plane presented in Marshall *et al.* (2006), the map developed in this thesis has greater angular resolution and superior distance resolution within $\sim$3 kpc. However, due to its reliance primarily on main-sequence stars, as opposed to giants, this map does not penetrate to as great a depth as Marshall *et al.* (2006).

In addition to tracing the dust density in nearby regions of the Galaxy (within several kiloparsecs), this map can be used to determine the distribution of stars in the Galactic plane. Earlier optical studies of the distribution of stars in the Galaxy traditionally consider only high-latitude stars, where the correction for dust extinction is straightforward (e.g., Jurić *et al.* 2008). Infrared surveys of the plane are less sensitive to dust extinction, but their wavelength coverage also makes them less sensitive to intrinsic stellar type, rendering photometric distances uncertain. The mapping efforts described here provide distances to stars throughout the Galactic plane, enabling future studies of the distribution of stars in the disk.

The technique described in this thesis is not limited to PS1 and 2MASS photometry. Near-infrared

photometry, in particular, has the potential to extend the map to greater extinctions, due to the steep drop-off in extinction with increasing wavelength. Three near-infrared surveys are of particular interest. WISE, discussed in § 0.3.3 in the context of the *Planck* dust maps, has conducted an all-sky survey in the NIR and MIR. Most useful to stellar inference are the passbands centered on 3.4 and 4.6 $\mu$m. *Spitzer* GLIMPSE surveyed the Galactic plane in the NIR and MIR (Churchwell *et al.* 2009), providing a deeper view into some of the regions of the Milky Way with the most complicated dust structure. Finally, UKIDSS is in the process of surveying over 7000 deg$^2$ of the Northern sky, including a strip through the Galactic plane, in the NIR *J*, *H* and *K* bands (Lawrence *et al.* 2007). In the areas covered, UKIDSS will constitute a significant improvement over 2MASS.

Additional near-UV/optical/NIR surveys are also of interest. The Dark Energy Survey (DES; The Dark Energy Survey Collaboration 2005) is surveying 5000 deg$^2$ of the southern sky, largely complementary to the PS1 footprint, in a similar filter set. The LSST (Ivezic *et al.* 2008) will provide deep *ugrizy* photometry for the sky south of a declination of $\delta \approx 34.5°$. The ESA *Gaia* mission (Lindegren *et al.* 1994) is currently in the process of collecting multiband photometry, geometric parallax distance measurements and proper motions for one billion stars. Parallax distances, where available, will vastly improve stellar distance estimates, breaking the dwarf-giant degeneracy in particular. Proper motion measurements from *Gaia* will provide additional information about the populations stars belong to, helping us to infer stellar distances and types.

In addition to determining the dust density in the nearby Galaxy, our method can be used to determine the distribution of stars in the Galactic plane. Earlier optical studies of the distribution of stars in the Galaxy traditionally consider only high-latitude stars, where the correction for dust

extinction is straightforward (e.g., Jurić *et al.* 2008). Infrared surveys of the plane are less sensitive to dust extinction, but their wavelength coverage also makes them less sensitive to intrinsic stellar type, rendering photometric distances uncertain. Our technique provides distances to stars throughout the Galactic plane, enabling future studies of the distribution of stars in the disk.

The technique described in this thesis is not limited to PS1 and 2MASS photometry. Inclusion of information from WISE, *Spitzer* GLIMPSE, as well as SDSS *u*-band photometry will improve our distance and reddening estimates. In addition, kinematic information, such as proper motion, may be incorporated into our framework in order to allow a more precise determination of stellar distances.

Upcoming surveys will also dramatically enhance our ability to measure the distances and reddenings to stars in the Galaxy. The LSST (Ivezic *et al.* 2008) will provide deeper photometry spanning a similar set of filters as those used in SDSS and Pan-STARRS 1, providing photometry for the sky south of $\delta < +34.5°$. In the nearer future, the Dark Energy Survey (DES) will survey a complementary 5000 deg$^2$ of sky to Pan-STARRS 1, in a similar filter set (The Dark Energy Survey Collaboration 2005). The *Gaia* mission (Lindegren *et al.* 1994), meanwhile, will provide multiband photometry and low-resolution spectroscopy alongside parallax distance measurements and proper motions for one billion stars. *Gaia's* parallax distances, in particular, will break many of the degeneracies in our model for $r_{P1} \lesssim 20$ stars, while its proper motions will aid in inferring the population each star belongs to. These new datasets will increase the power of our method to determine Galactic reddening and structure.

Improvements to the model also have the potential to greatly improve on the 3D dust map pre-

sented here. The technique developed in this thesis does a remarkable job of tracing dust structure in 3D, despite the fact that it is built up sightline-by-sightline and does not assume any spatial correlations in the 3D dust density field. A more physical model would characterize the distribution of dust throughout the volume of the Milky Way as a density field with some power spectrum. Doing so would allow neighboring regions of the sky to "share" information in an optimal way, and alleviate the "finger-of-God" phenomenon observed in the dust map presented here. Several researchers have conducted work in this direction, including Lallement *et al.* (2014) and Sale & Magorrian (2014).

A reliable map the three-dimensional distribution of dust is important to a wide range of astrophysics research. Nearly all observational work in the ultraviolet, optical and near infrared requires accurate dust correction. A three-dimensional dust map is particularly important for Galactic astronomy, where reddening is strongly distance-dependent. For extra-Galactic astronomy, a dust map derived from stellar colors is complementary to far-infrared dust-emission-based maps, due to the very different systematics that affect the two methods. But dust is not just a nuisance to be corrected for – by tracing the three-dimensional structure of the interstellar medium, we shed light on the morphology of the Milky Way. The data product developed and presented in this thesis – a three-dimensional map of dust in the nearest several kiloparsecs of our Galaxy – is incredibly rich, and I expect that it will find many different uses not yet envisioned by the author.

# A

# Mathematical Details

A number of derivations of methods used in the text are presented in somewhat greater detail below.

## A.1 Bounded Harmonic Mean Estimate of the Bayesian Evidence

The harmonic mean approximation, developed in Gelfand & Dey (1994), allows one to compute the Bayesian evidence using samples returned from a Markov Chain Monte Carlo simulation. For a

model with parameters $\theta$ and data $D$, Bayes' rule tells us that

$$p(\theta|D) = \frac{p(D|\theta)\,p(\theta)}{p(D)}\,. \tag{A.1}$$

We wish to compute the evidence $p(D)$, often denoted by $Z$. Multiplying each side of the above by an arbitrary function $\phi(\theta)$, rearranging terms and taking the integral over all $\theta$,

$$\frac{1}{p(D)} \int \mathrm{d}\theta\, \phi(\theta) = \int \mathrm{d}\theta\, p(\theta|D)\, \frac{\phi(\theta)}{p(D|\theta)\,p(\theta)}\,. \tag{A.2}$$

The r.h.s. is simply the expectation value of

$$\frac{\phi(\theta)}{p(D|\theta)\,p(\theta)} \tag{A.3}$$

for samples drawn from the posterior density $p(\theta|D)$. This is convenient, since MCMC methods draw a set of samples from the distribution $p(\theta|D)$. If the integral of $\phi(\theta)$ is normalized to unity, then

$$\frac{1}{p(D)} \equiv \frac{1}{Z} \approx \left\langle \frac{\phi(\theta)}{p(D|\theta)\,p(\theta)} \right\rangle_{\text{chain}}\,. \tag{A.4}$$

With $\phi(\theta) = \text{const.}$, the harmonic mean estimate is known to have infinite variance, which gives the method a somewhat notorious reputation. However, the "bounded" harmonic mean estimate has finite variance as long as $\phi$ has steeper wings than $p(\theta|D)$ (Robert & Wraith 2009). We choose $\phi$ to

be constant within an ellipse centered on a point of high density within the chain, and zero outside (Robert & Wraith 2009). The ellipse is aligned with the principle axes of the covariance matrix, in order to ensure that it contains only well sampled regions of parameter space.

We find a point of high density by first centering an ellipse on a random point in the chain. Because the points in the chain are sampled proportionately to the posterior probability density, this point is already likely to lie in a well-sampled region of parameter space. We then find the mean of the points in the chain falling in the ellipse, and move the center of the ellipse to that position in parameter space. One can iterate this procedure several times to settle into a densely sampled region of parameter space. The size of the ellipse we use to define $\phi(\theta)$ is chosen such that a preset fraction of samples in the chain are enclosed. For our calculations, we iterate five times to find a dense region of parameter space, and scale the ellipse such that it contains 5% of samples.

## A.2 Markov Chain "Swap" Proposals

Because of the way in which we parameterize the line-of-sight distance versus reddening profile, there can be strong anticorrelations between the different parameters. The differential reddening in one distance bin is often strongly anticorrelated with the differential reddening in neighboring distance bins, because transferring some differential reddening from one bin to a neighboring bin keeps the cumulative reddening constant in following distance bins. Similarly, if the data is well fit by a large jump in reddening in one bin, it is often also well fit by a jump in reddening in a neighboring bin. These strong anticorrelations between the differential reddening in neighboring distance bins can slow down Markov chain convergence when fitting the line-of-sight reddening profile.

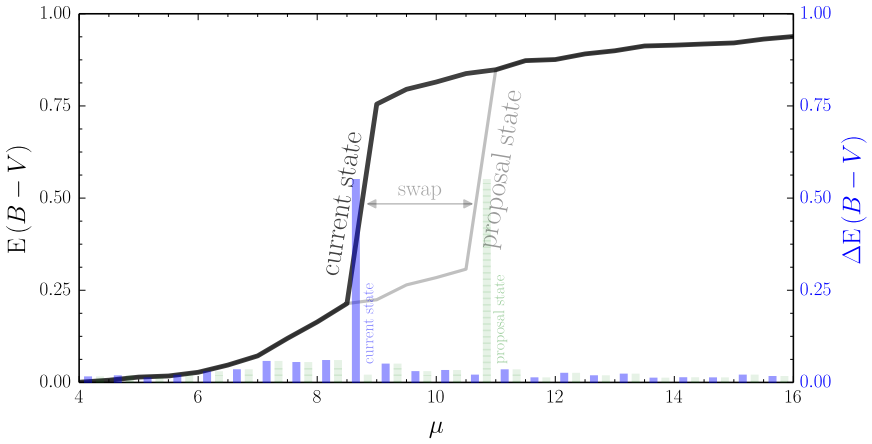


Figure A.1: Generation of an MCMC proposal state by the "swap" proposal method. The proposal state is identical to the current state, up to a swap in differential reddening in two bins. The black curve shows the cumulative reddening of the current state, while the light gray curve shows the cumulative reddening of the proposal state. The blue bars show the current differential reddening in each distance bin, while the striped green bars show the proposed differential reddening in each distance bin. Note that the two are identical, up to a swap between two distance bins.

We therefore introduce a new type of Markov Chain Monte Carlo (MCMC) proposal step, which we term the "swap" proposal. In order to generate a proposal state for the Markov chain, we swap the differential reddening in two distance bins, as shown in Fig. A.1.

The swap proposal is symmetric, allowing the usual Metropolis-Hastings acceptance probability to be used. Call the current state $X$ and the proposal state $Y$, and denote the two distance bins that were swapped to generate $Y$ as $i$ and $j$. The probability of proposing $Y$, $Q(X \to Y)$, is simply the probability that bins $i$ and $j$ are selected to be swapped. As long as the choice of $i$ and $j$ has nothing to do with the current state of the chain, the reverse step, from $Y$ to $X$, is equally likely to be proposed. That is, $Q(Y \to X)$ is also simply equal to the probability that distance bins $i$ and $j$ are

selected to be swapped. The acceptance probability, $\mathcal{A}(X \to Y)$, is therefore given by

$$\mathcal{A}(X \to Y) = \min\left(1,\ \frac{p(Y)}{p(X)}\frac{Q(Y \to X)}{Q(X \to Y)}\right) = \min\left(1,\ \frac{p(Y)}{p(X)}\right) , \tag{A.5}$$

where $p(X)$ and $p(Y)$ are the probability densities of $X$ and $Y$, respectively. This is simply the usual Metropolis-Hastings acceptance probability.

The addition of swap proposals, alongside Metropolis-Hastings proposals and affine stretch proposals, allows the Markov chain to mix more quickly. Many distance-reddening curves for the sightline plotted in Fig. 1.5, for example, differ primarily in which distance bin the large jump in reddening occurs. In such a sightline, the addition of swap proposals allows the Markov chain to transition quickly between probable states, greatly improving convergence times.

## A.3 Stellar Sample Reweighting

Here, we derive in detail how to reweight the Markov Chain samples resulting from the naive stellar inferences, in order to condition the stellar parameters on the line-of-sight reddening profile. This discussion complements § 1.7.

Given a fixed line-of-sight reddening profile parameterized by, $E(\mu; \vec{\alpha})$, each star is described by a distance $\mu$, stellar type $\vec{\Theta}$, and fractional offset $\delta$ from the reddening profile. The posterior of these parameters, conditioned on the star's photometry and the line-of-sight reddening profile, is given by

$$p\left(\mu, \vec{\Theta}, \delta \,|\, \vec{m},\ \vec{\alpha}\right) \propto p\left(\vec{m} \,|\, \mu, \vec{\Theta}, \delta, \vec{\alpha}\right) p\left(\mu, \vec{\Theta}, \delta \,|\, \vec{\alpha}\right) . \tag{A.6}$$

The second term on the right-hand side can be broken down into two parts,

$$p\left(\mu, \vec{\Theta}, \delta \,|\, \vec{\alpha}\right) \propto p\left(\mu, \vec{\Theta}\right) p(\delta \,|\, \mu, \vec{\alpha}) \ . \tag{A.7}$$

Thus,

$$p\left(\mu, \vec{\Theta}, \delta \,|\, \vec{m},\ \vec{\alpha}\right) \propto p\left(\vec{m} \,|\, \mu, \vec{\Theta}, \delta, \vec{\alpha}\right) p\left(\mu, \vec{\Theta}\right) p(\delta \,|\, \mu, \vec{\alpha}) \ . \tag{A.8}$$

The two stellar parameterizations, $\left\{\mu, \vec{\Theta}, \delta, \vec{\alpha}\right\}$ and $\left\{\mu, \vec{\Theta}, E\right\}$, are equivalent, as the stellar distance modulus, $\mu$, the line-of-sight reddening parameters, $\vec{\alpha}$, and the star's fractional offset, $\delta$, from the line-of-sight reddening are sufficient to determine the stellar reddening, $E$. We would like to reweight the samples we store in the space $\left\{\mu, \vec{\Theta}, E\right\}$, so that they correspond to the posterior density given above, in Eq. (A.8). As described in § 1.2, the samples we store in our initial processing are drawn from the posterior density

$$p\left(\mu, \vec{\Theta}, E \,|\, \vec{m}\right) \propto p\left(\vec{m} \,|\, \mu, \vec{\Theta}, E\right) p\left(\mu, \vec{\Theta}\right) p(E) \ , \tag{A.9}$$

with a flat prior on $E$, so that $p(E) = \text{const}$. Transforming to the parameterization $\left\{\mu, \vec{\Theta}, \delta, \vec{\alpha}\right\}$, we have to transform the flat prior $p(E)$ to an equivalent prior, $p(\delta \,|\, \mu, \vec{\alpha})$. This prior is given by

$$p(\delta \,|\, \mu, \vec{\alpha}) = p(E) \left.\frac{\partial E}{\partial \delta}\right|_{\mu, \vec{\alpha}} \propto \left.\frac{\partial E}{\partial \delta}\right|_{\mu, \vec{\alpha}} \ , \tag{A.10}$$

where we have taken out the constant factor $p(E)$ on the r.h.s. and replaced the equality with a proportionality. The stellar reddening is related to $\mu$, $\vec{\alpha}$ and $\delta$ by Eq. (1.43). Taking the derivative w.r.t. $\delta$,

$$\left.\frac{\partial E}{\partial \delta}\right|_{\mu,\vec{\alpha}} = \frac{\partial}{\partial \delta}\left[(1+\delta_i)\, E(\mu_i;\vec{\alpha})\right] = E(\mu_i;\vec{\alpha}) \ . \tag{A.11}$$

The flat prior in $E$ thus implies a prior on $\delta$ equal to

$$p(\delta \mid \mu, \vec{\alpha}) \propto E(\mu_i;\vec{\alpha}) \ . \tag{A.12}$$

In order to sample from Eq. (A.8), we can weight the samples from our initial processing by the ratio of the prior in the new parameterization, where reddening is conditioned on the line-of-sight reddening profile, to the prior used in the initial sampling, where a flat prior on reddening is used. From the above calculation, this ratio is given by

$$\frac{p_{\rm new}(\delta \mid \mu, \vec{\alpha})}{p_{\rm old}(\delta \mid \mu, \vec{\alpha})} \propto \frac{p_{\rm new}(\delta \mid \mu, \vec{\alpha})}{E(\mu_i;\vec{\alpha})} \ . \tag{A.13}$$

The functional form of $p_{\rm new}(\delta \mid \mu, \vec{\alpha})$ is given by Eq. (1.44).

## A.4 SEGUE-Derived Reddenings

Here, we review a method for calculating stellar reddenings on the basis of SDSS photometry and SEGUE predicted intrinsic stellar colors. As explained in Schlafly & Finkbeiner (2011), since the

extinction in an individual band $X$ is given by

$$A_X = R_X \mathrm{E}(B-V) \ , \tag{A.14}$$

colors transform as

$$\mathrm{E}(X-Y) = A_Y - A_X = (R_Y - R_X)\, \mathrm{E}(B-V) \ . \tag{A.15}$$

If we have only one color, $X - Y$, we can therefore estimate reddening as

$$\mathrm{E}(B-V) = \frac{\mathrm{E}(X-Y)}{R_Y - R_X} \, . \tag{A.16}$$

Our goal is to extend this formula to allow the use of multiple colors, possibly with strong covariance. Since Schlafly & Finkbeiner (2011) only predict the colors of stars, and not their overall magnitudes, we work in color space. Denote the intrinsic stellar colors as $\vec{c}_i$, and the reddened colors as $\vec{c}_r$.

In a multidimensional color space, Eq. (A.15) becomes

$$\vec{c}_r - \vec{c}_i = \vec{R}\ \mathrm{E}(B-V) \ , \tag{A.17}$$

where $\vec{R}$ has one component per color $X - Y$, given by $R_{XY} \equiv R_Y - R_X$. The estimated intrinsic colors and observed reddened colors are Gaussian random variables, with covariances $\Sigma_i$ and $\Sigma_r$,

respectively. Denote the estimated intrinsic colors as $\vec{c}_i'$, and the observed reddened colors as $\vec{c}_r'$. The likelihood of these two quantities taking on a particular set of values is given by

$$p\left(\vec{c}_i',\, \vec{c}_r' \,|\, \mathrm{E}(B-V)\,,\, \vec{c}_r\right) = \mathcal{N}\left(\vec{c}_r' \,|\, \vec{c}_r,\, \Sigma_r\right) \mathcal{N}\left(\vec{c}_i' \,|\, \vec{c}_i,\, \Sigma_i\right) \tag{A.18}$$

$$= \mathcal{N}\left(\vec{c}_r' \,|\, \vec{c}_r,\, \Sigma_r\right) \mathcal{N}\left(\vec{c}_i' \,|\, \vec{c}_r - \vec{R}\,\mathrm{E}(B-V)\,,\, \Sigma_i\right)\,. \tag{A.19}$$

In the second step, we have replaced $\vec{c}_i$ using Eq. (A.17). Using the symmetry of the Gaussian distribution,

$$p\left(\vec{c}_i',\, \vec{c}_r' \,|\, \mathrm{E}(B-V)\,,\, \vec{c}_r\right) = \mathcal{N}\left(\vec{c}_r \,|\, \vec{c}_r',\, \Sigma_r\right) \mathcal{N}\left(\vec{c}_r - \vec{R}\,\mathrm{E}(B-V) \,|\, \vec{c}_i',\, \Sigma_i\right) \tag{A.20}$$

$$= \mathcal{N}\left(\vec{c}_r \,|\, \vec{c}_r',\, \Sigma_r\right) \mathcal{N}\left(\vec{R}\,\mathrm{E}(B-V) - \vec{c}_r\,|\, -\vec{c}_i',\, \Sigma_i\right)\,. \tag{A.21}$$

If we assume a flat prior on $\mathrm{E}(B-V)$ and $\vec{c}_r$, then the above is proportional to the posterior probability density $p(\mathrm{E}(B-V)\,,\, \vec{c}_r \,|\, \vec{c}_i',\, \vec{c}_r')$. We could, in practice, frame the question in terms of the intrinsic colors $\vec{c}_i$, and put priors on them based on our Galactic and stellar model, but we wish to avoid tying our SEGUE-derived reddenings in any way to our Bayesian photometric reddening estimates. Now, integrating over $\vec{c}_r$, we obtain a convolution of two Gaussians, which is itself a Gaussian distribution:

$$p\left(\mathrm{E}(B-V) \,|\, \vec{c}_i',\, \vec{c}_r'\right) \propto \int \mathrm{d}\vec{c}_r\, \mathcal{N}\left(\vec{c}_r \,|\, \vec{c}_r',\, \Sigma_r\right) \mathcal{N}\left(\vec{R}\,\mathrm{E}(B-V) - \vec{c}_r\,|\, -\vec{c}_i',\, \Sigma_i\right) \tag{A.22}$$

$$= \mathcal{N}\left(\vec{R}\,\mathrm{E}(B-V) \,|\, \vec{c}_r' - \vec{c}_i',\, \Sigma_r + \Sigma_i\right)\,. \tag{A.23}$$

The probability density function of $\mathrm{E}(B-V)$ is thus a ray taken through a multivariate Gaussian. It can be shown that the above is also Gaussian, with mean and standard deviation given by

$$\langle \mathrm{E}(B-V) \rangle = \frac{(\vec{c}\,'_r - \vec{c}\,'_i)^T (\Sigma_r + \Sigma_i)^{-1} \vec{R}}{\vec{R}^T (\Sigma_r + \Sigma_i)^{-1} \vec{R}} , \tag{A.24}$$

$$\sigma^2_{\mathrm{E}(B-V)} = \left[ \vec{R}^T (\Sigma_r + \Sigma_i)^{-1} \vec{R} \right]^{-1} . \tag{A.25}$$

We plug intrinsic stellar colors appropriate for the SSPP stellar parameters into $\vec{c}\,'_r$, and use the observed SDSS colors for $\vec{c}\,'_i$.

One final note is that Schlafly & Finkbeiner (2011) used the SSPP stellar types to derive estimates of the mean and covariance of the magnitudes, rather than the colors. We will now show how to obtain the covariance of the colors from the covariance matrix of the magnitudes. Denote the covariance matrix of the magnitudes as $\Sigma_{ij}$, where $i$ and $j$ label passbands. Label the color $m_i - m_j$ as $c_{ij}$. We then refer to the covariance matrix of the colors $c_{ij}$ and $c_{k\ell}$ as $\Sigma'_{ij,k\ell}$. By expanding out

$$\Sigma'_{ij,k\ell} = \left\langle c_{ij} c_{k\ell} \right\rangle - \left\langle c_{ij} \right\rangle \left\langle c_{k\ell} \right\rangle \tag{A.26}$$

in terms of magnitudes, one obtains

$$\Sigma'_{ij,k\ell} = \Sigma_{ik} - \Sigma_{i\ell} - \Sigma_{jk} + \Sigma_{j\ell} . \tag{A.27}$$

The common choice of colors is to set the $i^{\mathrm{th}}$ color to $m_i - m_{i+1}$. Plugging $j = i+1$ and $\ell = k+1$

into the above, we find that the covariance of the $i^{\text{th}}$ color with the $k^{\text{th}}$ color is given by

$$\Sigma'_{i,k} = \Sigma_{i,k} - \Sigma_{i,k+1} - \Sigma_{i+1,k} + \Sigma_{i+1,k+1} \,. \tag{A.28}$$

# References


Allende Prieto, C., Sivarani, T., Beers, T. C., Lee, Y. S., Koesterke, L. *et al.* (2008). The SEGUE Stellar Parameter Pipeline. III. Comparison with High-Resolution Spectroscopy of SDSS/SEGUE Field Stars. *The Astronomical Journal*, 136(5):2070–2082.

Annis, J., Soares-Santos, M., Strauss, M., Becker, A., Dodelson, S. *et al.* (2014). The Sloan Digital Sky Survey Coadd: 275 deg$^2$ of Deep Sloan Digital Sky Survey Imaging on Stripe 82. *The Astrophysical Journal*, 794(2):120.

Barnard, E. E. (1916). Some of the Dark Markings on the Sky and What They Suggest. *The Astrophysical Journal*, 43(1):1.

Berry, M., Ivezić, Ž., Sesar, B., Jurić, M., Schlafly, E. F. *et al.* (2012). The Milky Way Tomography with Sloan Digital Sky Survey. IV. Dissecting Dust. *The Astrophysical Journal*, 757(2):166.

Boggess, N., Mather, J., Weiss, R., Bennett, C., Cheng, E. *et al.* (1992). The COBE mission – Its design and performance two years after launch. *The Astrophysical Journal*, 397(2):420–429.

Bok, B. J., Wolf's Method of Measuring Dark Nebulae. In H. Shapley, ed., *Source Book in Astronomy, 1900-1950*, chap. 47, (pp. 285–288). Cambridge, MA: Harvard University Press, 1960.

Bond, N. a., Ivezić, Ž., Sesar, B., Jurić, M., Munn, J. a. *et al.* (2010). The Milky Way Tomography with SDSS. III. Stellar Kinematics. *The Astrophysical Journal*, 716(1):1–29.

Bressan, A., Marigo, P., Girardi, L., Salasnich, B., Cero, C. D. *et al.* (2012). PARSEC: stellar tracks and isochrones with the PAdova and TRieste Stellar Evolution Code. 20(August):1–20.

Burstein, D. & Heiles, C. (1978a). A new method for determining the reddenings of extragalactic objects. *The Astrophysical Journal Letters*, 19(9):69–73.

Burstein, D. & Heiles, C. (1978b). HI, Galaxy Counts, and Reddening: Variation in the Gas-to-Dust Ratio, the Extinction at High Galactic Latitudes, and a New Method for Determining Galactic Reddening. *The Astrophysical Journal*, 225:40–55.

Burstein, D. & Heiles, C. (1982). Reddenings Derived from HI and Galaxy Counts - Accuracy and Maps. *The Astronomical Journal*, 87:1165.

Cardelli, J. A., Clayton, G. C. & Mathis, J. S. (1989). The Relationship Between Infrared, Optical, and Ultraviolet Extinction. *The Astrophysical Journal*, 345:245.

Chabrier, G. (2001). The galactic disk mass budget. I. Stellar mass function and density. *The Astrophysical Journal*, 554(2):1274–1281.

Chen, B.-Q., Liu, X.-W., Yuan, H.-B., Zhang, H.-H., Schultheis, M. *et al.* (2014). A three-dimensional extinction map of the Galactic anticentre from multiband photometry. *Monthly Notices of the Royal Astronomical Society*, 443(2):1192–1210.

Churchwell, E., Babler, B. L., Meade, M. R., Whitney, B. A., Benjamin, R. *et al.* (2009). The Spitzer /GLIMPSE Surveys: A New View of the Milky Way. *Publications of the Astronomical Society of the Pacific*, 121(877):213–230.

Draine, B. (2003). Interstellar Dust Grains. *Annual Review of Astronomy and Astrophysics*, 41(1):241–289.

Draine, B. T. & Li, A. (2007). Infrared Emission from Interstellar Dust. IV. The Silicate-Graphite-PAH Model in the Post- Spitzer Era. *The Astrophysical Journal*, 657(2):810–837.

Drimmel, R. & Spergel, D. (2001). Three-dimensional Structure of the Milky Way Disk: The Distribution of Stars and Dust beyond 0.35 $R_\odot$. *The Astrophysical Journal*, 20(1):181–202.

ESA (1997). *The HIPPARCOS and TYCHO catalogues. Astrometric and photometric star catalogues derived from the ESA HIPPARCOS Space Astrometry Mission*, vol. 1200 of *ESA Special Publications*.

Fitzpatrick, E. L. (1999). Correcting for the Effects of Interstellar Extinction. *Publications of the Astronomical Society of the Pacific*, 111(755):63–75.

Foreman-Mackey, D., Hogg, D. W., Lang, D. & Goodman, J. (2012). emcee: The MCMC Hammer. *arXiv e-prints*: 1202.3665.

Foster, J., Román-Zúñiga, C., Goodman, A., Lada, E. & Alves, J. (2008). Hunting Galaxies to (and for) Extinction. *The Astrophysical Journal*, 674(2):831–845.

Galilei, Galileo (1610). *Sidereus Nuncius*, Peter Baker, ed. and trans. (Oklahoma City: Byzantium Press, 2004), based on the trans. by Edward Stafford Carlos (London: Rivingtons, 1880).

Gelfand, A. E. & Dey, D. K. (1994). Bayesian Model Choice: Asymptotics and Exact Calculations. *Journal of the Royal Statistical Society*, 56(3):501–514.

Gelman, A. & Rubin, D. B. (1992). Inference from Iterative Simulation Using Multiple Sequences. *Statistical Science*, 7(4):457–472.

Gilmore, G., Surveys and Star Counts: The Kapteyn Legacy. In P. C. Van Der Kruit & K. Van Berkel, eds., *The Legacy of J.C. Kapteyn: Studies on Kapteyn and the Development of Modern Astronomy*, vol. 246 of *Astrophysics and Space Science Library*, chap. 12, (pp. 265–276). Dordrecht: Springer Netherlands, 2000.

Gingerich, O., Kapteyn, Shapley, and their Universes. In P. C. Van Der Kruit & K. Van Berkel, eds., *The Legacy of J.C. Kapteyn: Studies on Kapteyn and the Development of Modern Astronomy*, vol. 246 of *Astrophysics and Space Science Library*, chap. 9, (pp. 191–212). Dordrecht: Springer Netherlands, 2000.

Goodman, J. & Weare, J. (2010). Ensemble samplers with affine invariance. *Communications in Applied Mathematics and Computational Science*, 5(1):65–80.

Gorski, K. M., Hivon, E., Banday, A. J., Wandelt, B. D., Hansen, F. K. *et al.* (2005). HEALPix: A Framework for High-Resolution Discretization and Fast Analysis of Data Distributed on the Sphere. *The Astrophysical Journal*, 622(2):759–771.

Green, G. M., Schlafly, E. F., Finkbeiner, D. P., Jurić, M., Rix, H.-W. *et al.* (2014). Measuring Distances and Reddenings for a Billion Stars: Toward a 3D Dust Map from Pan-STARRS 1. *The Astrophysical Journal*, 783(2):114.

Green, G. M., Schlafly, E. F., Finkbeiner, D. P., Rix, H.-W., Martin, N. *et al.* (2015). A Three-dimensional Map of Milky Way Dust. *The Astrophysical Journal*, 810(1):25.

Hanson, R. J. & Bailer-Jones, C. a. L. (2014). 3D Galactic dust extinction mapping with multiband photometry. *Monthly Notices of the Royal Astronomical Society*, 438(4):2938–2953.

Herschel, W. (1785). On the Construction of the Heavens. *Philosophical Transactions of the Royal Society of London*, 75:213–266.

Hodapp, K. W., Kaiser, N., Aussel, H., Burgett, W., Chambers, K. C. *et al.* (2004). Design of the Pan-STARRS telescopes. *Astronomische Nachrichten*, 325:636–642.

Hogg, D. W., Bovy, J. & Lang, D. (2010). Data analysis recipes: Fitting a model to data. *arXiv e-prints*: 1008.4686.

Ivezić, Ž., Sesar, B., Jurić, M., Bond, N., Dalcanton, J. *et al.* (2008a). The Milky Way Tomography with SDSS. II. Stellar Metallicity. *The Astrophysical Journal*, 684(1):287–325.

Ivezić, Ž., Sesar, B., Jurić, M., Bond, N., Dalcanton, J. *et al.* (2008b). The Milky Way Tomography with SDSS. II. Stellar Metallicity. *The Astrophysical Journal*, 684(1):287–325.

Ivezić, Ž., Tyson, J. A., Acosta, E., Allsman, R., Anderson, S. F. *et al.* (2008). LSST: from Science Drivers to Reference Design and Anticipated Data Products. *arXiv e-prints*: 0805.2366.

Jurić, M., Ivezić, Ž., Brooks, A., Lupton, R. H., Schlegel, D. *et al.* (2008). The Milky Way Tomography with SDSS. I. Stellar Number Density Distribution. *The Astrophysical Journal*, 673(2):864–914.

Kaiser, N., Burgett, W., Chambers, K., Denneau, L., Heasley, J. *et al.*, The Pan-STARRS wide-field optical/NIR imaging survey. In *Society of Photo-Optical Instrumentation Engineers (SPIE) Conference Series*, vol. 7733 of *Society of Photo-Optical Instrumentation Engineers (SPIE) Conference Series*. San Diego, CA, 2010.

Kapteyn, J. C. (1904). Remarks on the determination of the number and mean parallax of stars of different magnitude and the absorption of light in space. *The Astronomical Journal*, 24:115.

Kapteyn, J. C. (1909a). On the Absorption of Light in Space. *The Astrophysical Journal*, 29:46.

Kapteyn, J. C. (1909b). On the Absorption of Light in Space. Second Paper. *The Astrophysical Journal*, 30:284.

Kruschke, J., *Doing Bayesian Data Analysis: A Tutorial Introduction with R*. Burlington, MA: Academic Press, 2010.

Lada, C. J., Lada, E. A., Clemens, D. P. & Bally, J. (1994). Dust Extinction and Molecular Gas in the Dark Cloud IC 5146. *The Astrophysical Journal*, 429(2):694.

Lallement, R., Vergely, J.-L., Valette, B., Puspitarini, L., Eyer, L. *et al.* (2014). 3D maps of the local ISM from inversion of individual color excess measurements. *Astronomy & Astrophysics*, 561:A91.

Lallement, R., Welsh, B. Y., Vergely, J. L., Crifo, F. & Sfeir, D. (2003). 3D mapping of the dense interstellar gas around the Local Bubble. *Astronomy & Astrophysics*, 411(3):447–464.

Lawrence, A., Warren, S., Almaini, O., Edge, A., Hambly, N. *et al.* (2007). The UKIRT Infrared Deep Sky Survey (UKIDSS). *Monthly Notices of the Royal Astronomical Society*, 379(4):1599–1617.

Lee, Y. S., Beers, T. C., Sivarani, T., Allende Prieto, C., Koesterke, L. *et al.* (2008a). The SEGUE Stellar Parameter Pipeline. I. Description and Comparison of Individual Methods. *The Astronomical Journal*, 136(5):2022–2049.

Lee, Y. S., Beers, T. C., Sivarani, T., Johnson, J. a., An, D. *et al.* (2008b). The SEGUE Stellar Parameter Pipeline. II. Validation With Galactic Globular and Open Clusters. *The Astronomical Journal*, 136(5):2050–2069.

Lemke, D. (2009). The short history of infrared space telescopes. *Astronomische Nachrichten*, 330(6):562–567.

Li, A. & Draine, B. T. (2001). Infrared Emission from Interstellar Dust. II. The Diffuse Interstellar Medium. *The Astrophysical Journal*, 554(2):778.

Lindegren, L., Perryman, M. A., Bastian, U., Dainty, C., Hog, E. *et al.*, GAIA: Global Astrometric Interferometer for Astrophysics. In M. A. Ealey & F. Merkle, eds., *Amplitude and Intensity Spatial Interferometry II*, vol. 2200 of *Society of Photo-Optical Instrumentation Engineers (SPIE) Conference Series*, (pp. 599–608). Kailua, Kona, HI, 1994.

Lombardi, M. (2009). NICEST, a near-infrared color excess method tailored to small-scale structures. *Astronomy & Astrophysics*, 493(2):735–745.

Lombardi, M. & Alves, J. (2001). Mapping the interstellar dust with near-infrared observations : An optimized multi-band technique. 1034:1023–1034.

Low, F. J., Rieke, G. & Gehrz, R. (2007). The Beginning of Modern Infrared Astronomy. *Annual Review of Astronomy and Astrophysics*, 45:43–75.

Lucretius, *de rerum natura (On the Nature of Things)*. Rouse, W. H. D & Smith, M. F., trans. Cambridge, MA: Harvard University Press, 1992.

Magnier, E., The Pan-STARRS PS1 Image Processing Pipeline. In S. Ryan, ed., *The Advanced Maui Optical and Space Surveillance Technologies Conference*, (p. E50). Wailea, Maui, HI, 2006.

Magnier, E., Calibration of the Pan-STARRS $3\pi$ Survey. In C. Sterken, ed., *The Future of Photometric, Spectrophotometric and Polarimetric Standardization*, vol. 364 of *Astronomical Society of the Pacific Conference Series*, (pp. 153–+). Blankenberge, Belgium, 2007.

Magnier, E. A., Liu, M., Monet, D. G. & Chambers, K. C., The extended solar neighborhood: precision astrometry from the Pan-STARRS 1 $3\pi$ Survey. In W. J. Jin, I. Platais, & M. A. C. Perryman, ed., *IAU Symposium*, vol. 248 of *IAU Symposium*, (pp. 553–559). Shanghai, 2008.

Mainzer, A., Bauer, J., Cutri, R. M., Grav, T., Masiero, J. *et al.* (2014). Initial Performance of the NEOWISE Reactivation Mission. *The Astrophysical Journal*, 792(1):30.

Mainzer, A., Bauer, J., Grav, T., Masiero, J., Cutri, R. M. *et al.* (2011). Preliminary Results from NEOWISE: An Enhancement to the Wide-Field Infrared Survey Explorer for Solar System Science. *The Astrophysical Journal*, 731(1):53.

Marshall, D. J., Robin, A. C., Reylé, C., Schultheis, M. & Picaud, S. (2006). Modelling the Galactic interstellar extinction distribution in three dimensions. *Astronomy & Astrophysics*, 453(2):635–651.

Neugebauer, G., Habing, H., van Duinen, R., Aumann, H., Baud, B. *et al.* (1984). The Infrared Astronomical Satellite (IRAS) mission. *The Astrophysical Journal Letters*, 278:L1–L6.

Newberg, H. & Yanny, B. (1997). Three-dimensional parameterization of the stellar locus with application to QSO color selection. *The Astrophysical Journal Supplement*, 113:89–104.

Onaka, P., Tonry, J. L., Isani, S., Lee, A., Uyeshiro, R. *et al.*, The Pan-STARRS Gigapixel Camera 1 and STARGRASP controller results and performance. In *Society of Photo-Optical Instrumentation Engineers (SPIE) Conference Series*, vol. 7014 of *Society of Photo-Optical Instrumentation Engineers (SPIE) Conference Series*. Marseilles, 2008.

Planck Collaboration (2011). Planck early results. I. The Planck mission. *Astronomy & Astrophysics*, 536:A1.

Planck Collaboration (2014). Planck 2013 results. XXXI. All-sky model of thermal dust emission. *Astronomy & Astrophysics*, 571:A11.

Planck Collaboration (2015). Planck 2015 results. X. Diffuse component separation: Foreground maps. *arXiv e-prints*: 1502.01588.

Planck Collaboration (2016). Planck intermediate results: XXIX. All-sky dust modelling with Planck, IRAS, and WISE observations. *Astronomy & Astrophysics*, 586:A132.

Pseudo Plutarch. *Placita philosophorum*. In W. W. Goodwin, ed., *Plutarch. Plutarch's Morals.* Cambridge, MA: Press of John Wilson and son, 1874. *Perseus Digital Library*. http://data.perseus.org/citations/urn:cts:greekLit:tlg0094.tlg003.perseus-eng1:3.1 (accessed 16 April 2016).

Robert, C. P. & Wraith, D. (2009). Computational methods for Bayesian model choice. *arXiv e-prints*: 0907.5123.

Robin, A. C., Reylé, C., Derrière, S. & Picaud, S. (2003). A synthetic view on structure and evolution of the Milky Way. *Astronomy & Astrophysics*, 409(2):523–540.

Rowles, J. & Froebrich, D. (2009). The structure of molecular clouds - I. All-sky near-infrared extinction maps. *Monthly Notices of the Royal Astronomical Society*, 395(3):1640–1648.

Russell, H. N. (1922). Dark Nebulae. *Proceedings of the National Academy of Sciences*, 8(5):115–118.

Sale, S. E. (2012). 3D extinction mapping using hierarchical Bayesian models. *Monthly Notices of the Royal Astronomical Society*, 427:2119–2131.

Sale, S. E. (2015). Three-dimensional extinction mapping and selection effects. *Monthly Notices of the Royal Astronomical Society*, 452(3):2960–2972.

Sale, S. E., Drew, J. E., Barentsen, G., Farnhill, H. J., Raddi, R. *et al.* (2014). A 3D extinction map of the northern Galactic plane based on IPHAS photometry. *Monthly Notices of the Royal Astronomical Society*, 443(4):2907–2922.

Sale, S. E. & Magorrian, J. (2014). Three-dimensional extinction mapping using Gaussian random fields. *Monthly Notices of the Royal Astronomical Society*, 445(1):256–269.

Schlafly, E. F. & Finkbeiner, D. P. (2011). Measuring Reddening With Sloan Digital Sky Survey Stellar Spectra and Recalibrating SFD. *The Astrophysical Journal*, 737(2):103.

Schlafly, E. F., Finkbeiner, D. P., Jurić, M., Magnier, E. A., Burgett, W. S. *et al.* (2012). Photometric Calibration of the First 1.5 Years of the Pan-STARRS1 Survey. *The Astrophysical Journal*, 756(2):158.

Schlafly, E. F., Green, G., Finkbeiner, D. P., Jurić, M., Rix, H.-W. *et al.* (2014a). A Map of Dust Reddening to 4.5 kpc from Pan-STARRS1. *The Astrophysical Journal*, 789(1):15.

Schlafly, E. F., Green, G., Finkbeiner, D. P., Rix, H.-W., Bell, E. F. *et al.* (2014b). A Large Catalog of Accurate Distances to Molecular Clouds from PS1 Photometry. *The Astrophysical Journal*, 786(1):29.

Schlafly, E. F., Green, G., Finkbeiner, D. P., Rix, H.-W., Burgett, W. S. *et al.* (2015). Three-dimensional Dust Mapping Reveals that Orion Forms Part of a Large Ring of Dust. *The Astrophysical Journal*, 799(2):116.

Schlegel, D. J., Finkbeiner, D. P. & Davis, M. (1998). Maps of Dust Infrared Emission for Use in Estimation of Reddening and Cosmic Microwave Background Radiation Foregrounds. *The Astrophysical Journal*, 500(2):525–553.

Seeley, D. & Berendzen, R. (1972a). The Development of Research in Interstellar Absorption, c. 1900-1930. *Journal for the History of Astronomy*, 3:52.

Seeley, D. & Berendzen, R. (1972b). The Development of Research in Interstellar Absorption, c. 1900-1930: Part 2. *Journal for the History of Astronomy*, 3:75.

Sesar, B., Jurić, M. & Ivezić, Ž. (2011). The Shape and Profile of the Milky Way Halo as Seen by the Canada-France-Hawaii Telescope Legacy Survey. *The Astrophysical Journal*, 731(1):4.

Shane, C. D. & Wirtanen, C. A. (1967). *Publications of the Lick Observatory*, 22:1.

Shapley, H. (1916). Studies of Magnitudes in Star Clusters: I. On the Absorption of Light in Space. *Proceedings of the National Academy of Sciences*, 2(1):12–15.

de Sitter, W. (1900). On the Systematic Difference, Depending on Galactic Latitude, Between the Photographic and visual magnitudes of the stars. *Publications of the Astronomical Laboratory at Groningen*, 2:1–22.

de Sitter, W. (1904). Investigation of the Systematic Difference Between the Photographic and Visual Magnitudes of the Stars Depending on the Galactic Latitude, based on photometric

observations by W. De Sitter, visual estimates by R. T. A. Innes, and photographs taken at the Cape Observatory, together with catalogues of the photometric and photographic magnitudes of 791 stars. *Publications of the Astronomical Laboratory at Groningen*, 12:1–167.

Skrutskie, M. F., Cutri, R. M., Stiening, R., Weinberg, M. D., Schneider, S. *et al.* (2006). The Two Micron All Sky Survey (2MASS). *The Astronomical Journal*, 131(2):1163–1183.

Slipher, V. M. (1909). Peculiar star spectra suggestive of selective absorption of light in space. *Lowell Observatory Bulletin*, 2:1–2.

Struve, F. G. W., *Études d'Astronomie Stellaire : Sur la voie lactée et sur la distance des étoiles fixes*. St. Petersburg: L'Imprimerie de l'Académie Impériale des Sciences, 1847.

Stubbs, C. W., Doherty, P., Cramer, C., Narayan, G., Brown, Y. J. *et al.* (2010). Precise Throughput Determination of the PanSTARRS Telescope and the Gigapixel Imager Using a Calibrated Silicon Photodiode and a Tunable Laser: Initial Results. *The Astrophysical Journal Supplements*, 191:376–388.

The Dark Energy Survey Collaboration (2005). The Dark Energy Survey. *arXiv e-prints*: 0510346.

Tonry, J. & Onaka, P., The Pan-STARRS Gigapixel Camera. In S. Ryan, ed., *Advanced Maui Optical and Space Surveillance Technologies Conference*. Wailea, Maui, HI, 2009.

Tonry, J. L., Stubbs, C. W., Lykke, K. R., Doherty, P., Shivvers, I. S. *et al.* (2012). The Pan-STARRS1 Photometric System. *The Astrophysical Journal*, 750(2):99.

Trumpler, R. J. (1930a). Absorption of Light in the Galactic System. *Publications of the Astronomical Society of the Pacific*, 42(248):214–227.

Trumpler, R. J. (1930b). Preliminary results on the distances, dimensions and space distribution of open star clusters. *Lick Observatory Bulletins*, 14(420):154–188.

Trumpler, R. J. (1930c). Spectrophotometric Measures of Interstellar Light Absorption. *Publications of the Astronomical Society of the Pacific*, 42(249):267–274.

Vergely, J.-L., Freire Ferrero, R., Siebert, A. & Valette, B. (2001). NaI and HI 3-D density distribution in the solar neighbourhood. *Astronomy & Astrophysics*, 366(3):1016–1034.

Warnes, G. (2001). The Normal Kernel Coupler: An adaptive Markov Chain Monte Carlo method for efficiently sampling from multi-modal distributions. Tech. Rep. 395, Department of Statistics, University of Washington.

Weingartner, J. C. & Draine, B. T. (2001). Dust Grain-Size Distributions and Extinction in the Milky Way, Large Magellanic Cloud, and Small Magellanic Cloud. *The Astrophysical Journal*, 548(1):296–309.

Wolf, M. (1923). Über den dunklen Nebel NGC 6960. *Astronomische Nachrichten*, 219(5239):109–116.

Wright, E. L., Eisenhardt, P. R. M., Mainzer, A. K., Ressler, M. E., Cutri, R. M. *et al.* (2010). The Wide-Field Infrared Survey Explorer (WISE): Mission Description and Initial On-Orbit Performance. *The Astronomical Journal*, 140(6):1868–1881.

Yanny, B., Rockosi, C., Newberg, H. J., Knapp, G. R., Adelman-McCarthy, J. K. *et al.* (2009). SEGUE: A Spectroscopic Survey of 240,000 Stars with g = 14-20. *The Astronomical Journal*, 137(5):4377–4399.

York, D. G., Adelman, J., Anderson, Jr., J. E., Anderson, S. F., Annis, J. *et al.* (2000). The Sloan Digital Sky Survey: Technical Summary. *The Astronomical Journal*, 120(3):1579–1587.

Yuan, H.-B., Liu, X.-W. & Xiang, M.-S. (2013). Empirical extinction coefficients for the GALEX, SDSS, 2MASS and WISE passbands. *Monthly Notices of the Royal Astronomical Society*, 13(3):2188–2199.

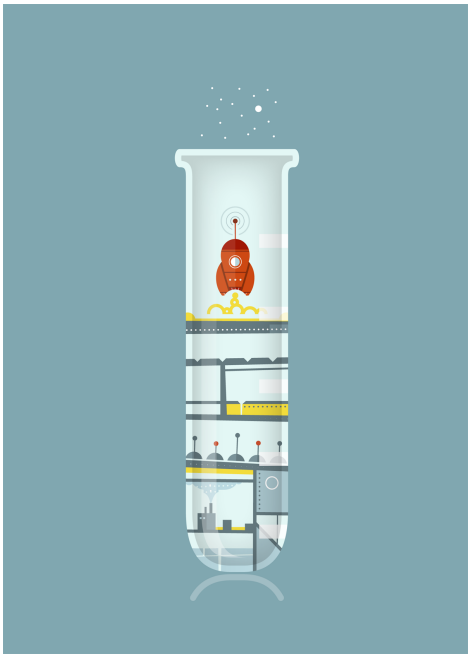

This thesis was typeset using LaTeX, originally developed by Leslie Lamport and based on Donald Knuth's TeX. The body text is set in 11 point Egenolff-Berner Garamond, a revival of Claude Garamont's humanist typeface. The above illustration, *Science Experiment 02*, was created by Ben Schlitter and released under CC BY-NC-ND 3.0. A template that can be used to format a PhD dissertation with this look & feel has been released under the permissive AGPL license, and can be found online at github.com/suchow/Dissertate or from its lead author, Jordan Suchow, at suchow@post.harvard.edu.